ULTRASONIC VIBRATION-ASSISTED LASER SURFACE ENGINEERING OF STRUCTURAL ALLOYS

By

SOURABH BISWAS

Bachelor of Engineering in Metallurgical and Materials Engineering
Indian Institute of Engineering Science and Technology
Shibpur, India
2011

Master of Science in Mechanical and Aerospace Engineering
Oklahoma State University
Stillwater, OK
2014

Submitted to the Faculty of the
Graduate College of the
Oklahoma State University
in partial fulfillment of
the requirements for
the Degree of
DOCTOR OF PHILOSOPHY
December, 2018

ULTRASONIC VIBRATION-ASSISTED LASER SURFACE ENGINEERING OF STRUCTURAL ALLOYS

Dissertation Approved:

Dr. Sandip P. Harimkar

Dissertation Adviser

Dr. A. Kaan Kalkan

Dr. Shuodao Wang

Dr. Ranji Vaidyanathan

ACKNOWLEDEGEMENTS

I am extremely grateful for the guidance, motivation and patience of my adviser Dr. Sandip P. Harimkar that was the key for successfully completing this project. I would like to thank Dr. Kalkan for being in my committee and performing Raman characterization studies on my samples in his lab as well as for his invaluable inputs that significantly enriched the analysis of my data. I would also like take this opportunity to thank my other committee members, Dr. Vaidyanathan and Dr. Wang being in my dissertation committee as well as for their constructive comments on my dissertation. This material is based upon work supported by the U.S. National Science Foundation (NSF CAREER Award No. CMMI-1149079). I am highly grateful to my colleagues Tanaji, Bindu, and Habib for not only assisting me with the experiments but also providing me with the adequate motivation over the past four years. I am highly thankful to my parents, Mr. Sanjoy Kr. Biswas and Mrs. Amita Biswas, my sister, Saptami Biswas, my cousin Arnab Sinha, and my sister-in-law Shaoni Sinha for their support and enthusiasm. I would like to thank my wife Mrs. Priyadarshini Dutta not only for her unflinching support but also for bearing my emotional swings during this project. I am highly grateful to my friend Dr. Adrish Ganguly for being an outside mentor and giving me invaluable inputs from an industrial perspective. I am highly grateful to my friends Joyjit, Sayan and Rehan for their help and support. Last but not the least, I would thank all my friends and well-wishers who have supported me in my life and am dedicating this work to each and every one of them.

Name: SOURABH BISWAS

Date of Degree: DECEMBER, 2018

Title of Study: ULTRASONIC VIBRATION-ASSISTED LASER SURFACE ENGINEERING OF STRUCTURAL ALLOYS

Major Field: MECHANICAL AND AEROSPACE ENGINEERING

Abstract: Simultaneous application of ultrasonic vibrations in conventional solidification processing techniques has been reported to be highly successful in elimination of dendritic microstructure in alloys and improved particle distribution in composites. However, similar studies in rapid solidification processing techniques such as laser processing have not been extensively performed. Hence, in this study, the major objective was to develop ultrasonic vibration-assisted laser surface engineering that involves simultaneous application of vertical ultrasonic vibrations on the substrate. This was achieved by attaching the substrates on a probe generating ultrasonic vibrations and simultaneously performing laser processing on the substrate. It should be noted that although laser surface engineering has recently emerged as one of the most popular non-conventional surface modification techniques as it offers refined microstructure, elemental redistribution, and excellent process control, it is often also associated with undesirable features such as dendritic, textured microstructure and elemental segregation. Detailed analysis on the effect of ultrasonic vibrations on the microstructural evolution, crystallographic texture, and phase evolution on laser surface melted and composite cladded commercial aluminum and titanium alloys is presented. Also, the effect of the microstructural, texture and phase changes in surface mechanical, tribological, and electrochemical properties was systematically studied. Furthermore, the effect of ultrasonic vibrations on laser surface engineering techniques without extensive melting such as laser surface texturing on stainless steel substrates was performed. The studies were primarily focused in investigating the influence of the ultrasonic vibrations on the surface texture evolution and its role in improving the tribological performance during steel-on-steel wear upon the external addition of graphene as a lubricant. The studies conclusively showed that ultrasonic vibrations are highly efficient in generating a significantly refined and equiaxed microstructure with superior surface mechanical and tribological properties.

TABLE OF CONTENTS

Chapter Page

Chapter Page

LIST OF TABLES

Table Page

LIST OF FIGURES

Figure Page

Figure Page

Figure Page

CHAPTER I

INTRODUCTION

1.1 Light Alloys

The light alloys are alloys of structural metals that exhibit certain key features such as relatively low density, affordability and low reactivity [1]. The metals that particularly project a remarkable combination of the aforementioned qualities are magnesium, aluminum, and titanium. Alsosince the alloys are almost exclusively used for in structural applications, developing high strength alloys from these metals is a major research focus. It should be noted that in this aspect each of the aforementioned alloys have been reported to respond extremely well to precipitation hardening and hence they have emerged to be the most popular choices for manufacture of light weight components such as airplane, automotive body and sport goods.

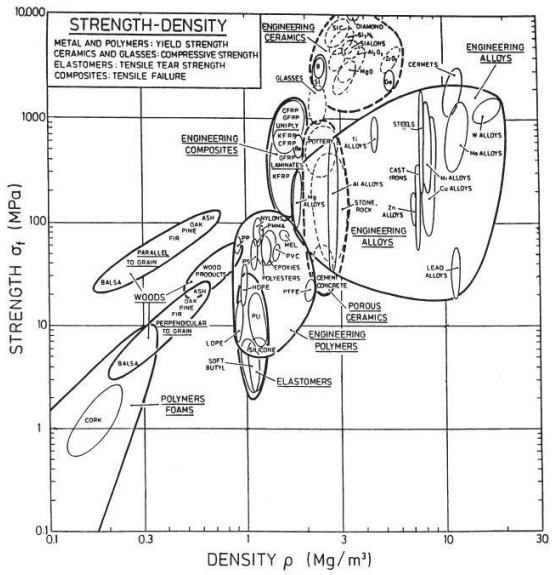

Figure 1.1 Strength vs density chart of popular engineering materials (reprinted from Polmear) [1]

Also, the inherent corrosion resistance of the alloys, particularly of titanium and aluminum dramatically increase their popularity as structural materials. Figure 1.1 illustrates the strength to specific density of major engineering materials, and it can be clearly observed that the 'light alloys' occupy the left-most section of the engineering alloys domain, underlining the ability of the three alloy systems (Mg, Al, and Ti) to be fabricated to high strength low density components. Interestingly, the chart shows materials such as engineering ceramics and composites which exhibit even higher strength to weight ratio. However, the strategic importance of light alloys lies in their high ductility and formability unlike the ceramics and composites whose ductility and formability properties is usually inferior to metallic materials.

1.1.1 Magnesium Alloys

Magnesium alloys are alloys comprising of magnesium as the major alloying element. In addition to magnesium, the most commonly used alloying elements of magnesium are aluminum (3 to 13 per cent), silicon, copper, zinc (0.5 to 3 per cent), and manganese (0.1 to 0.4 per cent). Magnesium exhibits the lowest density among all the structural metals and therefore renders its alloys exceptionally high specific strength (strength to weight ratio). However, it should be noted the lattice structure of magnesium is HCP that is often associated with brittle fracture of the material. The primary reason for this brittle behavior is due to the requirement at least six independent slip systems for the six independent components of plastic strain. Since, usually in HCP crystal structures only the three basal planes (0001) act as slip planes, metals with HCP structure such as magnesium often fail during conventional forming processes such as rolling and are usually manufactured by casting technique [8]. The magnesium alloys exhibit high corrosion resistance, particularly in chemically harsh environment such as saline (marine) environments [9]. In addition to marine applications, magnesium alloys are also particularly desired in automobile applications, as well as manufacturing of high end camera and lenses.

1.1.2 Titanium Alloys

Titanium alloys comprises of the metallic alloys that has titanium as the major material. Titanium alloys exhibit the highest specific strength (strength to weight ratio) as although the density of titanium is higher compared to other structural metals such as aluminum and magnesium, titanium exhibits very high strength, especially precipitation hardenable titanium alloys such as Ti-6Al-4V alloys. Apart from the extremely high specific strength of titanium alloys, the other major features that are particularly desired about titanium is its extremely high corrosion resistance, appreciable formability, and excellent biocompatibility. The high formability of titanium alloys is primarily due to the relatively low c/a ratio (1.587) [10]. It should be noted though that HCP metals are often reported to exhibit brittle behavior due to presence of just three slip planes (basal (0001) planes). However, the relatively low c/a ratio of titanium results in activation the prismatic (1100) and pyramidal (1101) planes for dislocation slip, thereby improving its ductility. Also, while the availability of titanium is fairly adequate (nearly 0.57%), extraction of titanium from its oxide ore it's a highly challenging and expensive process. [11]. Hence, due to the high cost of titanium, its uses are primarily restricted to niche industries that particularly desire its unique attributes and can also afford its high cost. Thus, the majority of application of titanium has been in manufacturing of biomedical implants, aircraft and high end sport cars.

In addition of the HCP crystal structure titanium exhibits in room temperature (known as 'alpha' titanium), it exhibits BCC crystal structure at elevated temperatures (known as 'beta' titanium). Titanium is often alloyed with aluminum, vanadium, molybdenum, and chromium depending on the requirements of the applications. Among the mentioned alloying elements, elements with FCC crystal structure such as aluminum as well as interstitial elements such as oxygen, nitrogen improve the stability of the alpha phase while alloying elements with BCC structure such as vanadium, molybdenum, and chromium improves the stability of the beta phase. Hence, based on the phases exhibited by the alloys, titanium alloys are often classified as alpha, alpha-beta, and beta alloys. It has

been widely accepted that by far the most popular titanium alloy is the Ti-6Al-4V alloy [12]. The addition of aluminum in this alloy is performed to impart solid solution strengthening to the metal as well as reducing its density, while vanadium is added to improve the stability of the beta phase (reduce the alpha to beta transition temperature), and thereby make the alloy heat treatable.

1.1.3 Aluminum Alloys

Aluminum (Al) are alloys comprising of aluminum as the primary metal. It should be noted that although the availability of aluminum is nearly double compared iron on the earth, iron has by far been the dominant metal for engineering applications historically. The preference of iron compared to aluminum has been primarily due to the overwhelming flexibility in extracting iron from its ore (iron oxide) by reducing with carbon. But the high reactivity of aluminum that results in the reaction of aluminum with carbon to form carbide as well as the unusually high affinity of aluminum with oxygen initially posed significant serious challenges concerning its extraction. However, with the advent of Hall-Heroult process and similar techniques, extraction and therefore cost of production of aluminum has been considerably reduced resulting in corresponding exponential increase in its uses. The most commonly cited attributes of aluminum that has driven this spectacular demand of aluminum are ability to strengthen the alloy by precipitation hardening (common alloying elements being copper, magnesium, zinc, and silicon), appreciable formability due to the FCC structure of aluminum, and excellent corrosion resistance due to formation of conformal corrosion resistant layer of Al_2O_3. Furthermore, aluminum has the second lowest density among structural metals (after magnesium) that further increases its value especially in applications requiring high specific strength such as aerospace and automobile. Indeed, it has been reported aluminum alloys comprises nearly 70% of the mass of an average commercial aircraft.

1.2 Laser Surface Engineering of Light Alloys

It has been widely reported that although the light alloys are highly valued for their outstanding bulk properties such as specific strength, corrosion resistance, formability, and weldability, their surface

properties such as wear resistance, surface hardness, and corrosion resistance is often inadequate [13-15]. Hence, improvement of surface properties of light alloys has inspired a number of researchers and therefore has resulted in several investigations. Among these techniques, laser surface engineering of light alloys has been generally accepted to be particularly successful in improving the surface properties of light alloys. The fundamental principle of laser surface engineering involves directing a focused laser beam on a predetermined specific region of the surface of an alloy and subsequently trigger controlled laser-material interactions to introduce physical/chemical transformations at the surface. The physical/chemical transformations that are commonly associated with laser-material interactions are heating, melting, vaporization (ablation), and generation of shock waves by sudden increase in volume of a coated film. The most popular advantages of this novel processing technique compared to conventional processing techniques such as casting are highly localized processing that can restrict the processing primarily in the desired regions, extremely high energy density that in addition to the localized nature of the processing can be used to process local regions before the thermal energy is dissipated within the bulk of the material, extensive process control since lasers can be readily programmed through CNC systems, chemical redistribution at the surface, and ability to generate tailor made microstructures by introduction of alloying/cladding powders in the melt pool are therefore often exploited in laser surface engineering. Naturally, the outcome of the laser processing is heavily dependent on the processing parameters employed during the processing and hence process modeling and optimization of laser processing is a highly researched area. The most important processing parameters that are commonly studied in such optimization/modeling studies are laser irradiation time, absorptivity of the surface, laser spot size, scanning speed etc.

Laser surface engineering can be further classified to the following processes based on the philosophy of the processing technique. The most common laser surface engineering processes are laser surface melting (LSM), laser surface alloying (LSA), laser shock peening (LSP), and laser composite surfacing (LCS). Each of the aforementioned processes primarily involve achieving controlled laser-

material interactions at the surface such as melting, introduction of alloying elements/ hard ceramic particles in the melt, rapid vaporization of a liquid film on the surface to generate compressive stresses. It should be noted that laser surface melting, laser surface alloying, and laser surface cladding involve melting of the substrate followed by resolidification of the melt pool. Now, it has been generally accepted that the cooling rates associated with laser processing is extremely high as while the laser interaction results in very local melting of the substrate, the bulk remains unaffected and cold. Thus, upon the removal of the laser spot, the unmelted bulk of the substrate aggressively withdraws the heat from the melt pool resulting in cooling rates of the order of 10^5-10^{11} K/s [16]. Furthermore, since the grain sizes of resolidified regions are significantly influences by undercooling, the high cooling rates associated with the laser processing results in a corresponding increase in undercooling and hence reduction in grain size. Hence, laser surface engineering processing that involves melting of the substrate is almost always associated by the formation of a highly refined dendritic microstructure. A detailed description of the popular laser surface engineering processes is provided henceforth.

1.2.1 Laser Surface Melting (LSM)

Figure 1.2 presents a schematic diagram of the fundamental features of the laser surface melting process. As depicted in the schematic, laser surface melting primarily comprises of using a high power laser beam to melt a localized zone of the substrate. Subsequently, upon the removal of the laser beam, the unmelted bulk act as a quenching heat sink, thereby triggering rapid cooling and solidification of the melt pool. Several investigations have reported that the cooling rates for laser surface melting processing are often in the of 10^5-10^{11} K/s, and thereby promotes the formation of a highly refined dendritic microstructure with extensive elemental redistribution [17]. Also, since the basic principle of laser surface melting involves remelting of the surface without addition of alloying elements or hard ceramic phases on the melt pool, this process has not been extensively used to improve surface hardness and subsequently tribological studies of laser surface melted substrates has also been highly limited. However, since this process is highly efficient in elimination/reduction of second phase particles due

to homogenization of the remelted region, it has been one of the most popular processing techniques to improve surface corrosion resistance of materials. The major reason for the improvement in corrosion resistance is the elimination/reduction of second phase particles result in decrease in formation of microgalvanic corrosion cells and thereby improving the corrosion resistance.

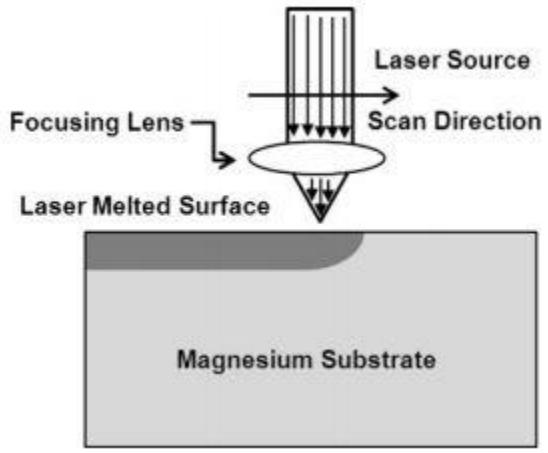

Figure 1.2 Schematic diagram representing LSM (reprinted with permission) [2]

1.2.2 Laser Composite Surfacing (LCS)

A schematic representation of the laser composite surfacing process is presented in Figure 1.3. In this process, a high power laser beam is employed to melt the surface of the substrate and subsequently hard ceramic particles are introduced in the melt pool, with the resulting surface being comprised primarily of a ceramic reinforced metal matrix composite that is highly distinct from the substrate. The introduction of the hard ceramic particles is achieved by either injection of the particles by forcing the particles in the molten pool with an assist gas (usually argon) or placement of the particles on the surface, usually with a binder and subsequently melting the substrate with a laser beam while the particles penetrate the melt pool due to action of gravity. Also, in addition to these methods that operates by the introduction of the particles externally, development of surface composites using *in-situ* methods have also been reported. In this technique, reactants instead of chemically inactive particles is injected in the melt pool that reacts with the molten metal, triggering chemical reactions and

thereby resulting in the formation of hard particles. This process is particularly effective if the metallic substrate has high affinity for the injected reactants and also the resulting phases are chemically stable and hard. Naturally, due to the extraordinary affinity of titanium to form hard nitrides and oxides with nitrogen and oxygen respectively, the most cited research on *in-situ* laser composite surfacing has been in laser surface nitriding of titanium. *In-situ* composite surfacing holds distinct advantage over *ex-situ* surfacing as this the resulting metal matrix surface composite exhibits significantly higher particle-matrix bonding compared to *ex-situ* surfacing.

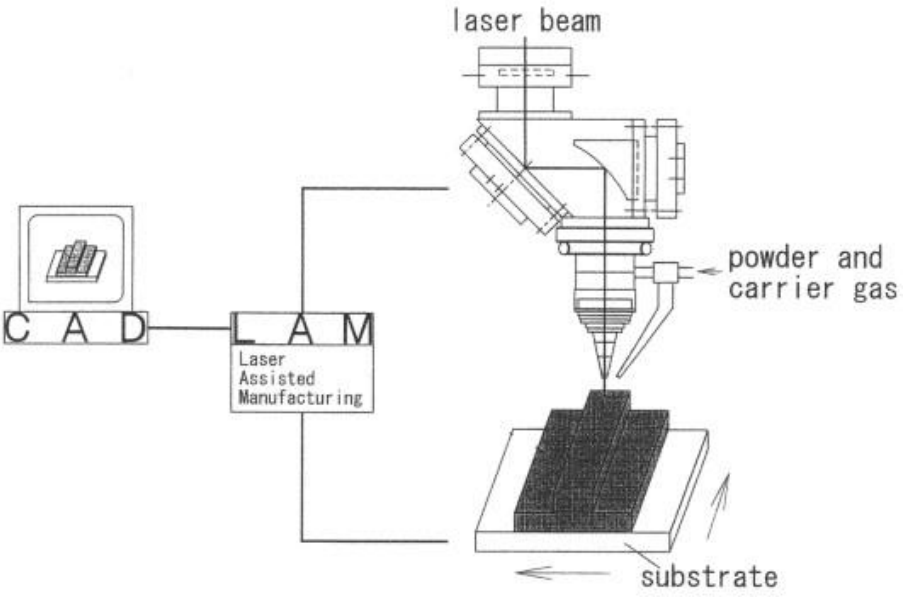

Figure 1.3 Schematic diagram of laser surface cladding (reprinted with permission) [3]

1.2.3 Laser Surface Alloying (LSA)

A schematic representation of the laser surface alloying process is presented in Figure 1.4. This process is highly similar to laser composite surfacing processing wherein external powders are injected in the melt pool. However, compared to laser composite surfacing that employs injection of hard ceramic particles in the melt pool, laser surface alloying involves injection of metallic powders. Also, while the hard ceramic particles do not extensively react with the melt pool, the metallic powders often undergo extensive intermetallic reactions resulting in the formation of hard intermetallic phases. Now,

since these phases form *in-situ* in the matrix, the resulting alloyed surface often exhibits extraordinary particle matrix bonding. Also, the introduction of the hard intermetallic phases in the melt pool almost always results in notable increase in the surface hardness. Furthermore, since wear resistance, especially abrasive wear resistance is highly dependent on the surface hardness of the substrate, laser surface alloying has emerged as a highly promising technique to improve surface hardness and wear resistance of the substrate.

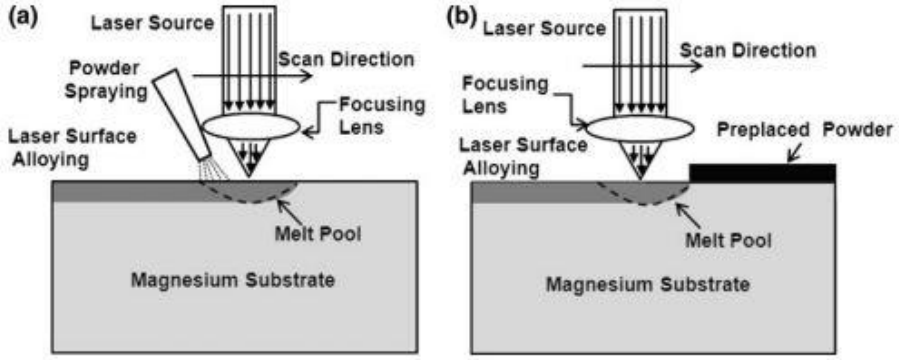

Figure 1.4 Schematic representation of laser surface alloying of magnesium alloys using (a) powder spraying, and (b) preplaced powder approach (reprinted with permission) [2]

1.3 Ultrasonic Vibration-Assisted Material Processing

Ultrasonic vibration-assisted material processing is the application of ultrasonic vibrations during processing of materials, and this novel processing has recently gained significant popularity. For instance, successful application of ultrasonic vibrations in solid state machining processes to improve machining efficiency, superior surface finish in machining applications such as grinding, drilling has been reported and has been largely attributed to change from brittle-to-ductile behavior, enhanced chip removal etc. In liquid state processing such as ultrasonic vibrations assisted solidification as well, the unique features such as grain refinement, superior elemental distribution has been successfully exploited in processing of materials with superior mechanical and electrochemical properties has shown extremely promising results. For instance, in the shielded melting arc welding studies performed with and without ultrasonic vibrations on AISI 304 stainless steel by Cui *et al* [18]. The authors reported

that the columnar dendritic microstructure reduced from about 95% to 10% as ultrasonic vibrations power output was increased from 0% (no-ultrasonic vibrations) to 90%. The transition of the resolidified grains from columnar dendritic structure to equiaxed with the application of ultrasonic vibrations (Power: 600W, Freq: 19 kHz) during argon shielded arc welding of ferritic stainless steel had been reported by Watanabe *et al*. [4] especially in the higher welding speed samples, as can be observed from Figure 1.5. Not only in heavier metals like steel, such reduction in grain size was also observed in one order of magnitude reduction (from 26μm to 2 μm) in grain size of eutectic silicon was reported in the investigations on the cast structure of A356 (7% Si, 0.3% Mg, balance Al) alloys by Jian *et al.* [19] on the application of ultrasonic vibrations (frequency: 20 kHz; amplitude: 56.7 μm) compared to their as-received counterparts. Such improvement in grain size in both the α-Al phase as well as the eutectic Si hypoeutectic LM6 Al-Si alloys has also been reported by Das *et al* [20]. Similar improvements in grain sizes and changes in grain morphology have been reported in hypereutectic and wrought Al systems [21, 22].

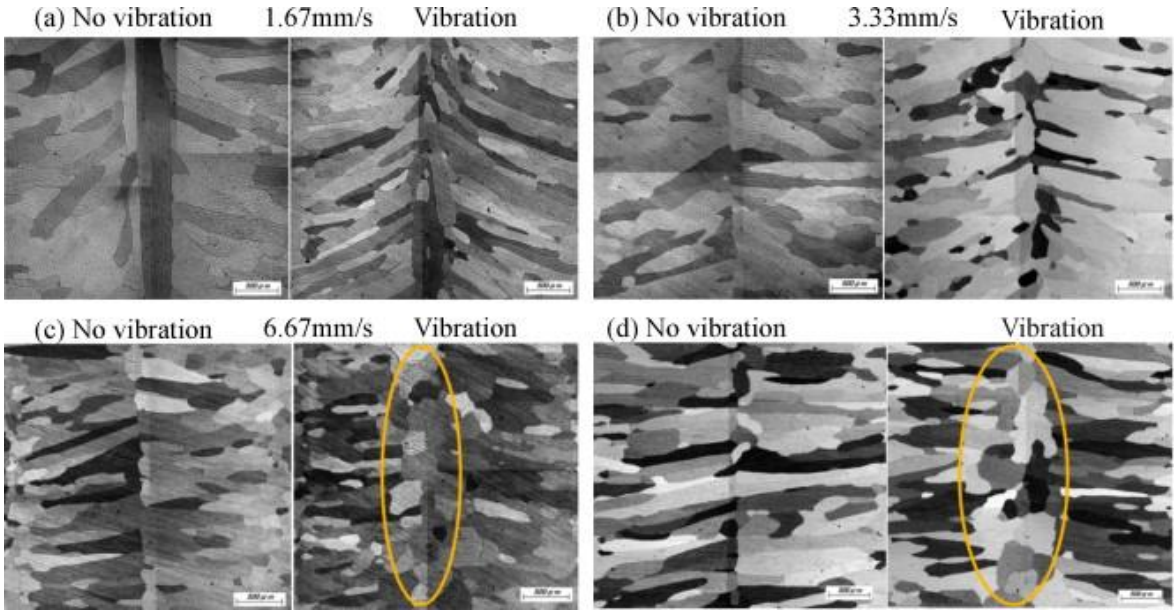

Figure 1.5 Transition of microstructures from columnar dendritic to equiaxed with application of ultrasonic vibrations in argon shielded arc welding of ferritic stainless steel at a welding speed of (a) 1.67 mm/s, (b) 3.33 mm/s (c) 6.67 mm/s, and (d) 10 mm/s (reprinted with permission) [4]

The authors reported that the average size of the α-Al and eutectic Si plates decreased from about 1500 μm to nearly 70 μm and about 55 μm to 8 μm respectively. A summary of the alloy systems, experimental details, input parameters, and results have been presented in Table 1.1.

Table 1.1 Summary of some of the major achievements in ultrasonic vibrations assisted solidification processing of metallic materials

Research group	Alloy systems	Experimental details	Input parameters	Results
Cui *et al.* [18]	AISI 304 Stainless Steel	Shielded melting arc welding	0% to 90% of ultrasonic vibrations input power	Columnar dendritic structure reduced from 95% to 10%
Watanabe *et al.* [4]	Ferritic Stainless Steel	ultrasonic vibrations assisted argon shielded arc welding of ferritic stainless steel	ultrasonic vibrations Power of 600W, Freq: 19 kHz	Grain refinement, transition of weld microstructure from columnar to equiaxed
Jian *et al.* [19]	A356 (7% Si, 0.3% Mg, balance Al)	ultrasonic vibrations assisted casting	(frequency: 20 kHz; amplitude: 56.7 μm)	Grain size of eutectic silicon from 26μm to 2 μm
Das *et al.* [20]	hypoeutectic LM6 Al-Si alloys	ultrasonic vibrations assisted casting	20 kHz frequency and amplitude of 25 μm	α-Al and eutectic Si plate size decreased from about 1500 μm to nearly 70 μm and about 55 μm to 8 μm
Feng *et al.* [21]	Hypereutectic Al-23% Si	ultrasonic vibrations assisted casting		Grain refinement of α-Al and Si

Since grain refinement is the only mechanism where one can achieve improvement in strength as well as toughness, use of ultrasonic vibrations in achieving grain refinement strengthening has been reported in recent investigations. The major mechanism associated with ultrasonic vibrations has been reported to be primarily a combination of cavitation and hydrodynamic stress associated dendrite

fragmentation. As rapid melting/solidification is encountered during several laser manufacturing processes such as surface modification (laser melting, alloying, cladding, and composite surfacing), forming (laser welding/joining), and material removal (laser machining) processes, the application of ultrasonic vibrations during laser processing presents a great potential for improving the microstructure, metallurgical quality, and material removal rates of the processed materials.

1.3.1 Ultrasonic Vibration-Assisted Laser Drilling

Laser drilling essentially involves the process of material removal by employing a focused laser beam on a substrate to create a melt pool and subsequently ejecting it. The primary features that are considered to be particularly crucial and therefore often used to quantify the quality of the machining operation are the drilled hole depth, width, taper angle, and recast layer thickness. The melting and ablation associated with laser irradiation results in formation of a vapor capped liquid pool that is ejected as the vapor pressure of the vapor cap pushes the liquid. However, the vapor pressure developed due to ablated substrate is rather limited and therefore is often compensated with additional forces, such as assist gas pressure and mechanical vibration. The assist gas is an inert gas (usually argon) used to create generate a protective environment around the melt pool to avoid undesirable reactions such as oxidation, nitrogen or moisture pick up. It should be noted that apart from creating a protective environment, assist gas has also been successfully employed to result in (3-8 times) increase in melt removal rate efficiency. However, the gas pressures that was employed to achieve the appreciable increase was considerably higher, thus making the processing expensive and complicated. Hence, use of mechanical forces through vibrations to facilitate melt ejection during laser drilling has also been extensively investigated by several research teams. For instance, about three to four fold increase in ejection rate was observed in the vibration-assisted laser drilling experiments by Park *et al* [23, 24]. However, the vibrations frequency employed in the investigations was lower than ultrasonic range.

The initial successful application of ultrasonic vibrations on laser processing of materials was reported on laser drilling of materials. The first scientific investigations of the ultrasonic vibration-

assisted laser drilling was published in 1975 by Mori *et al* [25]. The experiments were performed in aluminum, stainless steel, and brass substrates vibrating with a frequency of 20 kHz, irradiation energy of 5 J, pulse duration of 0.6 and 2 ms, and amplitude of 20 and 40 μm. The authors investigated the effect of the alloy composition, amplitude and pulse duration on the hole quality. It was observed that increase in amplitude results in an improvement in hole quality, that is, larger hole depth, less taper and higher hole width, and this improvement was more pronounced in the lower melting aluminum than the higher melting steel and brass substrates. The authors also commented on the possible ejection mechanism by placing a mercury droplet (with physical properties comparable to molten substrates) on the vibrating probe that resulted in atomization and subsequent ejection of the melt, and hence concluded that the melt ejection mechanism should be similar.

It should be noted that in the previous investigation, the effect of ultrasonic vibrations was primarily considered as an ejection force amplifier, and the effect of ultrasonic vibrations in the physical properties such as local effective density and laser absorptivity was not considered. The effect of the aforementioned local effective density and laser absorptivity in the efficiency of ultrasonic vibrations in laser drilling was incorporated and studied on Al based metal matrix composites (Al-Li alloy reinforced with 20% SiC by vol. and Al-Mg alloy reinforced with 20% Al_2O_3 by vol.) by Lau *et al* [26]. The experiments were performed with a pulsed 120 W Nd:YAG laser (pulse time of 2 ms), and ultrasonic probe frequency of 20 kHz. The authors predicted that the maximum drilled hole length (z_{max}) during the laser drilling process from a Gaussian heat source due to pure laser ablation (eq 1.1). The effect of ultrasonic vibrations in the mathematical formulation was incorporated by the local effective density changes that are triggered by the standing waves associated with ultrasonic vibrations (eq 1.2). Again, since laser absorptivity is a function of local effective density (eq 1.3), the authors calculated the total difference in maximum depth of drilling that can be achieved due to incorporation of ultrasonic vibrations (eq 1.4).

$$z_{max} = \frac{1}{\alpha} \ln \frac{I(0,0)}{I_t} \quad (1.1)$$

$$\rho' = \frac{\rho}{1 + \frac{4\pi a}{\lambda} \cos\frac{4\pi Z}{\lambda} \cos \omega t} \quad (1.2)$$

$$\alpha' = \frac{\alpha}{1 + \frac{4\pi a}{\lambda} \cos\frac{4\pi Z}{\lambda} \cos \omega t} \quad (1.3)$$

$$z'_{max} - z_{max} = B \sin \frac{4\pi z'_{max}}{\lambda} \quad (1.4)$$

Here, I(0,0) is the intensity at irradiation point, I_t is the threshold intensity for ablation, ρ and ρ′ are the bulk and local effective density respectively, λ and a are the wavelength and amplitude of standing wave respectively, α and α′ are laser absorptivity in static and vibrated substrate respectively, and B is a material constant. Now, since the laser drilling process not only involves ablation of the material but also melt ejection, the authors hypothesized that the improved ejection efficiency exposes unmelted surface that is eventually ablated by the laser beam, and hence the melting process complements the ablation. Also, as reduction in recast layer thickness (due to reduction in melt volume) is a direct consequence of the improved melt ejection, the authors measured the reduction in recast layer to validate the hypothesis. The experimental evidences also supported the hypothesis, and it was observed that the recast (written as over-reacted zone) layer of the Al-SiC composites decreased in the ultrasonic vibrations assisted laser drilled materials (from 20 μm in samples processed without ultrasonic vibrations 5 μm in the ultrasonic vibration-assisted laser drilled samples). Also, it was observed that the recast layer comprised of needle-like phases (carbides of aluminum, eutectic silicon), that are brittle and hence deteriorate mechanical properties. Similarly, due to ejection of melt, the total thermal energy in the material decreased resulting in reduction of heat affected zone (the ultrasonic vibration-assisted drilled samples exhibiting about 30% smaller HAZ than the as received materials). However, the authors also reported that the HAZ in the ultrasonic vibration-assisted samples exhibited higher porosity. It was concluded that the higher porosity was primarily due to selective ejection of the aluminum matrix while the reinforcing ceramic particles (SiC whiskers) remained unmelted and therefore unremoved.

The drilling process was subsequently modelled using finite element modeling (FEM), and the drill profile (depth, width, taper angle) and recast layer thickness was predicted [5]. The governing heat equation that for the thermal model was the heat equation based on a polar co-ordinate system (eq 1.5). The boundary conditions of the drilling process was based on assuming that heat conduction dominates the heat transfer process (and thereby neglecting heat convection) and temperature dependent values of thermal conductivity, density, and specific heat was employed. Also, the vaporization of the molten material was simulated by considering an element to be vaporized if its temperature exceeds the melting point and not undergoing element death to simulate the gas-liquid heat transfer. The melt expulsion was considered as a consequence of the difference in surface tension due to temperature gradient in the laser melted region (eq 1.6) and the recoil pressure (eq 1.7), with the expulsion being resisted due to viscous drag (eq 1.8). Since, the application of ultrasonic vibration significantly increases the recoil pressure (P_r), the required velocity of an element (U) in the force balance equation also increases (eq 1.9) and was calculated in the finite element modeling simulations. Finally elimination of the melt was considered if the height of melt ejection (ejection velocity of the melt multiplied with effective time of ejection) exceeded the height of the drilled hole. The authors also considered the vapor point shift (ΔT_b) due to the action of recoil pressure (ΔP_t) as described in eq 1.10. The authors (using aforementioned physical equations) simulated the effect of ultrasonic vibrations on final hole depth and recast layer thickness (volume of non-ejected melt) of steel substrate materials at two different initial hole depths. Also, the temperature profile around the hole was computed to predict the heat affected zone and verified with experimental evidence [5]. The experimental setup involved employing a Ti-sapphire laser (λ =775 nm) with a pulse of 240 fs with a repetition rate of 1 kHz, and the substrates (Nitinol: 50.6 % Ni and 49.6% Ti) were vibrated with a frequency of 40 kHz and vibration amplitude of 2.5μm. The authors examined the effect of ultrasonic vibrations on the quality of the micromachined holes and recast layer microstructure.

$$\frac{\partial T}{\partial t} = k\left(\frac{\partial^2 T}{\partial r^2} + \frac{1}{r}\frac{\partial T}{\partial r} + \frac{1}{r^2}\frac{\partial^2 T}{\partial \theta^2} + \frac{\partial^2 T}{\partial z^2}\right) + \frac{Q}{\rho c} \quad 1.5$$

$$F_t = \frac{d\gamma}{dr} \times A_s \quad 1.6$$

$$F_r = \frac{dP}{dr} \times V \quad 1.7$$

$$F_f = \eta \times A_s \times \frac{dU}{dy} \quad 1.8$$

$$F_f - F_r - F_t = 0 \quad 1.9$$

$$\Delta T_b = \Delta P_r \times \frac{dT}{dP} \quad 1.10$$

Here, eq. 1.5 is the heat transfer equation, $\frac{d\gamma}{dr}$, A, $\frac{dP}{dr}$, V, η, U are the surface gradient, area, pressure gradient, volume, viscosity, and velocity of simulated element respectively, ΔP_r is the recoil pressure and P is the vapor pressure at a temperature of T. The application of ultrasonic vibrations was simulated by increasing recoil force (F_r) from 12 kN to 160 kN in 0.3 mm initial hole and 6 kN to 200 kN in 1.3 mm initial hole for the non-vibrated and vibrated samples respectively. The equations conclusively demonstrated that the increase in recoil pressure due to ultrasonic vibrations resulted in increase of hole depth from about 1 mm to nearly 1.75 mm as well as reduced heat affected zone thickness by almost four times in the vibrated samples, and has been presented in Figure 1.6. The effect of ultrasonic vibrations on laser microhole machining of Nitinol substrates was studied by Zheng *et al.* [6]. The effect of superior control associated with extremely short laser pulse time (< 10 ps) and the superior melt ejection associated with ultrasonic vibrations was explored. The ultrasonic vibrations was observed to result in significant refinement of grain-size in the recast layer as compared to the non-vibrated samples that exhibited comparatively columnar grains, presented in Figure 1.7(a). The ultrasonic vibrations assisted drilled specimen also resulted in superior quality of drills, with drill length increasing from 1.65 mm to 1.95 mm with application of ultrasonic vibrations, as well as reduction in taper angle from 56 to 50, as can be observed from Figure 1.7(b).

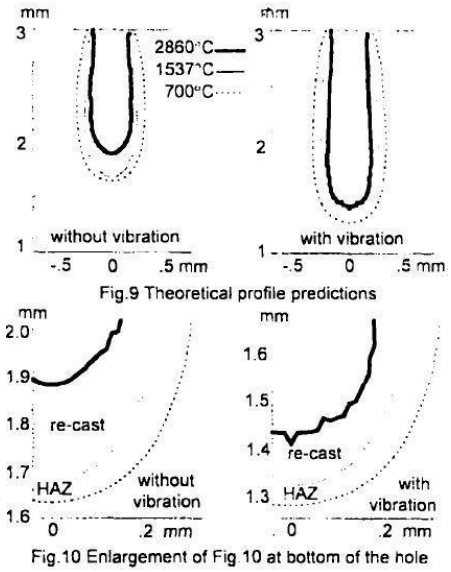

Figure 1.6 Theoretical predictions of drilled holes, and HAZ with and without ultrasonic vibrations in steel substrates (reprinted with permission) [5]

Laser drilling, particularly with short pulse duration has often been reported to exhibit poor surface quality due to redeposition of the ejected particles on the substrate surface. The agglomeration and redeposition of the ejected particles has been associated with heating of the particles that promote diffusion and adhesion. The ultrasonic vibrations have been reported to increase convection heat transfer as it increases turbulence of the air/plasma (surrounding the laser irradiated zone). Hence, the efficiency of ultrasonic vibrations in developing superior surface quality in laser drilling was investigated by Kang *et al* [27]. The researchers used tempered steel as substrate material (ASTM W110), a nanosecond pulsed fiber laser (λ = 1070 nm, pulse energy = 0.1 to 1 mJ, pulse duration = 200 ns, and spot size = 10 μm and 25 μm), and the vibrating module (frequency ≈ 30 kHz, amplitude = 3 μm). The ultrasonic vibration-assisted drilled substrates were reported to be particularly effective in improving surface quality (determined by measuring particle density on surface), with higher pulse energy (1 mJ compared to 0.5 mJ, spot size of 25 μm), and ineffective for lower spot sizes, with higher pulse energy (10 μm).

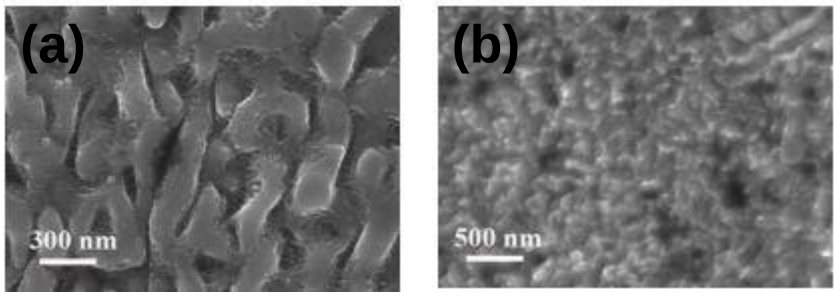

Figure 1.7 Microstructure of material deposited on the walls generated by laser drilling: (a) without and (b) with ultrasonic vibration assistance (reprinted with permission) [6]

The former observation was attributed to the increased tendency of agglomeration of nanoparticles with increased pulse energy, resulting in increase in deterioration of surface quality in the laser drilled samples without ultrasonic vibrations that rendered the effect of ultrasonic vibrations in improving surface quality more distinct. The inefficiency of ultrasonic vibrations in improving surface quality of laser drilled samples with lower spot sizes was attributed the considerable increase in energy density in the lower spot size laser drilled samples (6.25 times). The aforementioned extensive increase was concluded to overwhelm the enhanced cooling effect of the ultrasonic vibrations. The investigation also reported the laser cutting of the substrate with and without the application of ultrasonic vibrations that exhibited similar trends of improved surface finish on the machined sidewalls with the ultrasonic vibration-assisted laser drilled samples. The enhanced cooling associated with ultrasonic vibrations were also reflected in the elemental analysis of the laser machined sidewalls (using EDS) that exhibited considerable reduction in oxide formation (from 30.9 atomic % in the without ultrasonic vibration specimen to 11 atomic % in the with ultrasonic vibration specimen) due to increased cooling rate that reduced oxygen diffusion in the melt particles.

The use of ultrasonic vibrations assisted laser drilling of stainless steel using continuous wave mode CO_2 laser was reported by Alavi *et al* [28]. The effect of increase in ultrasonic vibration amplitude on the drill quality (drill length, aspect ratio, and taper angle) was investigated. The experiments were performed on 316 stainless steel with a laser power of 900 W, laser head to sample distance of 5 cm

and 1.5 cm, ultrasonic vibration frequency of 20 kHz and amplitude of 23, 37, and 51 μm. The authors reported that for higher laser head to sample distance (focal distance) of 5 cm, laser drilling without ultrasonic vibrations did not result in any melt expulsion and the ultrasonic vibration-assisted laser melted samples resulted in formation of deep craters on the surface. The depth of the craters were observed to decrease with increase in ultrasonic vibration amplitude (320 μm, 310 μm, and 270 μm crater depth for 23 μm, 31, and 51 μm amplitude respectively). The decrease in depth of craters was attributed to the delayed onset of melt expulsion due to the enhanced convection cooling effect associated with ultrasonic vibrations, similar to observations of Kang *et al* [10]. The samples drilled with lower laser head to sample distance (1.5 cm), however, exhibited significantly larger aspect ratio holes. The lowering of laser head to sample distance was reported to result in significant melt expulsion, as was evident from the heavy material build up in the ultrasonic vibration-assisted laser drilled samples.

The mechanism of formation of deep craters (blind holes) in the ultrasonic vibration-assisted laser drilled specimen (with higher laser head to sample distance of 5 cm) was further investigated by Alavi *et al.* [29]. The study was primarily to establish the effect of increased convectional cooling associated with ultrasonic vibrations on the delay of onset of melting and subsequently melt expulsion. The experiments were performed on stainless steel substrates with a continuous wave CO_2 laser (laser power = 900 W, focus distance = 5 cm, irradiation time of 0.3s, 0.4s, and 0.45s respectively) and the amplitude of ultrasonic vibrations employed were 23 μm, 31, and 51 μm respectively. The authors reported that while the laser drilled samples without ultrasonic vibrations exhibited distinct melt zone (but virtually no expulsion, hence more reminiscent to laser melting experiments), the ultrasonic vibration-assisted laser drilled sample for shorter irradiation time (0.3 s) exhibited complete absence of melt zone and only heat affected zone was observed. The absence of melt zone was attributed with the delay of onset of melting due to enhanced conventional cooling associated with ultrasonic vibrations. Also, the ultrasonic vibration-assisted laser drilled sample for longer time scales (0.35 s and 0.45 s)

exhibited melt zone formation indicating onset of melting occurred between 0.3 s to 0.35 s of irradiation time. Also, similar to their previous investigation, the depth of crater was observed to decrease with increase in ultrasonic vibration amplitude for both 0.35 s (crater depth being 257 μm, 190 μm, and 105 μm for 23 μm, 37 μm, and 51 μm vibration amplitude) and 0.45 s (crater depth being 320 μm, 300 μm, and 270 μm for 23 μm, 37 μm, and 51 μm vibration amplitude) laser treated samples. Hence, while increased convectional cooling decreased melt volume and therefore crater depth, increasing irradiation time was observed to increase crater depth due to higher melt volume. The microstructural characterization of the laser irradiated samples without ultrasonic vibrations displayed a combination of columnar dendritic grains (at the melt interface, dendritic arm spacing = 2.2 μm) and equiaxed grains (at the interior of melt zone, grain size = 3-5 μm), the laser irradiated samples with ultrasonic vibrations exhibited completely equiaxed or short dendritic microstructure with an average grain size of 1.6 μm. Hence, it was concluded that the ultrasonic vibrations were effective in both delaying the onset of melting as well as development of equiaxed refined microstructure. Ultrasonic vibration-assisted laser melting, as reported earlier, was observed to be more effective in generating deeper holes under the more focused beams (lower focal length). The increase in ultrasonic vibration amplitude was observed to increase aspect ratio, hole depth, and decrease hole diameter meaning and taper angle, meaning deeper and straighter holes could be machined with application of ultrasonic vibrations, as presented in Figure 1.8.

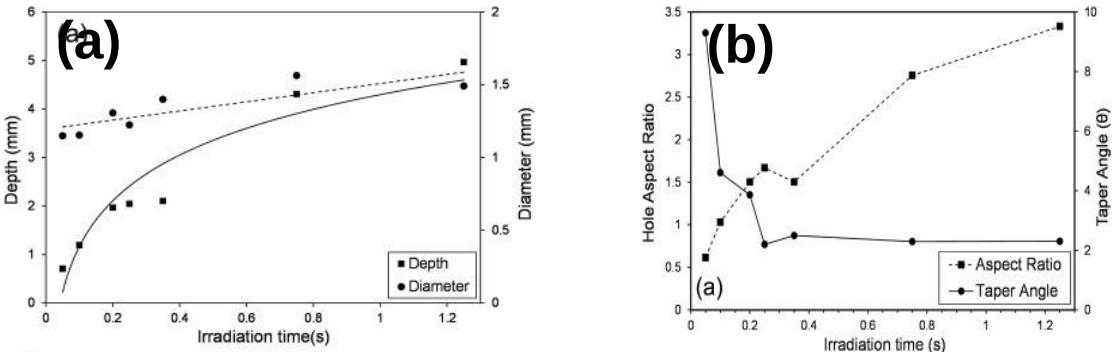

Figure 1.8 Variation of (a) hole depth, diameter, and (b) aspect ratio, and taper angle with irradiation time (reprinted with permission) [31]

The investigation of the effectiveness of ultrasonic vibrations in (aforementioned) higher focused conditions was further extended on the geometry of drilled holes (hole depth, diameter, and taper angle) as well as quality of drilling (material build-up, spatter, recast layer thickness, and heat affected zone) [30]. Also, effect of time in hole evolution was studied using high speed photography and the theoretical mechanism of melt ejection was explored using finite element modeling. The investigation was performed with a continuous wave CO_2 laser (λ = 10.6 μm, focus length = 1.5 mm) on 316 stainless steel substrates with varying irradiation time (50, 100, 200, 250, 350, 750, 1250 ms) with an ultrasonic vibration frequency and amplitude of 20 kHz and 23 μm. The high speed camera photography revealed that while laser irradiation results in heating and subsequently melting of material (indicated by formation of bright spot), the first ejection of a melt droplet was noticed at a time of 2-2.125 ms post bright spot formation meaning that melt volume must reach a critical size before being able to eject. The effect of irradiation time on laser drilled holes were observed that with increase in irradiation time hole depth and aspect ratio increased due to higher melting and therefore higher melt ejection. However, as the holes get deeper with increased melt time, ejection of the droplets get increasingly more difficult, decreasing drill rate. The effects of increase in melt ejection with increase in irradiation time was also reflected in the quality parameters that exhibited increase in resolidified build up material and splatter with deeper holes (longer irradiation time samples). Finite element modeling was employed to establish the mechanism of hole formation and temperature distribution, with the experimental data used as numerical constraints. The thermal modeling indicated that the onset of melting occurs at about 1.53 ms of irradiation, and since the first droplet ejection occurred at about 2.2 ms, the difference of 0.67 ms was concluded to be the time required for the melt volume to reach the critical volume to undergo ejection, and was calculated to be 1.82×10^6 μm^3.

The previous investigation was primarily directed towards establishing the irradiation time on ultrasonic vibration-assisted laser drilling of materials. The authors also reported the effect of focus distance on hole depth and quality under similar processing conditions (identical substrate, laser

wavelength, power, ultrasonic vibration frequency, and amplitude) [31]. The following focus distances: 15 mm, 25 mm, 35 mm, 50 mm and a constant irradiation time of 0.4 s was reported for this investigation. The laser drilled holes exhibited increase in taper angle and decrease in hole depth with increase in focus distance, in all the samples other than the 50 mm (that exhibited very shallow craters). The authors concluded that the decrease in hole depth was primarily a consequence of decrease in power density with increase in focus distance that delayed formation of critical melt volume discussed in their previous investigation. Also theoretical prediction of melt volume was performed using finite element modeling. It was assumed that the critical melt volume for each experiment was equal, and hence, similar to the method mentioned in the previous study, the time for initiation of melting was predicted and compared with experimental data.

1.3.2 Ultrasonic Vibration-Assisted Laser Melting

Laser melting involves using a high power laser beam to melt a localized zone of a substrate and exploit the heat extractability of the unmelted zone to initiate rapid quenching and resolidification of the melt pool. The rapid resolidification results in significant undercooling of the melt pool, resulting in formation of a very refined dendritic microstructure as well as elemental redistribution. While the refined microstructure associated with laser melting gives it a distinct advantage, it is also associated with directionality (due to strong solidification texturing), non-uniform properties (corrosion resistance), as well as defects such as microsegregation, porosity, and tendency to undergo cracking. Hence, the hydrodynamic and cavitation stresses associated with ultrasonic vibrations is expected to naturally result in improved microstructural features such as further refined and equiaxed grains. However, the laser melting of materials under the influence of ultrasonic vibrations are relatively challenging as the inherent dynamic nature of the melt due to the turbulence associated with the ultrasonic vibrations. Unlike conventional casting, laser melting involves formation of a localized melt pool, hence melt ejection (that is highly desired for drilling experiments) is often possible and therefore the amplitudes of the ultrasonic vibrations are often considerably smaller than laser drilling

counterparts. It should be mentioned that due to the lower amplitudes employed (to avoid melt ejection), it also reduces the melt turbulence that dictates the hydrodynamic stresses and their corresponding implications such as dendrite fragmentation, and grain refinement. The aforementioned processing challenges are most likely the major reason that ultrasonic vibration-assisted laser melting has only recently attracted significant research interests.

The hardening associated with grain refinement generated by ultrasonic vibration-assisted laser melting was also observed by Zhou *et al* [7]. The authors reported the effect of the aforementioned hardening (due to laser melting with and without ultrasonic vibrations) on the tribological properties of cold work tool steel (Cr12MoV steel) using an optical fiber laser (power = 1800 W, scanning speed = 700/min) and an ultrasonic vibration source with an amplitude of 20 μm and frequency of about 20.5 kHz. The authors reported that the without ultrasonic vibration-assisted specimen exhibited a highly textured microstructure dominated by columnar cellular grains, particularly at the melt interface that experiences the highest thermal gradient (due to the heat extraction from the surrounding unmelted zone) and lowest solidification rate. The ultrasonic vibration-assisted laser melted samples, however, exhibited a highly refined microstructure that was considerably equiaxed although was not completely devoid of dendritic grains, as presented in Figure 1.9. The mechanical implications of this refinement was also observed in the mechanical properties, with the without ultrasonic vibration-assisted laser melted samples exhibiting lower hardness (varying from 310 to 425 HV) than the with ultrasonic vibration counterpart (varying from 401 to 453). The tribological properties also followed similar trend, with the ultrasonic vibration-assisted laser melted samples exhibiting an average coefficient of friction of 0.24 compared to the without ultrasonic that exhibited 0.36, indicating reduction in adhesive wear, also confirmed from analysis of wear track. Similarly, wear loss also reduced with ultrasonic vibration-assisted laser melting (wear depth reducing from 10.4 μm in the without ultrasonic samples to about 7.8 μm in the with ultrasonic samples), underlining the efficiency of ultrasonic vibrations.

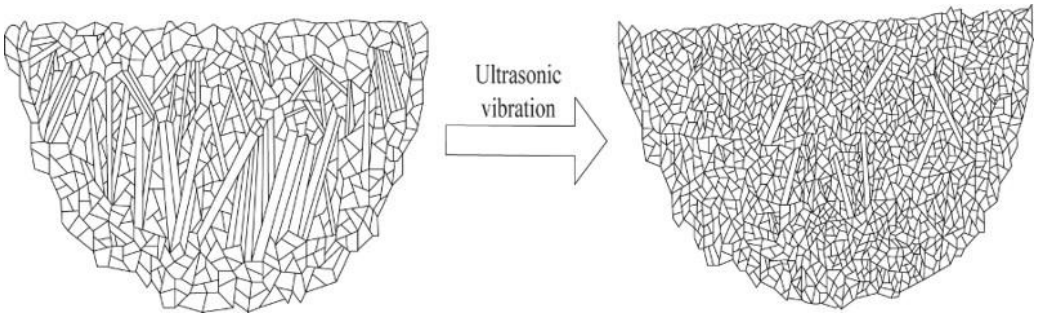

Figure 1.9. Microstructural evolution of laser melted Cr12MoV cold die steel (a) without ultrasonic vibrations, and (b) with ultrasonic vibrations (reprinted with permission) [7]

1.3.3 Ultrasonic Vibration-Assisted Laser Surface Cladding

The dendrite fragmentation associated with grain refinement is not only effective for melting of bulk substrates but also powders. This was observed in the ultrasonic vibration-assisted laser surface cladding of Ti-6Al-4V substrates with yttria stabilized zirconia coatings. The authors employed a Nd:YAG laser (power = 400 W, scan speed = 200 mm/min) and ultrasonic vibration frequency of 40 kHz and maximum amplitude power of 1 kW. The authors observed that application of ultrasonic vibrations resulted in increase in melt of depth of substrate (from 318 μm to 430 μm) and decrease in clad thickness (from 533 μm to 380 μm). The increase in melt depth was attributed to improved convection heat transfer in the melt due to the acoustic streaming associated with ultrasonic vibrations. The elemental distribution (using EPMA) confirmed that the ultrasonic vibrations resulted increased migration of titanium atoms into the yttria stabilized zirconia coating that resulted in dilution of the coating (from 37.37% in without ultrasonic to 53.09% in with ultrasonic samples).

The efficiency of ultrasonic vibrations in developing refined equiaxed microstructure has been a common observation in the various scientific efforts cited in this study. The influence of the microstructural refinement on their macroscopic properties was investigated by studying the hot corrosion behavior of ultrasonic vibration-assisted laser surface cladded yttria stabilized zirconia coatings [32]. The investigation was performed using a pulsed Nd:YAG laser (power = 5.2 J, spot diameter = 3 mm, scanning speed = 5 mm/s, and pulse duration = 1 ms) and ultrasonic power source

(frequency = 20 kHz, amplitude = 0%, 20%, 30%, and 50% of 2600 W peak power). The investigations revealed that the melt pool experiences turbulence from two distinct physical phenomenon. The first phenomenon is the periodic switching on and off of the laser pulse that influences the surface tension, generating unbalanced surface force, and the second obviously being the acoustic streaming and cavitation associated with ultrasonic vibrations. The combination of the two forces indicated to counter each other, as observed from the surface roughness measurements (Ra, a direct indication of melt turbulence). Surface roughness initially decreased with increase in ultrasonic vibration amplitude (5.2 μm in without ultrasonic vibration samples to 1.82 μm in 20% ultrasonic vibration samples) and then subsequently increased in the higher ultrasonic vibrations amplitude samples (Ra = 3.6 μm in 50% ultrasonic vibration samples). This trend was also observed in the crack widths of the clad coatings that is associated with surface roughness (increase in roughness results in increase in uneven surface stresses hence more cracking) that initially decreased with application of ultrasonic vibration (10 μm in 20% samples compared to 20 μm in without ultrasonic samples) and eventually increased (25 μm). Their hot corrosion behavior was investigated in 1100 C fused Na_2SO_4+V_2O_5 salt (1:1 ratio by wt%) after immersing them for 20 hours. The crack distribution and roughness was observed to significantly influence their hot corrosion behavior as both acted as resting zones for the hot molten salts. The extended contact time results in depletion of yttria from the matrix (to form YVO_4), destabilizing the t-ZrO_2 (zirconia) and triggering undesirable transformation of t-ZrO_2 to m-ZrO_2. Hence the strain and oxidation tolerance of the claddings were lower in 50% ultrasonic vibration samples, while the comparatively more optimized processing conditions experienced by the 20% ultrasonic vibration samples resulted in improved strain and oxidation tolerance.

1.3.4 Ultrasonic Vibration-Assisted Additive Manufacturing

Additive manufacturing is one of the most promising manufacturing technologies and has its popularity has grown immensely in the last decade due to their ability to manufacturing complex components, superior control of composition, and lower manufacturing time. In this novel technique,

lasers have been proven to be extremely valuable due to their high power density and excellent process control, resulting in development of additive manufacturing techniques such as selective laser sintering, direct metal laser sintering, laser net engineered shaping, and selective laser melting. All the aforementioned processes essentially involves the deposition of a layer of the desired material in powders, and employing a high power laser beam to consolidate the powders (by sintering or melting), and subsequently iterating the process repeatedly. It should be noted that the use of lasers in this technique is not only just to consolidate the process, but also to exploit the high thermal stresses generated during the processing due to built up heat from the preceding laser scans to generate plastic working of the powders [33, 34]. Also, unlike laser melting, this process involves extensive melting and consolidation of powders, and therefore, very unique microstructures have been reported in additive manufacturing processes that are not usually observed in components manufactured using conventional techniques. However, the components manufactured by additive manufacturing (using lasers) also exhibits the usual challenges associated with laser processing such as pores, micro cracks, and textured dendritic microstructure. Hence, the acoustic streaming, cavitation, and hydrodynamic stresses associated with ultrasonic vibrations can be naturally extended to additive manufacturing techniques as well.

The effect of ultrasonic vibrations on property and quality of additive manufactured components was explored by Ning *et al* [35]. The researchers fabricated 17-4 PH Fe-Cr stainless steel using a laser engineered net shaping machine. The size of the fabricated components was observed to increase with application of ultrasonic vibrations (the without ultrasonic vibration-assisted fabricated samples exhibiting a height and cross-sectional area of 2.56 mm and 3.22 mm^2 respectively while the with ultrasonic vibration fabricated samples exhibited a height and cross-sectional area of 2.64 mm and 3.59 mm^2 respectively). This improvement is sample size was attributed to the improved powder utilization efficiency in the ultrasonic vibrations assisted manufactured components. The porosity of the components were also observed to decrease with ultrasonic vibration-assisted samples (from 0.68%

in without ultrasonic vibration samples to 0.35% in with ultrasonic vibration samples), due to improved collapse rate of the gas induced pores from the cavitation stresses generated by ultrasonic vibrations. The grain size also was further refined by the ultrasonic vibrations (from 7-11 μm in the without ultrasonic to 1.5-3 μm in the with ultrasonic samples), that resulted in improvement in hardness (from 441 HV in without ultrasonic samples to 456.8 HV in with ultrasonic samples).

The effect of the ultrasonic vibrations on the processing and mechanical properties was further continued by Cong *et al* [36]. The authors fabricated 17-4 stainless steel blocks using laser engineered net shaping with and without the simultaneous applications of ultrasonic vibrations (frequency = 41 kHz) . It was observed that the ultrasonic vibrations improved the powder utilization efficiency (ratio of volume of component to actual volume of powders used, that increased from 20.7% in the without ultrasonic assisted fabricated samples to 23.2% in with ultrasonic vibration-assisted samples). The increase was attributed to the higher available energy for the powders from the ultrasonic vibrations resulting in increased melting. The higher powder utilization efficiency also increased sample height (and size) from 1.26 mm in without ultrasonic vibration-assisted samples to 1.35 mm in with ultrasonic vibration-assisted samples. The cavitation stresses also significantly reduced the defects such as pores and micro cracks due to earlier collapse of gas-evolved pores, as well as triggered extensive dendrite fragmentation resulting in a more refined equiaxed microstructure (from 10 μm columnar grains in without ultrasonic vibration samples to 2 μm in with ultrasonic vibration samples). The aforementioned improvements in fabrication quality and microstructure due to ultrasonic vibrations resulted in improvement in hardness (from 46 to 56 HRC), tensile strength (by 144.2%), ductility (by 108.5%), toughness (by 313.9%), and yield strength (117.7%).

CHAPTER II

OBJECTIVES AND PROPOSED WORK

Laser surface engineering has emerged as a highly promising non-conventional processing technique to achieve tailor made surface properties. The outstanding properties are primarily due to the formation of highly refined microstructure, elemental redistribution and high power density associated with lasers that promote possibility of surface alloying. In addition, lasers have recently been reported to be successfully used to process surface with very controlled textures. However, despite of these outstanding properties, laser processed surfaces have been reported to suffer from dendritic microstructure, crystallographic texturing, and elemental redistribution. Also, investigations on processing techniques such as laser surface texturing has been mostly limited to pulsed lasers with very short pulse regimes such as femto or pico-second lasers.

In conventional solidification techniques, the efficiency of ultrasonic vibrations in development of refined equiaxed microstructure has been established. However, similar investigations on effect of simultaneous application of ultrasonic vibrations in processing techniques involving rapid solidification techniques have not extensively reported. Hence, this investigation primarily focused on investigation of ultrasonic vibration-assisted laser surface engineering. Significant efforts were directed towards evaluating the efficiency of simultaneous application of vertical ultrasonic vibrations during laser processing. Investigations were undertaken on several fundamental aspects during research of this dissertation such as: (1) ultrasonic vibration-assisted laser surface melting and cladding of aluminum alloy and composites laser surface melting of wrought Al-Cu-Mg alloy and its influence in microstructural evolution, crystallographic texture formation, elemental redistribution and its relationship with surface properties such as corrosion

resistance and surface mechanical strength, (2) ultrasonic vibration-assisted laser surface melting and texturing of ti-6al-4v alloy and its influence in microstructural evolution, surface mechanical properties, and tribological behavior in simulated body fluids, (3) ultrasonic vibration-assisted laser surface texturing of stainless steel and its influence on the tribological properties with addition of graphene as a lubricant.

2.1 Ultrasonic Vibration-Assisted Laser Surface Melting and Cladding of Aluminum Alloy and Composites

This investigation explored laser surface melting of a wrought Al-Cu-Mg aluminum alloy by irradiating the substrate with a high power continuous wave CO_2 laser while the substrate was simultaneously subjected to vertical ultrasonic vibrations. The increased convectional currents (of the air enveloping the melt pool) associated with ultrasonic vibrations was observed to result in slight increase in solidification rate, that was confirmed by thermal modeling. The laser surface melted samples in which ultrasonic vibrations were simultaneously applied exhibited marked grain refinement with nearly five-fold decrease in grain size compared to the laser melted samples processed without application of ultrasonic vibrations. This was attributed to the dendrite fragmentation triggered from cavitation associated with ultrasonic vibrations. Also, it appears that the ultrasonic vibrations resulted in the resolidified grains to exhibit primarily dendritic parabolic morphology compared to the cellular morphologies observed in the laser surface melted samples without ultrasonic vibrations. The microstructural texture and phase evolution strongly indicated that the ultrasonic vibrations resulted in formation of considerably randomly oriented α-Al grains compared to the highly textured grains observed in the laser melted samples without ultrasonic vibrations, also reflected in the microstructures. Furthermore, the application of ultrasonic vibrations virtually eliminated the θ phase reducing the surface hardness.

The investigation was further continued to study the effect of laser melting with and without simultaneous application of ultrasonic vibrations on electrochemical properties of 2024

aluminum alloy. The electrochemical behavior of the laser melted specimens was studied using open-circuit and potentiodynamic (Tafel) polarization measurements. Subsequently, investigation of the corrosion films was performed with scanning electron microscopy. It was observed that the laser melted specimens exhibited significant improvement in open circuit potential (both with and without simultaneous ultrasonic vibration application). The open circuit potential of the laser melted specimen without ultrasonic vibrations was observed to be more stable compared to the laser melted specimen with ultrasonic vibrations. It was observed that the corrosion mechanism undergoes a transition from pitting to uniform corrosion in the laser treated specimen, particularly in the laser melted specimen without ultrasonic vibrations. However, the extensive agitations due to ultrasonic vibrations in the melt pool appear to restrict copper migration to grain boundaries that result in porous and relatively inefficient passive layer formation in laser processed samples with application of ultrasonic vibrations. This behavior was also observed in the potentiodynamic polarization studies that showed that the laser melted specimen without ultrasonic vibrations exhibited lower corrosion current and corrosion rate compared to the laser melted specimen with ultrasonic vibrations as well as the as received substrate.

Due to the observed decrease in surface mechanical hardness that indicated similar decrease in tribological properties of laser melted wrought aluminium alloys, the study was continued to investigate laser composite surfacing of wrought aluminum alloy with ceramic particles has been extensively investigated for improving tribological properties. However, the process often results in incomplete penetration of ceramic particles in the melt pool and undesirable interfacial reactions. In this paper, laser composite surfacing of 2024 aluminum alloy with SiC particles is investigated using two distinct approaches: laser remelting and laser melting under the influence of ultrasonic vibrations of preplaced powder mixture. Detailed analysis of variation of clad layer thickness, microstructure in the composite clad layer, phase/texture development, surface roughness, and sliding wear performance with laser processing conditions is presented. The

analysis showed that remelting and ultrasonic vibration assist results in significant improvement in clad layer thickness and microstructure (reduction in needle-like α-Si phase). While the laser remelting resulted in significant reduction in wear rate, the specimens processed with ultrasonic vibration-assisted laser melting showed variable wear rate likely due to complex effects of microstructural modification and enhanced surface roughness.

2.2 Ultrasonic Vibration-Assisted Laser Surface Melting and Texturing of Ti-6Al-4V Alloy

Titanium alloys are becoming increasingly important in several manufacturing sectors due to their high strength-to-weight ratio and excellent corrosion resistance. However, surface modification of the titanium alloys are often required to improve surface hardness and wear resistance. In this investigation, spot laser surface melting of Ti–6Al–4V alloy under the influence of ultrasonic vibrations (20 kHz) was investigated. The development of microstructure and microhardness in the resolidified region with and without the application of simultaneous ultrasonic vibrations was studied. It was observed that the application of ultrasonic vibrations entirely eliminated the large columnar grains from the resolidified region and refined the microstructure, resulting in about two-fold increase in the surface microhardness. The microstructural refinement with the application of ultrasonic vibrations during laser was primarily due to enhanced fluid flow and cavitation in the melt.

The studies were further continued by processing larger area substrates to evaluate its influence in tribological properties. In this study, ultrasonic vibration-assisted laser surface processing that involved application of vertical ultrasonic vibrations to the Ti-6Al-4V alloy substrates while being irradiated with a CO_2 laser was performed for the development of laser melted and textured surfaces with potential applications in biomedical implants. The laser processing resulted in very consistent repeating undulating grooved surfaces, and the undulations were significantly more pronounced in the samples processed with higher ultrasonic power outputs. The phase evolution, studied using x-ray diffraction, confirmed that the laser processing triggered

transformation of globular α → acicular α and martensitic α' as well as increased amounts of retained β phases, which were also reflected in the microscopic analysis. The surface texture developed by the laser processing resulted in increased surface wettability with increasing ultrasonic power output. The textured surfaces exhibited marked decrease in coefficients of friction during sliding wear testing performed under simulated body fluid due to lubricant entrainment within the textured grooves. The texturing also resulted in significant reduction in surface contact area during the wear process, which considerably reduced the overall wear rates due to abrasive wear.

2.3 Ultrasonic Vibration-Assisted Laser Surface Texturing of Stainless Steel

The studies also were directed towards understanding the efficiency of ultrasonic vibrations in improving tribological performance of laser surface textured steels with continuous wave lasers. It should be noted that laser surface texturing has been almost exclusively performed using lasers with extremely short pulse times (in the range of 10^{-9} to 10^{-15} s). But industrial applications of lasers are mostly dominated by continuous wave lasers (that are capable to produce shortest pulses in the range of 10^{-3} s). Hence in this study, substrates were processed with a novel processing technique involving laser texturing while the surface was simultaneously subjected to vertical ultrasonic vibrations. The investigation was primarily directed towards effect of graphene addition in the tribological properties of sliding steel surfaces that has attracted significant interest in the past few decades due to its unique mechanical and electrochemical properties. In particular, graphene reduces friction and wear loss in structural materials. The increase in vibration amplitude increased the surface roughness that was observed to further decrease coefficient of friction. It was established that just trace addition of graphene monolayer flakes (average thickness of 0.35 nm) resulted in significant decrease in the coefficient of friction. The Raman spectroscopy analysis of the wear scars revealed the presence of graphene validating even trace addition of graphene results

in formation of a highly lubricated tribolayer. Raman spectra also indicate defect formation in the graphene during wear due to the severe shear stresses.

CHAPTER III

EXPERIMENTAL DETAILS

3.1 Materials

The aluminum substrates used for the laser surface engineering experiments was commercial high strength wrought Al-Cu-Mg alloys (source: McMaster-Carr). The laser surface melting experiments were performed using wrought Al-Cu-Mg alloys. The laser surface cladding experiments were performed on 2024 aluminum alloy (3.8-4.9% Cu, 1.2-1.8% Mg, rest Al and trace elements) hexagonal cap screws (head width = ¾"). The aluminum alloy specimens were carefully polished using 1200 grit size paper, sand blasted (pressure of 70 MPa), and subsequently cleaned with to remove surface impurities. Commercially pure Al (particle size: 10-14 μm) and SiC (particle size: 10.6 μm) powder mixture in the 80:20 ratio by weight was ball milled for 15 min at 300 rpm. Subsequently, a slurry of the powder mixture was prepared using water soluble organic binder (LISI W 15853) and reducer (LISI W 15833) and was sprayed on the surface of the AA2024 substrate. The titanium substrates used was Ti-6Al-4V screws, for spot melting investigation grade 5 Ti-6Al-4V screws were used (source: McMaster-Carr). For large area processing, grade 23 Ti-6Al-4V (Ti-6Al-4V ELI) substrate (source: M. Vincent and Associates, Minneapolis, MN) was used. The substrate (for grade 23 Ti-6Al-4V) was procured as rod, that was subsequently machined to flat head screws (φ = 1.5"), and then polished with 1200 grit size polishing paper to remove surface irregularities. Each substrate post polishing was carefully cleaned with deionized water and acetone to remove inorganic and organic impurities respectively.

3.2 Ultrasonic Vibration-Assisted Laser Processing Setup

Figure 3.1 presents the ultrasonic vibration-assisted laser surface processing set-up used in this study. The substrates were irradiated with a continuous wave (CW) CO_2 laser (Ferranti, Manchester, UK) operated at a power ranging from 450-950 W. The laser beam had a Gaussian energy distribution. The ultrasonic vibrations was applied by mounting the sample with an ultrasonic vibration probe (made of titanium-alloy with 1" diameter) that was connected with an ultrasonic power generator (Sonic & Materials Inc., Newtown, CT, USA) operating with a frequency of 20 kHz and total power output of 750 W. The key processing parameters such as irradiation power, scanning speed, focusing distance, beam diameter, ultrasonic power amplitude was systematically varied in each investigation and is provided separately.

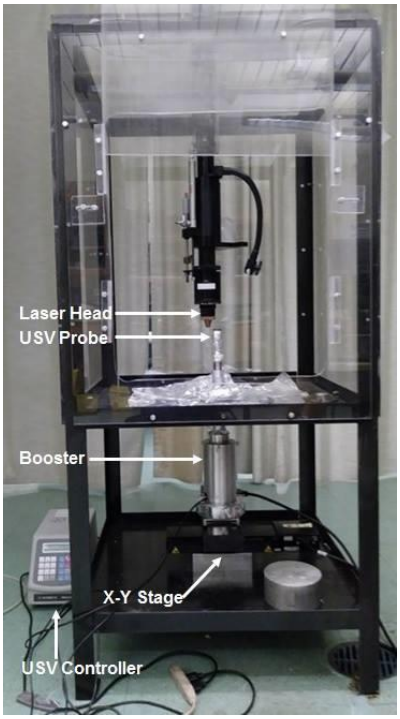

Figure 3.1 Experimental set-up used to perform laser surface engineering with and without simultaneous applications ultrasonic vibrations

3.3 X-Ray Diffraction (XRD)

XRD analysis of the bulk substrates was conducted using a Philips Norelco X-Ray diffractometer (PW1830, Philips, Longmont, CO, USA) operating with Cu K_α (λ = 1.54 Å) radiation. The micro-XRD characterization was performed using a Bruker AXS D8 X-Ray diffractometer (Brucker, Billerica, MA, USA).

3.4 Scanning Electron Microscopy (SEM) And Energy Dispersive Spectroscopy (EDS)

The microstructural characterization was performed using a scanning electron microscope (FEI Quanta 600, Thermofischer Scientific, Hillsboro, OR, USA) that was enabled with an Evex EDS system for elemental analysis. The microstructures were imaged after carefully polishing (with progressively finer emery paper, followed by colloidal alumina) and subsequently etching the substrate. Keller's reagent (composition: HNO_3, HCl, HF and water with a ratio of 2.5:1.5:1:95 by volume) and Kroll's reagent (composition: HNO_3, HF and water with a ratio of 2:10:88 by volume). The wear scars were imaged using a JSM-6360 (JEOL, Japan) scanning electron microscope.

3.5 Microhardness

The microhardness of the samples were measured using a Vickers microhardness tester (Model: CM-700 AT, Clark Instruments, Suntec Corp, Novi, MI, USA). The load and dwelling time was varied from 200 to 500 gf and 15s to 25 s respectively in each specific investigation. The measurements were repeated for five times for each reading and the average value (with the corresponding standard deviation is reported).

3.6 Wear and Profilometry

The wear tests were conducted using a tribometer (Nanovea, Irwin, CA) operating in ball-on-disk mode. The operating environment (e.g. dry, lubricated, immersed), load, disk rotating speed, wear radius, counterbody, and testing time was varied for each experiment and has been

presented separately. The surface profilometry experiments were conducted using a non-contact 3D optical profilometer (Model: PS50, Nanovea, Irvine, CA, USA). The simulated body fluid used in the immersed wear experiments was Hank's solution (Life Technologies, Carlsbad, CA, USA). The lubricated wear experiments were performed by adding a suspension of graphene and ethanol (concentration 1mg/L, Graphene Laboratories Inc., Calverton, NY, USA).

3.7 Corrosion Testing

The open circuit and potentiodynamic polarization measurements were performed in naturally aerated 3.5% NaCl solution using a potentiostat galvanostat (Ametek Scientific Instruments). The potentiostatic experiments were performed for 20,000 s and the corrosion films were subsequently characterized using a scanning electron microscope (FEI Quanta, Thermofischer Scientific, Hillsboro, OR, USA). The potentiodynamic experiments were performed by scanning the current response from -0.25 V to +0.25 V with respect to the open circuit potential at a sweep rate of 0.33 mV/s. The corrosion rate was calculated using Faraday's law:

$$Corrosion\ Rate = \frac{i_{corr}M}{nF\rho} \quad (3.1)$$

Here, i_{corr} is the corrosion current density measured by Tafel extrapolation in A/cm^2; M is the atomic weight of Al in g; n is 2 for Al; F is Faraday's constant (96,500 C/mol).

3.8 Surface Wettability

The surface wettability was measured by imaging a droplet of water (volume = 5 μL) on the substrates and imaging the droplet with an optical microscope (Proscope Camera, Bodelin Technologies, Wilsonville, OR, USA), and the contact angles of the droplets with the substrate were subsequently calculated with by image analysis using ImageJ software.

3.9 Raman Characterization

Raman spectra were acquired by a WITec alpha300 micro-Raman system, equipped with 532 nm excitation laser and 600 lines/mm grating. The signal was accumulated for 50 s employing a 20× objective lens, incident laser power of 10 mW, and laser spot of 10 µm diameter.

3.10 Laser Thermal Modelling

A 3D heat transfer model was developed using the COMSOL ® Multiphysics software (Ver. 5.1). The model was created to simulate laser surface melting of the aluminum alloy specimens and to predict the temperature profile of the specimens. Isothermal lines in the cross section of the laser melted samples were used to predict the melting depth and width. A Gaussian distribution of the laser energy, convection and radiation surface heat losses and conduction heat transfer through the specimen were considered on the computational heat transfer model. The model considered the specimen as a cylinder with a height of 8 mm and diameter of 11 mm, presented in Figure 3.2 and a step time of 0.01 s was used.

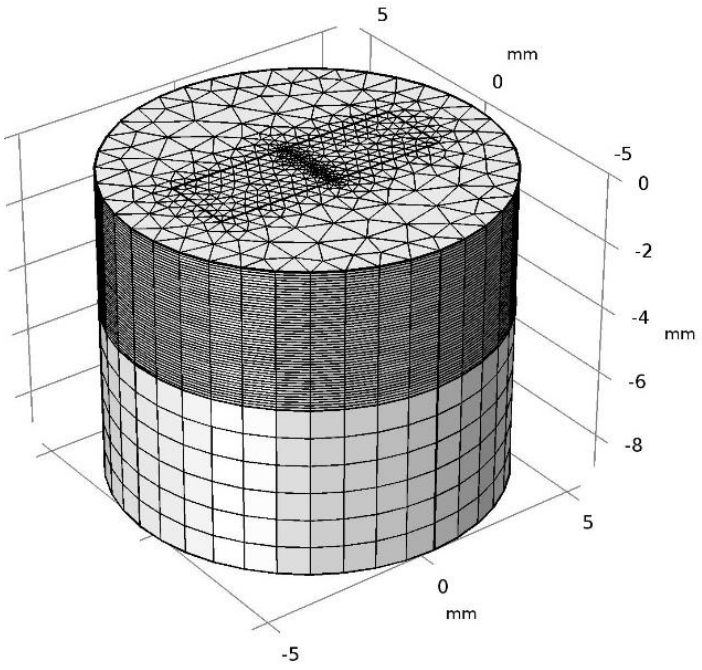

Figure 3.2 Schematic description of specimen used for thermal model

The thermophysical properties used in the model are listed in Table 3.1.

Table 3.1. Thermophysical properties employed in the model

Thermophysical Property	**Value**	
Absorption Coefficient, A	0.97	
Power, P (W)	973	
Emissivity, ε	0.4	
Stefan-Boltzmann constant, σ (W/m^2K^4)	5.67×10^{-8}	
Beam Diameter, D (mm)	2.15	
Density, ρ (Kg/m^3)	2780	
	Temp Range (K)	**C_P**
Heat Capacity, C_P (J/kgK) [37]	250-298	881
	298-373	927
	373-473	1047
	473-573	1080
	573-673	1080
	673-2000	1080
	Temp Range (K)	k
Thermal Conductivity, k (W/mK) [37]	250-298	100
	298-373	140
	373-473	160
	473-573	155
	573-673	145
	673-773	145
	773-873	180
	873-2000	238
Heat Transfer Coefficient, h (W/m^2K) [38]	50	

The model assumed that top surface of the specimen (irradiated by a laser beam) that exclusively acts as the source of heat generation. The governing heating equation (for the top surface) of the specimen is presented in Eq. 3.2. The heat loss phenomenon was attributed to convection and radiation losses that resulted in cooling of the heated surface, which was simulated using the cooling equation (Eq. 3.3). The laser beam did not irradiate the side surface of the specimen, thus only convection and surface-to-ambient radiation heat losses are applied (Eq. 3.4). The bottom surface of the specimen was assumed as an insulator and the insulator surface equation was applied to the boundary (Eq. 3.4). To include the effect of ultrasonic vibration on the heat transfer, the value of h was increased 25 times [39] while the ultrasonic vibration is present. The temperature distribution was simulated using the heat transfer equation described in eq. 3.5.

$$-k\left[\left(\frac{\partial T}{\partial x}\right)+\left(\frac{\partial T}{\partial y}\right)\right]=A\frac{4P}{\pi D^2}-\varepsilon\sigma\left[T^4-{T_0}^4\right]-h[T-T_0] \quad 3.2$$

$$\left[\left(\frac{\partial T}{\partial x}\right)+\left(\frac{\partial T}{\partial y}\right)\right]=\varepsilon\sigma\left[T^4-{T_0}^4\right]+h[T-T_0] \quad 3.3$$

$$k\left[\left(\frac{\partial T}{\partial x}\right)+\left(\frac{\partial T}{\partial y}\right)\right]=0 \quad 3.4$$

$$\rho C_P\frac{\partial T}{\partial t}+\ \rho C_P u.\nabla T+\ \nabla.q=Q \quad 3.5$$

CHAPTER IV

RESULTS AND DISCUSSION

4.1 Ultrasonic Vibration-Assisted Laser Surface Melting of 2024 Aluminum Alloy

This investigation primarily focused on the microstructural evolution of wrought Al-Cu-Mg alloy during laser surface melting in line scanning mode with and without simultaneous application of vertical ultrasonic vibrations on the substrate. Commercial aluminum 2024 alloys samples procured in the form of threaded hex-head screws were used for laser processing (sample ID: 93306S712, McMaster-Carr, USA). The material was selected to be aluminum as aluminum does not undergo solid to solid phase transformations (unlike titanium and steel) and cooling of liquid aluminum exclusively results in $L \rightarrow \alpha$ transformation. Therefore, the resolidified structure (post completion of solid to liquid transformation) can be preserved. Furthermore, line scanning mode was selected to investigate microstructural evolution of resolidified grains that has undergone the solidification transformation once and not been subjected to remelting and resolidification, especially in the overlapped regions of large area processed multi-line scanned substrates. The major motivation of this investigation was to study the efficiency of the hydrodynamic stresses associated with ultrasonic vibrations in triggering grain refinement and subsequently generating a refined equiaxed microstructure during rapid solidification (associated with laser surface melting). The key processing conditions for the corresponding sample (identified with the sample ID) has been presented in Table 4.1.

Table 4.1 Summary of processing conditions employed for performing laser surface melting experiments without and with simultaneous influence of ultrasonic vibrations

Sample ID	Laser Power (W)	Beam Diameter (mm)	Track Length (mm)	Beam Velocity (mm/min)	USV Amp (%)
LSM	950	2.15	6	100	0
UV-LSM	950	2.15	6	100	20

4.1.1 Melt Depth Characterization

Figure 4.1 presents the low magnification cross-sectional scanning electron micrographs of the laser surface melted samples without (LSM) and with the influence of ultrasonic vibrations (UV-LSM). As can be observed from Figure 4.1(a), the LSM samples exhibited a very well defined melt pool with a depth of about 478 μm and width of 1132 μm. The melt depth of the UV-LSM samples, as can be observed from Figure 4.1(b), was calculated to exhibit a depth of 348 μm and width of 1021 μm. Thus, the melt depth appeared to decrease in the laser surface melted samples under the influence of ultrasonic vibrations compared to the without ultrasonic vibration counterparts. The effect of ultrasonic vibrations in increasing the air velocity at the substrate-air interface and subsequently the convectional cooling rate has been widely reported in literature [39]. Therefore, the decrease in melt depth appears to be a direct consequence of the higher convectional cooling rates associated with substrates vibrating at ultrasonic frequencies. The quantification of the effect of convectional cooling was performed using thermal modelling techniques employing finite element method.

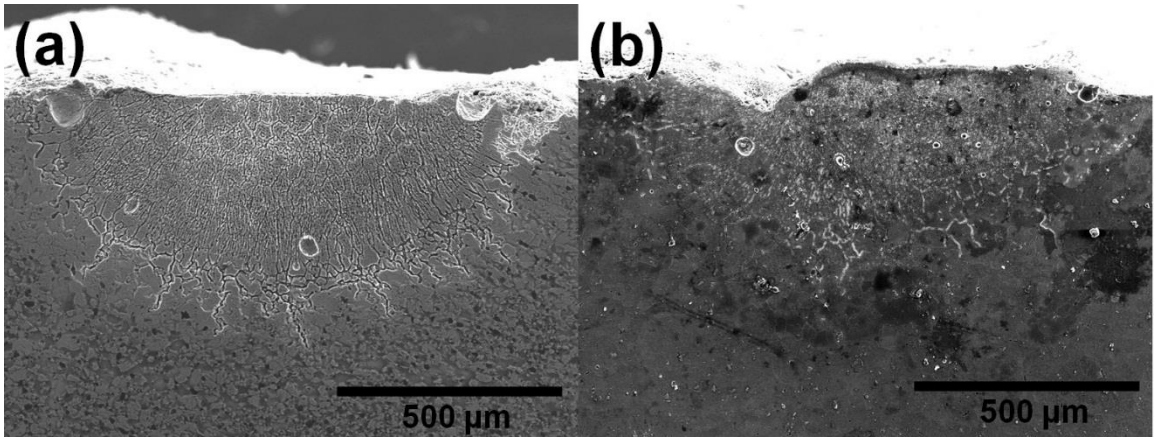

Figure 4.1 Low magnification cross-sectional microstructures of resolidified regions in laser track for: (a) LSM and (b) UV-LSM

4.1.2 Computational Analysis of Cooling Rate

The variation of the cooling rate during of the LSM sample has been presented in Figure 4.2(a). The thermal modelling indicated that the maximum cooling rate at the surface of the melt pool without the influence of ultrasonic vibrations increased from 493 K/s at the core (about 400 µm from the surface) to 1120 K/s at the surface. The variation can be clearly attributed to the higher heat convection at the substrate-material interface (surface) compared to the core of the material. The similar modeling was performed employing conditions associated with ultrasonic vibrations (corresponding to UV-LSM sample), and the results have been presented in Figure 4.2(b). This was to understand the effect of enhanced convection rate on the cooling rate and melt front velocity during the laser melting process. It can be observed that the maximum cooling rate at the surface increased from about 1120 K/s to 1200 K/s when the thermal convection rate was increased. It should be noted that the microstructural evolution during laser melting has been primarily associated with the melt front velocity. The melt front velocity, based on the thermal profile obtained from the thermal modeling, was calculated for the LSM and UV-LSM samples and has been presented in Figure 4.2(c). It can be clearly observed that the melt front velocity indicated

marginal increase from about 1863 μm/s to 1907 μm/s at the surface of the melt pool due to the enhanced convection. Considering the microstructural analysis (discussed later) exhibiting significant (more than five-fold) decrease in grain size in the UV-LSM sample, it can be clearly concluded that melt front velocity is not the major contributor of grain refinement. Hence, the other popular mechanisms associated with ultrasonic vibrations such as dendrite fragmentation [40], increased heterogeneous nucleation due to fragmentation of secondary phases [20], remelting of nascent dendrite tips [41] appear to dominate the microstructural refinement observed in the UV-LSM sample.

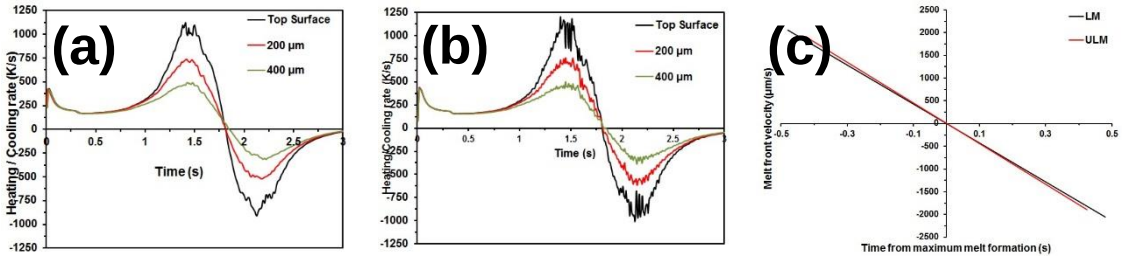

Figure 4.2 Variation of cooling rate with depth in (a) LSM and (b) UV-LSM samples, (c) variation of melt front velocity with time in LSM and UV-LSM samples

4.1.3 Microstructural Analysis

The moderate magnification microstructure LSM and UV-LSM samples have been presented in Figure 4.3. It was observed that the processing primarily resulted in a directionally solidified microstructure exhibiting epitaxial growth from the fusion boundary to the surface, as presented in Figure 4.3(a). The directionally solidified grains were observed to exhibit cellular morphology as can be observed in Figure 4.3(b-c). The occurrence of directional solidification or constrained growth often observed in processing routes wherein direction of solidification and direction of heat flow is antiparallel as reported by Zimmerman *et al.* [42]. The primary reason for absence of secondary, tertiary and higher order dendrites has been attributed to the positive temperature gradient imposed by the heat flow from the surface to the core, which dissipates the latent heat of fusion through the solid resulting in constrained growth.

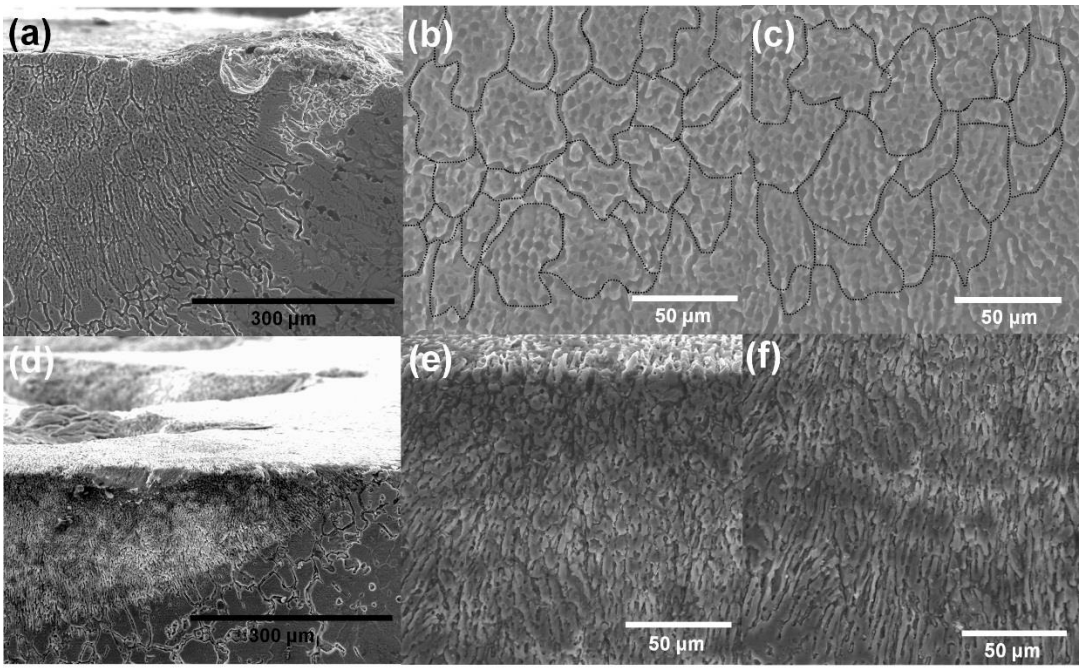

Figure 4.3 Cross-sectional microstructures of (a-c) LSM, and (d-f) UV-LSM

It was also observed that the aspect ratio appeared to be highest at the fusion boundary (about 4.5), gradually decreasing in the grains closer to the surface (about 2.13 at the surface). Now, since melt front velocity is highest at the fusion boundary (1863 µm/s, described in the computation model), the nascent dendrites naturally experience higher undercooling at the fusion boundary resulting in generation of higher number of stable nuclei at the surface. Thus, the increase in competing stable nucleii significantly reduces the average lateral space for a nucleus to grow and thus results in further preferential growth towards the surface, as well as increasing the aspect ratio. However, the grains closer to the surface experience less undercooling and therefore more freedom for lateral growth. Therefore, the increase in undercooling with increase in melt depth appears to be the primary reason for the increase in aspect ratio with melt depth. The microstructures of the LSM sample also exhibited presence of coarse intermetallic precipitates. The precipitates are most likely the θ (Al_2Cu) precipitates based on their spherical morphology and coarse size with an average diameter about 7 µm (the θ″ and θ′ precipitates are reported to exhibit plate-like morphology and significantly finer) [43, 44]. The moderate magnification microstructure of the

UV-LSM sample has been presented in Figure 4.3(d). The microstructure consisted of predominantly fine dendritic grains in the resolidified region near the fusion boundary. It can be clearly observed that the UV-LSM sample comprised of significantly refined grains. The grain size of the LSM sample was about 28 μm at the surface and 19 μm at the fusion boundary, compared to the UV-LSM sample that exhibited an average grain size of about 4.8 μm and 2.8 μm at the surface and fusion boundary respectively. These grains appeared to grow towards the center of the melt pool as observed during typical directional solidification, as presented in Figure 4.3(e-f). It was also observed that unlike the LSM sample that indicated presence of coarse θ precipitates, the θ precipitates was virtually absent in the UV-LSM sample. This can be attributed to the increased of supersaturated solid solutions and suppression of precipitation due to dissolution of secondary phases or increased homogenization in ultrasonic vibration-assisted soldering of 2024 aluminum alloy has been reported by Yuan-Xing *et al.* [45]. The primary reason mentioned by the authors was the increase in diffusion due to the ultrasonic vibrations during the resolidification process. As mentioned previously, it appears that the cavitation associated with ultrasonic vibrations triggers extensive dendrite fragmentation of both α-Al grains and the secondary phases. Thus, it appears that the ultrasonic vibrations facilitated extensive fragmentation and resulted in considerable increase in nascent nuclei for grain growth. It was also observed that unlike the LSM sample, that exhibited reduction in aspect ratio (higher lateral growth) near the surface, the aspect ratio of the dendrites remained relatively unchanged with change in melt depth.

Now, the effect of convectional cooling is most effective at the air-melt pool interface that is the surface of the melt pool. Subsequently, the effects of enhanced convectional cooling are more effective at regions closer to the surface, as was also observed in the thermal modeling (1120 K/s at the surface compared to 493 K/s at the fusion interface). This is in good agreement with the variation of aspect ratio in the UV-LSM sample that experienced faster cooling rates, especially at the surface, significantly increasing the nucleation rate at the surface and therefore the aspect ratio

closer to the surface remains relatively unchanged. The topographic microstructures of the LSM sample has been presented in Figure 4.4. As can be observed from the low magnification microstructure presented in Figure 4.4(a), a very well defined laser track was generated during the laser surface melting of the sample. The width of the laser track was observed to consistently increase with increase in progress of laser track (about 1071 μm at region I and 1522 μm at region II).The increase in laser track is due increase in preheating ahead of melt pool with time. The increased preheating essentially increases the temperature of the neighboring regions of the melt pool and therefore the total energy (and time) required for melting the preheated regions also decreases resulting in a higher volume of melting occurs for the same amount of input heat. The morphology and grain size of the interfacial (region A) and core regions (region B) in higher magnification has been presented in Figure 4.4(b) and 4.4(c) respectively. It can be clearly observed in Figure 4.4(b) that the grain exhibited consistent epitaxial growth from the interface, with an average grain size of about 7.1 ± 0.7 μm. The grains were observed to solidify with an orientation angle of approximately 65 ± 3° to the laser scanning direction at the surface, and gradually the orientation angle was parallel (0°) with the laser scanning direction, as can be observed from Figure 4.4(c). Similar changes in orientation angle of grains have been reported rapid solidification studies on various Al-Cu alloys with varying copper composition by Gill *et al.*[46, 47]. It should be noted that the orientation angle between grain orientation and laser scanning directions in the mentioned publications was calculated on longitudinal sections. However, since the plane front is three-dimensional, similar relationship between orientation angle and laser scanning direction should exist at the surface grains as well.

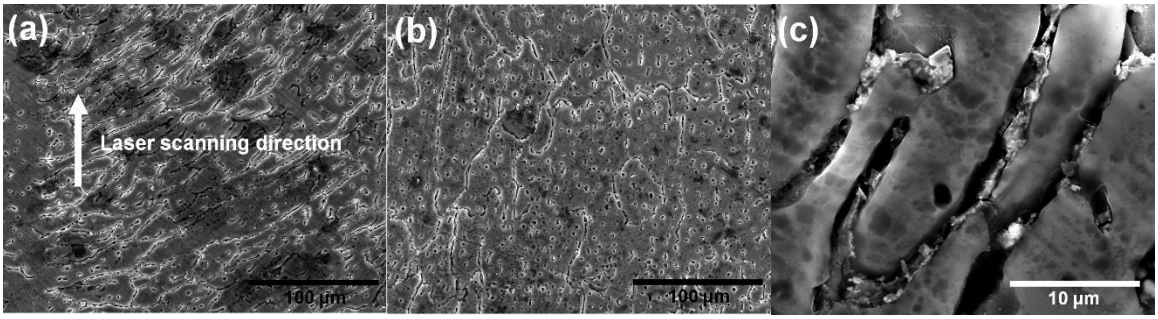

Figure 4.4. Surface microstructures: (a) at the fusion boundary, (b) interior of remelted region, and (c) high magnification microstructure exhibiting the cellular elliptical morphology for LSM sample.

The cellular morphology was numerically predicted by Hunt *et al.* [48, 49] and the solution was noted to be similar to the solutions on the Hele Shaw cells reported by McLean *et al.*[50]. Thus since the elliptical morphology of the grain tips, as can be observed in Figure 4.4(d), appeared to emulate the circular/elliptical tips for epitaxial cellular grains predicted by the authors, it can be clearly stated that the grains were epitaxial cells. It should be also noted that the microstructure comprising of parallel cellular lamellae of grains are remarkably similar to the microstructures of laser remelted Al-Cu eutectic alloys with laser scanning velocities below 20 cm/s, reported by Zimmerman *et al.* [42]. Similar cellular morphology of grains has been reported on the morphological maps of rapidly solidified Al-Cu alloys developed by Gill *et al.* [46, 47].

Therefore, the dominant solidification mechanisms of the LSM should be the stable lamellar dendritic growth reported by the aforementioned investigations. The grains indicated preferential precipitation of equilibrium coarse θ (Al_2Cu) precipitates along the grain boundaries, as can be observed from Figure 4.4(d). The presence of such precipitates in laser melted Al-4.5 Cu alloy has also been reported by Munitz *et al.*[51]. The reason has been primarily attributed to the preferential segregation of copper along the grain boundaries. Therefore, the preferential segregation of copper at the grain boundaries during the laser assisted remelting process in conjunction with the tendency of the equilibrium θ precipitates to solidify at the grain boundaries

are primarily responsible for the lamellar θ phase along the grain boundaries. The topographic microstructures of the UV-LSM sample have been presented in Figure 4.5. The low magnification microstructure, as can be observed from Figure 4.5(a) exhibits considerably uniform melt track unlike the LSM sample, observed in Figure 4.4(a), resulting in much less change in melt depth (about 1138 μm at region I and 1123 μm in region II). The high magnification microstructures, presented in Figure 4.4(b-d) reiterate the significantly refined grains observed in cross-sectional microstructures (presented in Figure 4.3). It was also observed that unlike the LSM microstructures that exhibited continuous grain growth of cellular morphologies from the resolidified interface, the UV-LSM microstructures exhibit grain branching, as can be observed in Figure 4.5(b). Again, evolution of grains of similar morphologies has been predicted numerically and identified as dendritic by Hunt *et al.* [48, 49]. The authors reported that one of the most characteristic feature of a dendritic grain was the parabolic appearance of the grain's tip, described as 'Ivantsov dendritic appearance'. The authors reported that unlike a cellular grain, that exhibits primarily circular/elliptical interface, the dendritic grains are reported to exhibit primarily parabolic morphology. Clearly, the sharp grains, as can be observed in Figure 4.5(d) appear to imitate the parabolic features, confirming them to be dendrites. Thus, the resolidified grain morphology appears to shift from cellular to dendritic when solidification occurs under the influence of ultrasonic vibrations. The formation of dendritic grains also explains the dendrite branching observed in Figure 4.5(b). The primary cause for unstable dendrite growth is most likely due overgrowth of certain dendrites, resulting in the neighboring dendrites (with slower growth rates and thus smaller sizes) to trigger secondary/tertiary dendrite formation to compensate the extra space.

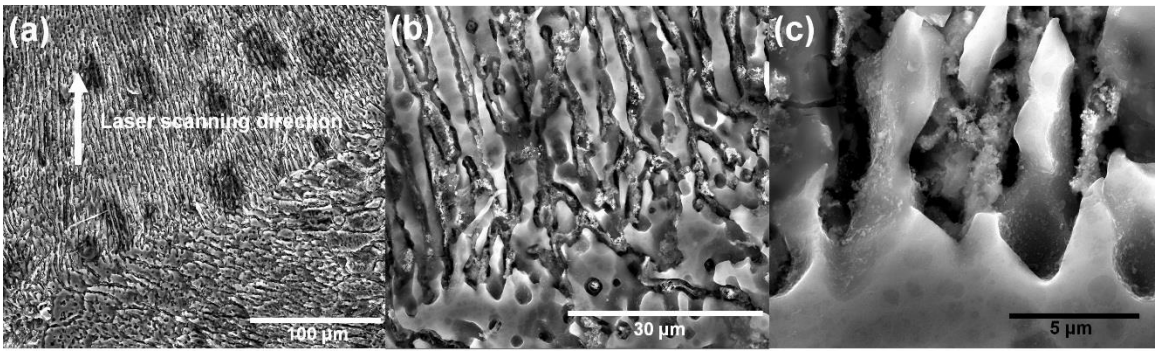

Figure 4.5 Surface microstructures of UV-LSM sample: (a) microstructure of the grains at the fusion boundary, and (b-c) high magnification microstructure of the grains exhibiting grain branching

The dendrite branching appears to be a consequence of growth of secondary/tertiary dendrites when dendrite growth velocities exceed stable dendritic growth. Now, dendrite growth rate has been calculated to be a function of dendrite tip radius by Seetharaman *et al.* [52]. The primary cause for unstable dendrite growth is most likely due overgrowth of certain dendrites, resulting in the neighboring dendrites (with slower growth rates and thus smaller sizes) to trigger secondary/tertiary dendrite formation to compensate the extra space.

4.1.4 Elemental Redistribution Analysis

The elemental distribution of the samples was performed using energy dispersive spectroscopy and has been presented in Figure 4.6. The as-received samples indicated to have a chemical composition (Al-2.78Mg-5.61Cu) similar to the commercial 2024 (Al-1.5Mg-4.35Cu) alloys. The chemical composition of the LSM sample indicated selective vaporization of magnesium and aluminum as was observed by the decrease in magnesium and aluminum content to 1.35% (from 2.78% in as-received) and 88.17% (from 90.27% in as-received) respectively, and increase in copper content to 10.23% (from 5.61% in as-received). The occurrence of selective vaporization of magnesium in 2024 aluminum alloys has been previously reported by Li *et al*. [53]. The primary reason for the selective vaporization has been attributed to the low boiling point of

magnesium and aluminum) compared to copper during the extraordinarily high temperatures reached during laser processing. The UV-LSM sample was observed to exhibit further increase amount of selective vaporization, noted by the further increase in copper content to 16.22% and decrease in aluminum and magnesium content to 79.91% and 0.95% respectively. The reason is most likely due to the extensive acoustic streaming associated with ultrasonic vibrations which result in considerable homogenization of the melt. Similar increase in homogenization due to acoustic streaming was also mentioned in the ultrasonic vibration-assisted solidification studies reported by Zhong *et al.* [54]. Therefore, as the surface of the melt pool primarily undergoes depletion of low boiling point metals (magnesium and aluminum), the vaporization rate of these metals gradually reduces due to their reduced concentration. However, the homogenization effects associated with ultrasonic vibration increases the concentration of magnesium and aluminum near the surface, resulting in further selective vaporization.

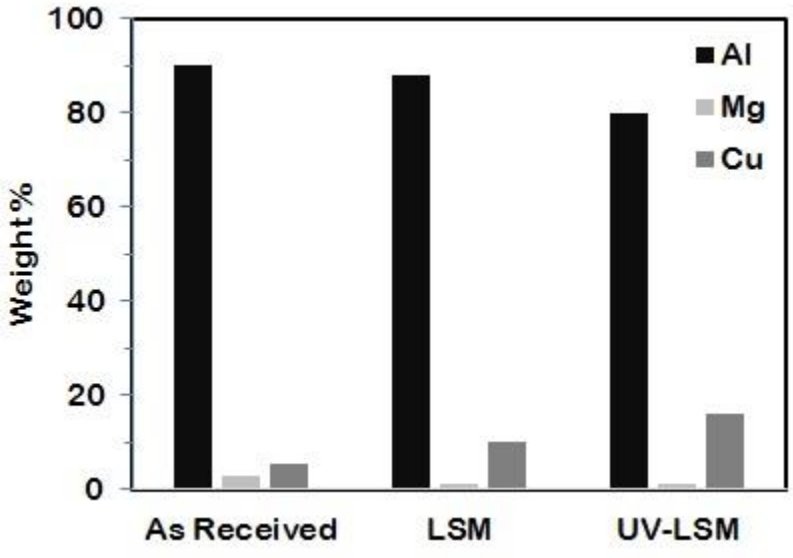

Figure 4.6. Elemental distribution of as-received, LSM, and UV-LSM samples

4.1.5 XRD Analysis

The x-ray diffraction (XRD) patterns of the as received, LSM and UV-LSM samples and their corresponding texture indices have been presented in Figure 4.7. The XRD pattern of the as received material exhibited mildly textured grains with the (111), (200), and (311) peaks exhibiting relatively lower intensity and the (220) peak exhibiting relatively higher intensity than corresponding JCPDS peaks. The XRD patterns of the LSM samples without USV however, exhibited marked preference in solidification of (111) planes, as can be observed in the dominance of the (111) peak over the other characteristic peaks. The prominence in preferential growth of (111) planes were observed to be significantly less in the USV assisted LSM samples, as can be identified by the increase in intensity to the peaks of (200), (220), and (311) planes.

The quantitative analysis of texturing was performed by calculating the texture index of the major characteristic peaks of the samples. The texture index for a particular (hkl) plane was given by the following relation [54]:

$$TC_{av}(hkl) = \frac{I(hkl)}{I_0(hkl)} \left\{ \frac{1}{n} \sum_1^n \frac{I(hkl)}{I_0(hkl)} \right\}^{-1} \quad 4.1$$

Here, I(hkl) is the relative intensity (normalized to 100) of a particular (hkl) peak, I_0(hkl) is the intensity of powder diffraction of α-aluminum as per JCPDS (card number: 04-0787), and n is the number of diffraction peaks considered in the calculations. Subsequently, the texture index of various planes was calculated for all the samples have been presented in Figure 4.8(b). Thus, as mentioned, the as-received samples exhibited mild texturing with the (111), (200), and (311) planes having lower texture indexes of 0.56, 0.83, and 0.95 while the texture index of (220) planes was 1.65. The considerable preference of the (111) planes during solidification was demonstrated by the marked increase in its texture index to 2.62 in the LSM sample while the other characteristic planes exhibited decrease in texture index. The result was in good agreement to the topographic microstructures (Figure 4.4 (a-d)), which also exhibited continuous growth of cellular grain from

the fusion interface to the core. However, it appeared that the preferential growth of (111) planes was considerably limited in the UV-LSM sample, as the texture index of the (111) planes was calculated to be 1.14. The reduction in preferential texturing was further evident by the increase in the texture indexes of the (220) and (311) planes to 1.27 and 1.32 respectively. Thus, the ultrasonic vibrations appeared to limit preferential grain growth, that was also reflected in the topographic microstructure that exhibited grain branching and promote generation of much more desirable randomly oriented grains.

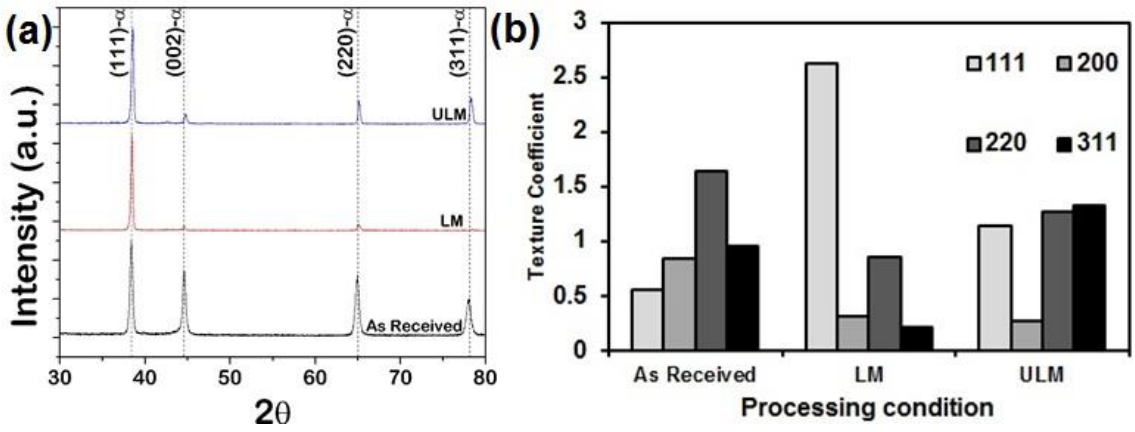

Figure 4.7. (a) XRD patterns and (b) texture coefficient of as-received, LSM, and UV-LSM samples

4.1.6 Microhardness Characterization

The variation of hardness with depth from surface has been presented in Figure 4.8.

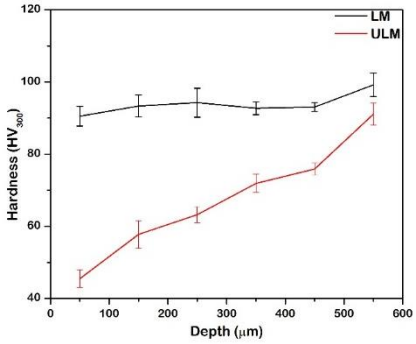

Figure 4.8 Hardness variation with depth in the melt pool of LSM and UV-LSM samples

The as received materials were observed to exhibit hardness of 104 ± 3 HV and was similar to the hardness of 2024 alloys (consisting similar chemical composition) reported by Li *et al.* [45]. It can be observed that the hardness of the LSM sample exhibited relatively lower hardness values at the surface and the hardness values gradually increased with depth. The hardness of the without LSM sample was observed to be 90 ± 3 HV and 99 ± 3 at the surface and at the fusion interface respectively. The UV-LSM sample, however, exhibited marked decrease in hardness, as can be observed from Figure 4.8. The hardness profile indicated that UV-LSM sample generated a relatively softer surface, with the surface hardness being about 45 ± 3 HV and fusion boundary exhibiting a hardness of 76 ± 2 HV. The notable decrease in hardness was primarily attributed to the presence of hard θ precipitates in the LSM microstructures while the absence of the precipitates in the UV-LSM samples resulted in generation of a supersaturated but softer surface. Thus, the high decrease in grain refinement appeared to have very little influence in the hardness of the surfaces and was found to be in good agreement with the low Hall-Petch coefficient values reported by Taha *et al.* [55].

4.2 Electrochemical Behavior of Ultrasonic Vibration-Assisted Large Area Laser Surface Melted AA2024 Alloy

The section is reproduced from the publication "Effect of simultaneous application of ultrasonic vibrations during laser surface melting on electrochemical properties of 2024 aluminum alloy" in Advanced Materials Proceedings (volume 2, issue 10, year 2017, pp 675-678) in which the student is also the first author. The investigation on laser surface melting in line scanning clearly demonstrated that the ultrasonic vibrations are highly efficient not only in generating a refined equiaxed microstructure but also promote dissolution of the precipitates. The precipitates, particularly Al_xCu_y phases are reported to be significantly cathodic in nature (compared to the α phase in the matrix) and hence readily form microgalvanic corrosion cells. Naturally, the restriction of these phases associated with laser surface melting renders this novel technique ideally suited to

develop corrosion resistant surfaces. Hence, in this investigation, the effect of laser surface melting with and without the simultaneous application of vertical ultrasonic vibrations in the electrochemical behavior was studied. To develop an adequately large surface to conduct electrochemical characterization testing (potentiostatic and potentiodynamic characterization), the samples were prepared using area scanning mode. The key processing parameters employed in this study is presented in Table 4.2.

Table 4.2 Processing parameters for laser melting of 2024 alloy without and with the simultaneous application of ultrasonic vibrations.

Sample	Power (W)	Working Distance (mm)	Scanning Speed (mm/s)	Ultrasonic Amplitude (%)
L20	950	5	20	-
L30	950	5	30	-
UL20	950	5	20	60%
UL30	950	5	30	60%

In this investigation, commercially available screws made of 2024 aluminum alloy (sample ID: 93306A712, McMaster-Carr, USA) that was carefully polished with 1200 grit size paper and subsequently cleaned with deionized water and acetone and then sand blasted to improve laser absorptivity was used as substrates.

4.2.1 Open Circuit Corrosion Behavior

The open circuit corrosion data of the as received, laser surface melted 2024 aluminum alloy with and without the simultaneous influence of ultrasonic vibrations is presented in Figure 4.9. The as received material exhibited very stable open circuit potential of about -590 mV in the initial stage (<15,000s) followed by slight decrease to about -610 mV. Such observation is common for aluminum based alloys that exhibit initial increase in open circuit potential due to formation of passive oxide (Al_2O_3) layer and eventual exfoliation of the film in the later stages due to pitting [1]. In comparison, the laser melted specimens both with (UL20 and UL30) and without (L20 and L30)

simultaneous application of ultrasonic vibrations showed significant increase in corresponding open circuit potential to about -470 to -490 mV in the initial stages. It has been reported that the rapid resolidification after laser melting results in considerable elemental redistribution, particularly segregation of copper along the grain boundaries, that renders the grain boundaries more electropositive as compared to the grain bodies [53, 56] The laser melted specimens without simultaneous application of ultrasonic vibrations (L20 and L30) manifested not only higher open circuit potential but also relatively stable potential. The open circuit potential of the L20 and L30 specimens decreased from about -475 mV to -515 mV. Such a stable open circuit potential of laser melted specimens can be attributed to higher relative stability of the passive oxide film without the destabilizing effects from the electropositive precipitates that promote pitting. Compared to laser melted specimens, the alloys laser melted with simultaneous application of ultrasonic vibrations (UL20 and UL30) exhibited notable decrease in open circuit potential with time (Figure 4.9). The open circuit potential decreased from -473 mV to -630 mV and -500 mV to -604 mV over 20,000 s for UL20 and UL 30 specimens, respectively. Since the variation in open circuit potential is often directly related with the stability of corrosion films, it can be inferred that the passive layer formation for specimens laser melted with simultaneous application of ultrasonic vibrations (UL20 and UL30) was not very efficient compared to L20 and L30 specimens.

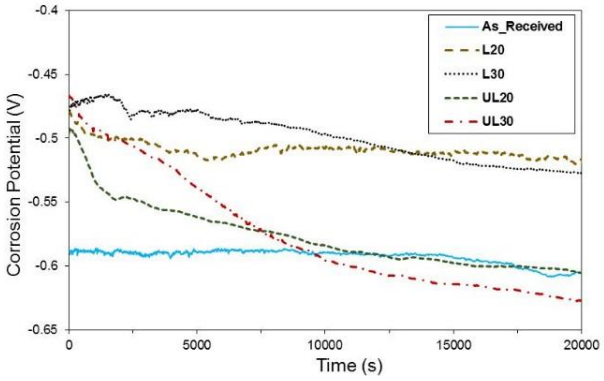

Figure 4.9 Variation of open circuit potential with time for as received and laser melted 2024 aluminum alloy with and without application of ultrasonic vibrations.

4.2.2 Microstructural Characterization

Surface microstructures of as received and laser melted 2024 aluminum alloy with and without simultaneous application of ultrasonic vibrations after immersing for 20,000s are presented in Figure 4.10. It can be clearly observed that as received specimens exhibit pitting characteristics with extensive corrosion products on the surface (Figure 4.10 (a)). The laser melted specimens without simultaneous application of ultrasonic vibrations (L20 and L30) exhibited highly plate like features for the surface oxide layer (Figure 4.10(b-c)). The formation of such conformal oxide layer with polygonal plate-like features is a characteristic of microgalvanic uniform corrosion [57]. It has been widely accepted that the passive oxide layer in aluminum alloys is primarily composed of aluminum oxide formed according to reaction [58]:

$$2Al + 6H_2O \rightarrow Al_2O_3.3H_2O\ (\text{bayerite}) + 3H_2 \qquad 4.2$$

It also indicates that the oxide layer most likely nucleated from the bulk of the grains (compared to the grain boundaries that were cathodic due to copper migration) and was a relatively stable formation process. In comparison, the laser melted specimen with simultaneous application of ultrasonic vibrations (UL20 and UL30) exhibited a corrosion mechanism highly similar to the as received specimen with porous and uneven corrosion surface (Figure 4.10 (d-e)). It appears that even the passive layer formation was not very continuous in the UL20 and UL30 specimens that resulted in the aforementioned morphology of the corrosion film. It can be inferred that while the laser melting under the influence of ultrasonic vibrations resulted in partial elimination of the precipitates. The extensive turbulence in the melt due to ultrasonic vibrations restricted the complete migration of the copper atoms towards the grain boundaries and the atoms most likely remained segregated in the grains. This observation is in good agreement with the initial passivation and eventual decay of the open circuit potential of the UL20 and UL30 specimens in the potentiostatic experiments.

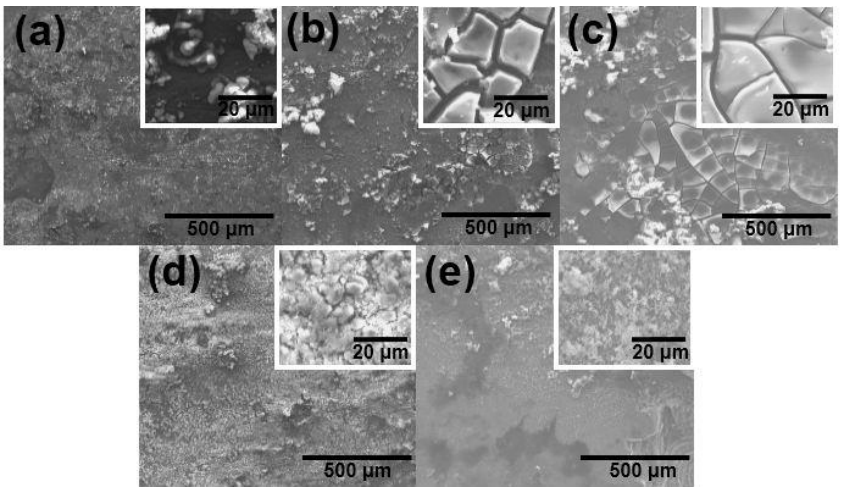

Figure 4.10 Microstructures of corroded surfaces for (a) as received, (b) L20, (c) L30, (d) UL20, and (e) UL30 specimens (higher magnification images are provided in the insets)

4.2.3 Potentiodynamic Polarization Measurements

The potentiodynamic polarization curves for as received and laser melted 2024 aluminum alloy with and without simultaneous application of ultrasonic vibrations are presented in Figure 4.11. The presence of single polarization line in each of the scans clearly indicate that the polarization current is controlled exclusively by charge transfer across the electrode-electrolyte interface [59]. Also, very similar to the observations from the potentiostatic results, it can be clearly observed that laser melting resulted in considerable improvement in corrosion potential, E_{corr} (Table 4.3). The specimens laser melted without simultaneous application of ultrasonic vibrations also showed an improvement in corrosion resistance (based corrosion current, I_{corr}, and corrosion rate calculated from Faraday's law).

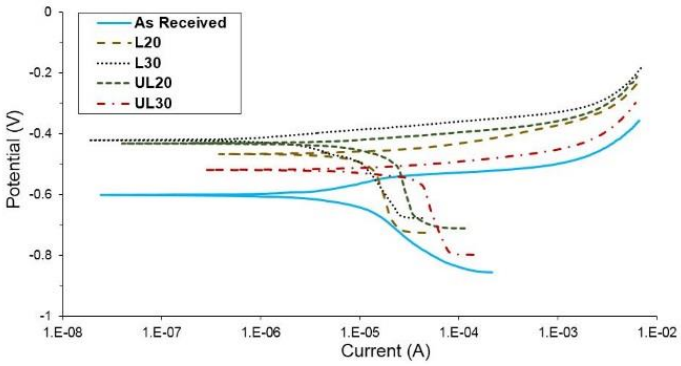

Figure 4.11. Potentiodynamic polarization curves for as received and laser melted 2024 aluminum alloy with and without simultaneous application of ultrasonic vibrations

Table 4.3 The results of potentiodynamic polarization tests on laser melted 2024 aluminum alloy with and without application of ultrasonic vibrations.

Sample	E_{corr} (mV)	I_{corr} (μA/cm^2)	Corrosion rate (μm/y)
As Received	-601	2.875	4.56
L20	-465	2.575	4.08
L30	-409	1.248	1.98
UL20	-427	5.244	8.32
UL30	-526	9.438	14.97

The application of ultrasonic vibrations during laser melting apparently resulted in slight deterioration of corrosion resistance compared to both as received and as laser melted specimens.

4.3 Ultrasonic Vibration-Assisted Laser Surface Cladding of Al-SiC Composite

This section is reproduced from the publication on the "Effect of laser remelting and simultaneous application of ultrasonic vibrations during laser melting on the microstructural and tribological properties of laser clad Al-SiC composites" in which the student is the first author [60].The investigations on ultrasonic vibration-assisted laser surface engineering of wrought aluminum and titanium alloys was primarily focused on the laser surface melting and texturing aspect of laser surface engineering. In this study, particular interest was devoted towards understanding the applicability of simultaneous application of ultrasonic vibrations in laser surface

cladding. Major emphasis was devoted towards understanding the microstructural evolution of the clad layer as well as the remelted surface layer and subsequently the fundamental relationship of the microstructure with the tribological performance was studied. Also, the ultrasonic vibrations are generated by an acoustic apparatus that transfer the vibrations primarily in monolithic medium (unlike the initial preplaced clad layers comprising primarily of powders). Hence, this study also incorporated remelting of the clad layer (by rescanning the clad layer) to investigate the effect of the remelting operation on the microstructural evolution of clad layer. The aluminum alloy specimens (Mcmaster-Carr, sample ID: 93306A712) were carefully polished using 1200 grit size paper, sand blasted, and subsequently cleaned with to remove surface impurities. Commercially pure Al (particle size: 10–14 µm) and SiC (particle size: 10.6 µm) powder mixture in the 80:20 ratio by weight was ball milled for 15 min at 300 rpm. Subsequently, a slurry of the powder mixture was prepared using water soluble organic binder (LISI W 15853) and reducer (LISI W 15833) and was sprayed on the surface of the AA2024 substrate. Table 4.4 presents the key processing parameters used in this investigation.

Table 4.4. Processing conditions used for laser surface cladding of 2024 aluminum alloy with SiC

Processing Conditions Sample ID		Laser Melting		Laser Remelting	
		Vibration Amplitude (%)	Scan Speed (mms^{-1})	Vibration Amplitude (%)	Scan Speed (mms^{-1})
Laser processed without vibrations	LM	-	10	-	-
	RM	-	10	-	3.33
Laser processed with vibrations	ULM	80	10	-	-
	URM	-	10	80	3.33

4.3.1 Clad Layer Characteristics

The microstructures of the laser cladded specimen exhibited the formation of a very distinct composite cladded zone and melt zone. The data for the final clad layer thickness for different

samples calculated from cross-sectional SEM microstructures is presented in Figure 4.12(a). The composite clad layer thickness was about 31.73 μm, 32.57 μm, 39.21 μm, and 60.11 μm for LM, RM, ULM, and URM specimens, respectively. Figure 4.12(b) presents the relative change in the ratio of thickness of the final clad layer (C) to the thickness of initial sprayed powder layer thickness (I). Clearly, significant increase in C/I ratio was observed after remelting operation in the laser processing both with and without simultaneous application of ultrasonic vibrations. The C/I ratio increased from 34.75% for LM to 57.93% for RM while it increased from 37.53% for ULM to 60.11 % for URM specimens. Note that laser melting results in the formation of dense composite layer on the surface. The subsequent remelting of this dense layer causes in further deepening of laser melted pool and additional mixing of the reinforced particles in the pool, resulting in thicker composite clad layers and higher C/I ratios as observed for RM and URM specimens. The effect of the ultrasonic vibration was also observed to improve the thickness of composite clad layer and C/I ratio in both the melted and remelted specimen. The thickness of the composite clad layer increased from 31.73 μm for LM to 39.21 μm for ULM while the C/I ratio increased from 34.75% for LM to 37.53% for ULM. The composite clad thickness and C/I ratio of 60.11 μm and 61.04%, respectively, was observed for URM specimens. It has been widely recognized that ultrasonic vibrations cause cavitation and improve fluid convection in the solidifying melt [61, 62]. The effects of ultrasonic vibration assistance have been utilized for grain refinements in the castings [40]. It appears that similar effects cause deeper penetration of ceramic particles in the melt pool during laser composite surfacing, resulting in thicker clad layer thickness and improved C/I ratio in specimens laser melted and remelted with simultaneous assistance of ultrasonic vibrations.

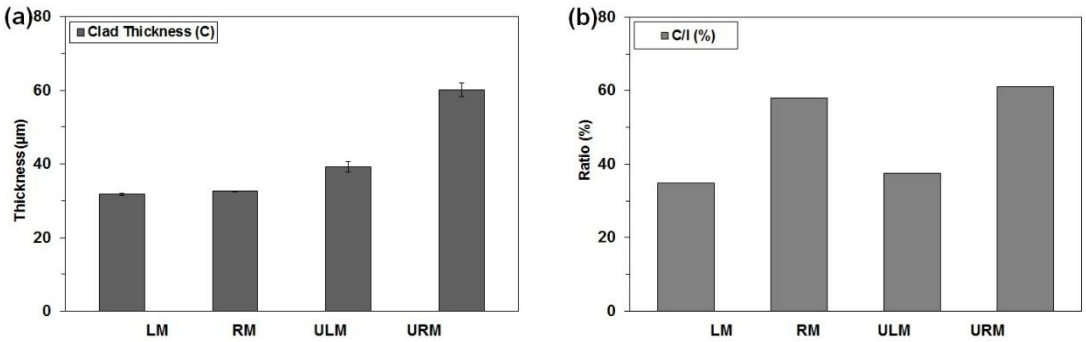

Figure 4.12. Variation of (a) composite clad layer thickness (C), and (b) ratio of clad layer thickness to initial preplaced powder thickness (C/I) with laser processing conditions.

4.3.2 XRD Characterization

XRD patterns from the surface of the laser clad Al-SiC composite specimens are presented in Figure 4.13(a). While the patterns from all the specimens exhibited characteristic peaks of α-Al and SiC, some variation in the intensity of peaks was observed. To study the evolution of texture in the specimens, the texture coefficient (TC) was estimated using characteristic peaks of α-Al, according to [63]:

$$TC_{hkl} = \frac{I(hkl)}{I_0(hkl)} \left\{ \frac{I}{n} \sum_1^n \frac{I(hkl)}{I_0(hkl)} \right\}^{-1} \quad 4.3$$

where, *I(hkl)* is the observed relative intensity of a specific *(hkl)* peak, $I_0(hkl)$ is the relative intensity of standard *(hkl)* peak of pure Al (JCPDS: 04-0787), and *n* is the number of diffraction peaks considered in the calculations. The texture coefficients for the all the laser clad Al-SiC surfaces for different crystallographic planes are presented in Figure 4.13(b). It should be noted that while the resolidified microstructure under the composite clad layer exhibited the typical cellular dendritic grains, the clad layer of the treated specimens exhibited very restricted texturing, suggesting limited opportunity for preferential solidification. It appears that reinforced SiC particles in the composite clad layer restrict the development of preferential texture in the surface. For example, the TC was estimated to be about 0.92 for (311) plane and about 1.1 for (220) plane for specimen LM specimens, indicating random texture.

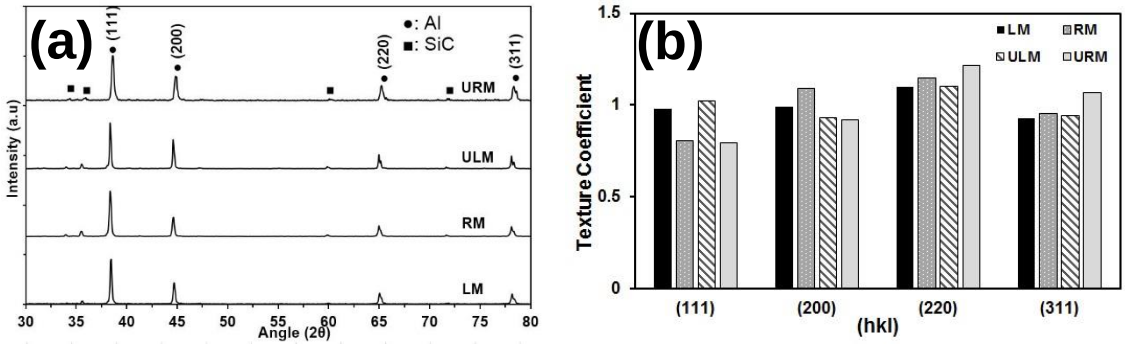

Figure 4.13 (a) XRD patterns and (b) texture coefficients for laser clad Al-SiC composite surfaces processed with different laser processing conditions.

It is expected that the cavitation and enhanced convection in melt pool due to application of ultrasonic vibrations during laser melting, in addition to the presence of SiC particles, severely restrict the grain growth and retain random texture in ULM specimens. However, the laser clad composite surfaces processed by laser remelting (RM and URM) exhibited slightly higher texture coefficients. For example, texture coefficients for (220) plane were estimated to be 1.14 and 1.21 for RM and URM, respectively. The results indicate that laser remelting, both with and without simultaneous application of ultrasonic vibrations, results in slightly higher texturing compared to laser specimens.

4.3.3 Microstructural Characterization

As mentioned earlier, the laser processing resulted in the formation of a very distinct composite clad layer at the top surface and thicker resolidified zone underneath the clad layer, as presented in Figure 4.14. The resolidified melt zone thickness of about 150-200 μm was observed for all the specimens. The resolidified zone exhibited typical epitaxial cellular/dendritic morphology characteristic of rapid solidification observed in laser processing [53]. The SiC particles penetrated only near the surface of the melt pool, forming a distinct composite clad layer at the top. The higher magnification microstructures of the composite clad layer for different processing condition are also presented in Figure 4.14. The microstructures of the laser clad zone

revealed presence of acicular needle-like phase. The formation of needle-like phase is a common feature in laser surface engineering of Al-SiC composites and has been widely reported to be eutectic acicular α-Si phase [64-66]. Also, the acicular α-Si phase is observed to nucleate from the SiC particles [67]. The microstructures also exhibited presence of pores and microcracks, that appeared to be more pronounced in the URM samples while the LM samples exhibited virtually crack/pore free substrate. Naturally, the additional energy provided during the remelting operation as well as the activation of cavitation with ultrasonication resulted in such the aforementioned pores/microcracks in the clad layers of the URM samples. While the acicular α-Si phase is observed for all the specimens, the composite layers clad with remelting, both with and without application of ultrasonic vibrations (RM and URM), showed a marked reductions in the relative percentage of this phase compared to the specimens processed by just laser melting (LM and ULM). It appears that the remelting of the laser clad layer causes partial melting of the needle-like phase formed during initial melting step. Also, the specimens processed with the simultaneous application of ultrasonic vibrations (ULM and URM) showed some reduction of needle-like phase. The application of ultrasonic vibrations during laser melting appears to suppress the interfacial reactions and decomposition of SiC possibly due to cavitation and enhanced fluid convection.

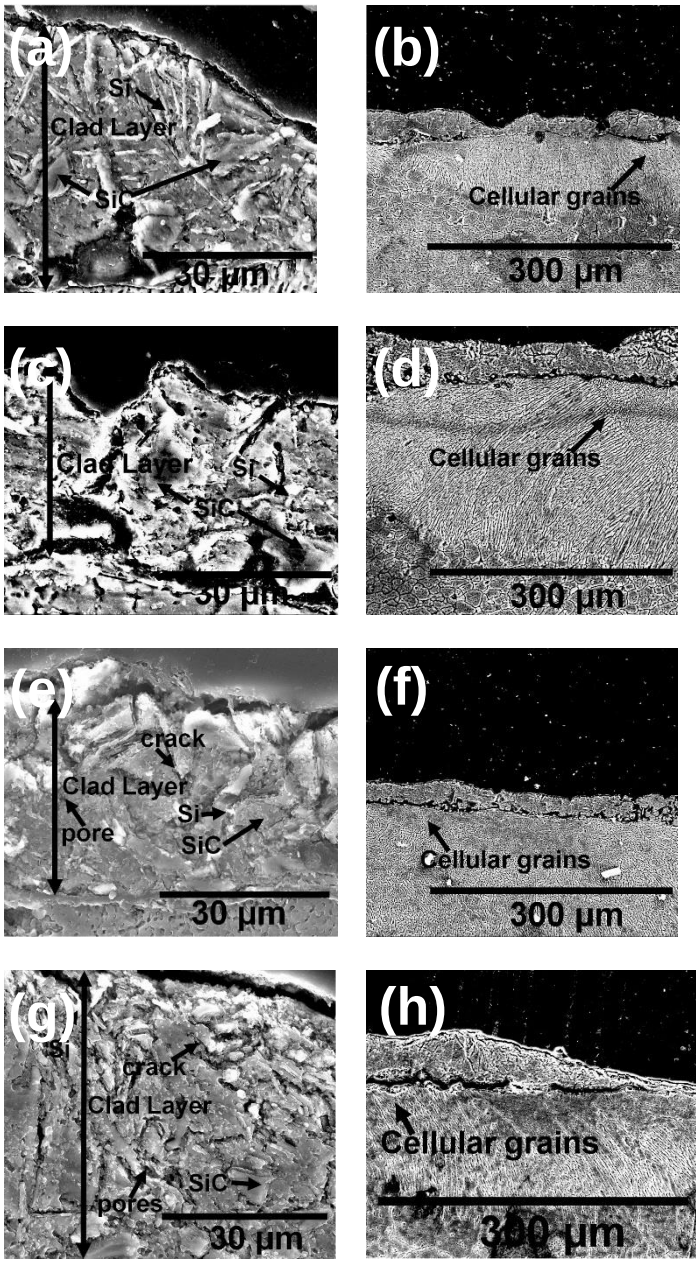

Figure 4.14 SEM micrographs from laser clad Al-SiC composite surfaces: (a-b) LM, (c-d) RM, (e-f) ULM, and (g-h) URM

4.3.4 Tribological Analysis

The wear rates of the laser clad Al-SiC composite surfaces processed with laser melting and remelting, both with and without the simultaneous influence of ultrasonic vibrations, are presented in Figure 4.15. The laser remelted specimens processed with both the conditions (i.e.

without and with simultaneous application of ultrasonic vibrations) exhibited marked improvement in wear resistance.

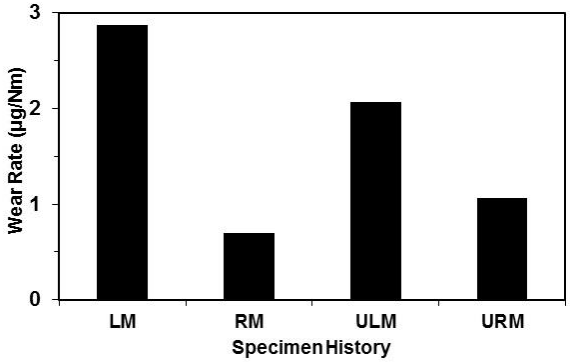

Figure 4.15 Total wear rate for laser clad Al-SiC composite surface processed with different laser processing conditions.

For example, the total wear loss decreased from 2.87 $\mu gN^{-1}m^{-1}$ for LM to 0.7 $\mu gN^{-1}m^{-1}$ for RM while it decreased from 2.07 $\mu gN^{-1}m^{-1}$ for ULM to 1.07 $\mu gN^{-1}m^{-1}$ for URM specimens. On the other hand, the effect of ultrasonic vibrations on the wear rate was not consistent. The application of ultrasonic vibration during laser processing was observed to improve the wear resistance for laser melted specimens. The wear rate decreased from 2.87 $\mu gN^{-1}m^{-1}$ for LM to 2.07 $\mu gN^{-1}m^{-1}$ for ULM specimens. For the laser remelted specimens, the application of ultrasonic vibrations resulted in slight increase in wear rate (0.7 $\mu gN^{-1}m^{-1}$ for RM to 1.07 $\mu gN^{-1}m^{-1}$ for URM). As discussed in the previous section, the laser remelting and ultrasonic vibration assist cause microstructural modification in the composite clad composite layer, especially the reduction in needle-like α-Si phase. It is well recognized that needle-like α-Si phase increase the brittleness of the material and is detrimental to the wear performance. The marked reduction in the wear rate for remelted specimens (RM and URM) appears to be partly due to microstructural modification characterized by reduction in needle-like α-Si phase. As wear performance is also influenced by surface features of the specimens, surface roughness (Rz) of the laser clad Al-SiC composite specimens was also characterized (Figure 4.16).

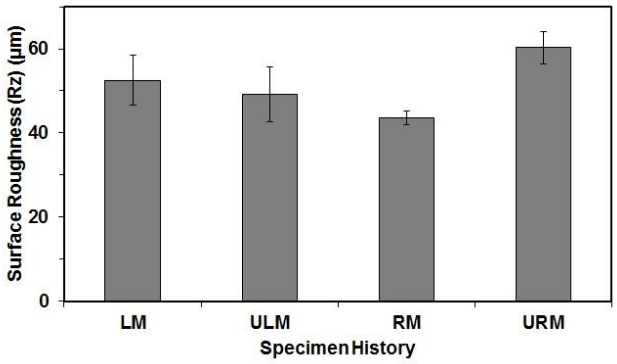

Figure 4.16 Surface roughness (R_z) of laser clad Al-SiC composite surface processed with different laser processing conditions.

In the specimens laser processed without simultaneous application of ultrasonic vibrations, the laser remelting resulted in reduction in surface roughness (from 53 µm for LM to 44 µm for RM). Such an improvement in surface finish has likely contributed to a marked reduction in wear rate observed for RM specimens. It should be noted that superior surface finish has often been reported to improve tribological properties [68, 69]. On the other hand, laser melting and remelting under the influence of ultrasonic vibrations resulted in slightly higher surface roughness. The surface roughness was observed to be 49 µm and 60 µm for ULM and URM specimens, respectively. The higher surface roughness of ULM and URM specimens is a direct result of melt cavitation and turbulence in melt pool during laser melting and remelting under the influence of ultrasonic vibrations. This effect of ultrasonic vibrations on melt pool instability during laser melting is well reported in literature. In spite of some microstructural modifications, the higher surface roughness in the ULM and URM resulted in inconsistent wear performance. Figure 4.17 presents the scanning electron micrographs of the wear tracks of the laser clad Al-SiC surfaces.

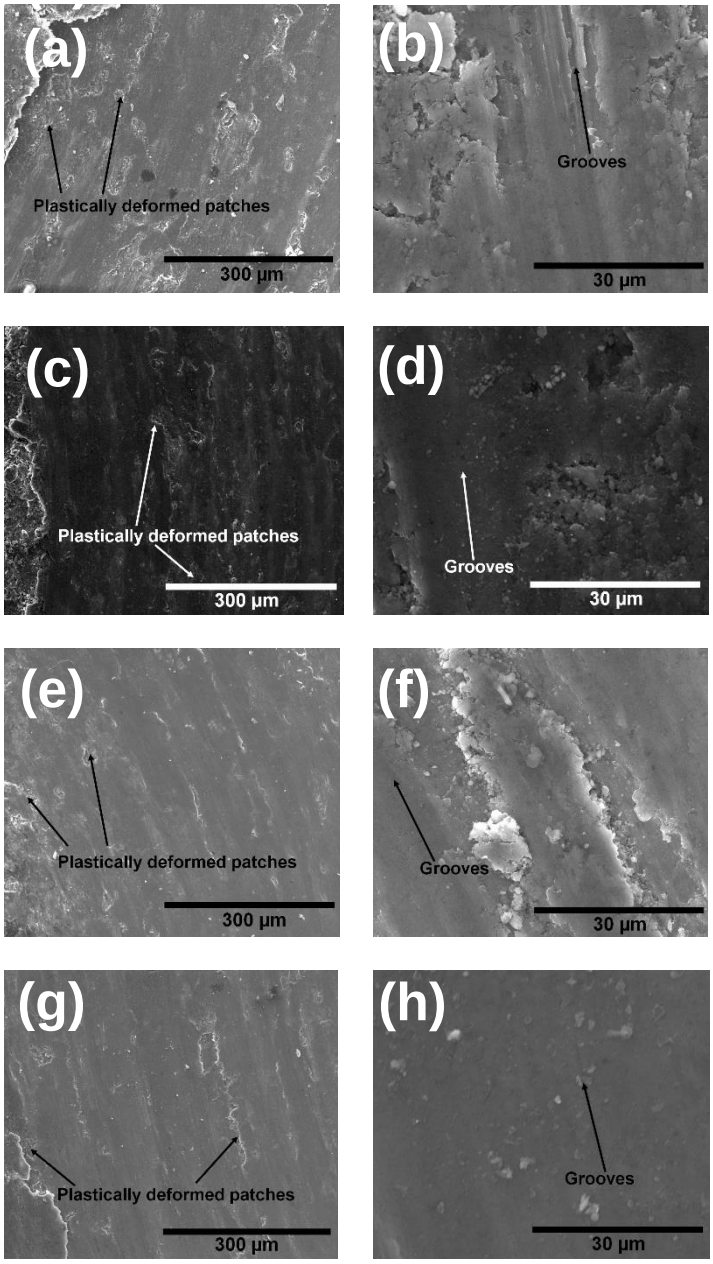

Figure 4.17 Low and higher magnification microstructures of wear surfaces of laser clad Al-SiC composites: (a-b) LM, (c-d) RM, (e-f) ULM, and (g-h) URM samples

It can be observed from Figure 17 (a-h) that deep grooves are present on the wear tracks of all the samples. It has been widely confirmed that the grooves are exclusively associated with the ploughing mechanism of abrasive wear [70]. Also, since mass loss during wear is predominantly caused by abrasive wear, the occurrence of abrasive wear can be deducted for the laser clad

composite surfaces. Obviously, the high hardness of the counterbody (Al_2O_3) as well as the abrasive action of the SiC-rich wear debris from the composite clad layers are the primary causes for the abrasive wear. In addition to deep grooves indicative of abrasive wear, discontinuous patches were also observed on the wear tracks. The presence of such patches indicates that the material removal during wear did not proceed through a very continuous regular rate but was irregular, with certain patches undergoing extensive plastic deformation followed by plastic rupture. Similar deformation patches in wear process were also observed in the wear experiments on laser surface cladded Al-SiC specimens [70, 71]. It was reported that total area of such patches increases at higher loads, and it is also accompanied with increase in coefficient of friction.

4.4 Laser Surface Melting of Al-SiC Metal Matrix Composites

The investigation on laser surface cladding of wrought aluminum plates with aluminum and silicon carbide showed that the energy input from laser triggers significant chemical reactions between the aluminum matrix and silicon carbide particles. However, due to the relatively low amplitude of the ultrasonic vibrations (less than 1 μm), the results clearly indicated that silicon carbide particles did not undergo extensive penetration in the melt. Hence, in this study, the major motivation was to study the effect of laser processing in an Al-SiC matrix with well distributed dispersion of the SiC particles. The laser power and scanning velocity was systematically varied to understand the effect of the aforementioned processing parameters on the microstructural and phase evolution, surface roughness, and tribological properties of the material. The formation of phases due to particle-matrix interactions was studied in detail using microscopy and XRD characterization techniques. The processing conditions has been summarized in Table 4.5. Commercial Al-SiC plates (thickness: 5 mm) comprised of 80% A356 (cast Al-7% Si alloy) and 20% SiC was used in this investigation. The Al-SiC plates carefully polished with 1200 grit size sand paper, cleaning with acetone and deionized water. The samples were subsequently sand blasted to improve laser absorption by increasing surface roughness.

Table 4.5 Processing conditions employed for laser surface melting of Al-SiC composites

Sample ID	Laser Power (W)	Scan Speed (mm/s)	Beam Length (mm)
P250S5	250	5	19.05
P250S10	250	10	19.05
P250S15	250	15	19.05
P300S5	300	5	19.05
P300S10	300	10	19.05
P300S15	300	15	19.05
P350S5	350	5	19.05
P350S10	350	10	19.05
P350S15	350	15	19.05
P400S5	400	5	19.05
P400S10	400	10	19.05
P400S15	400	15	19.05

The effect of laser processing parameters, that is, laser power and decrease in scanning speed and its subsequent effect on the surface roughness was studied. Finally, the effect of the laser processing on particle-matrix bonding as well as surface roughness on the surface tribological was studied. Since particle-matrix bonding is often associated with improved load bearing in the composite, improvement in bonding can potentially improve tribological performance of the alloys. Major emphasis was given towards understanding the effect of processing conditions by systematically varying the key processing conditions: laser power and scanning speed. Subsequently, its effect on the microstructure and phase evolution, surface texture and roughness of the laser melted surface and their influence of tribological performance was studied in detail.

4.4.1 XRD Analysis

The x-ray diffraction (XRD) patterns of the as-received and laser surface melted Al-SiC samples are presented in Figure 4.18. The XRD pattern of the as received sample exhibited all the characteristic peaks of the major constituents of the composite: aluminum, silicon, and silicon carbide. In comparison, the laser surface melted substrates exhibited emergence of complex intermetallic phases such as Al_4C_3, Al_4SiC_4. The formation of these phases is consistent with investigations on laser surface cladding of aluminum with silicon carbide [60, 66]. The as-received samples is mentioned as AR in this text henceforth.

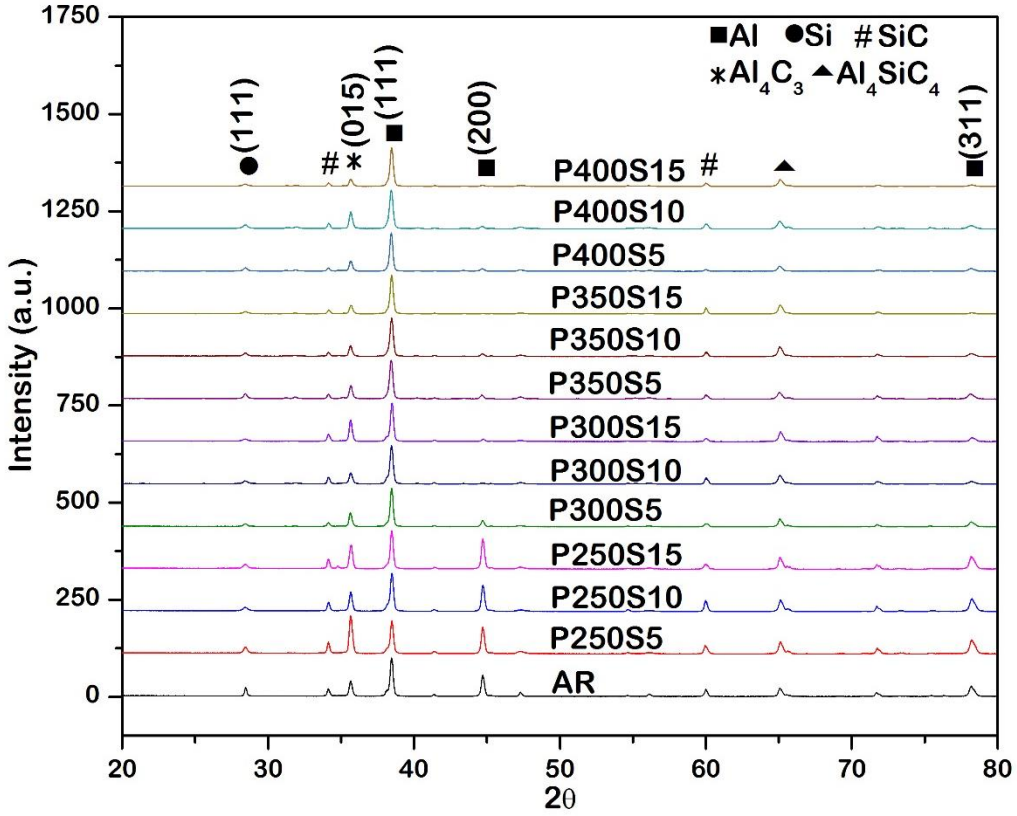

Figure 4.18 XRD patterns of laser surface melted Al-SiC substrates processed with systematic variation in laser power and scanning speed

The studies have confirmed that formation of these phases occur as the thermal energy from the laser beam partially melts the silicon carbide particles and the molten constituents react with the matrix (aluminum) to trigger the following reactions:

$$4Al + 3SiC = Al_4C_3 + 3Si \quad (4.4)$$

$$4Al + 4SiC = Al_4SiC_4 + 3Si \quad (4.5)$$

Since the thermal energy from the laser processing is primarily responsible in the formation of these phases, it was observed that the relative intensity of the peaks increased with increase in laser power and decrease in laser scanning velocity. It should be noted that these phases are highly brittle and therefore are highly undesired as it results in significant deterioration of surface properties such as toughness and moisture resistance. Indeed, use of laser with lower power input has been employed to suppress the formation of these phases in welding studies of Al-SiC substrates [72]. Another striking feature observed in the XRD patterns was the lateral shift of the characteristic peaks to higher angles with increase in both laser power and decrease in scanning velocity. Now, shift of characteristic peaks to higher is often associated with residual compressive stresses in the matrix [73]. This is most likely due to the higher volume of the complex intermetallic phases (Al_4C_3, Al_4SiC_4) compared to the reactants that increased the total volume of the zone surrounding the precipitated phases, thereby imparting compressive stresses to the particles.

4.4.2 Surface Roughness and Microstructural Analysis

The surface microstructures of the laser surface melted samples are presented in Figure 4.19. It can be clearly observed that the laser surface melting resulted in a highly conformal, crack-free laser surface melted zone. Also, the laser melted surface exhibited linear tracks corresponding to the laser line scans. The laser melted samples exhibited needle-like phases surrounding the silicon carbide particles. The presence of needle-like features is a common observation in laser processed Al-SiC composites and has been identified to be comprised of acicular α-Si, Al_4C_3, and Al_4SiC_4 [60, 66].

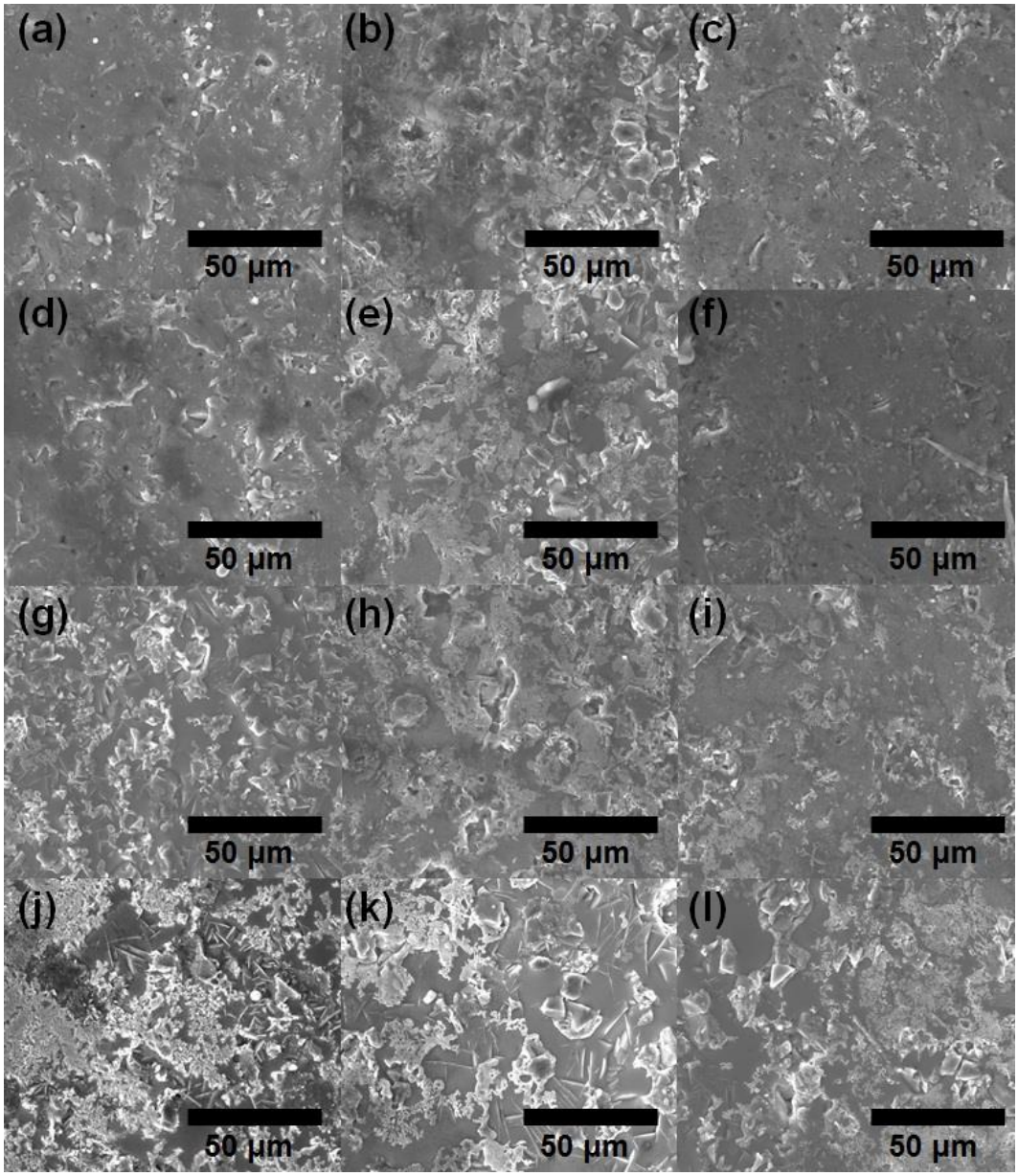

Figure 4.19 High angle magnification SEM micrographs of P250S5, P250S10, P250S15, P300S5, P300S10, P300S15, P350S5, P350S10, P350S15, P400S5, P400S10, and P400S15

This observation was also reflected in the XRD patterns of the laser melted samples exhibited presence of phases such as Al_4C_3, Al_4SiC_4. The needle-like phases were observed to be more prominent with increase in laser power and decrease in scanning speed. Obviously, this is a consequence of the increased thermal energy input from the laser that increased the overall volume fraction of the precipitated phases. The presence of the intermetallic phases surrounding the also

indicated that although the laser processing resulted in formation of undesirable intermetallic phases surrounding the matrix, it has also been associated with improved particle-matrix bonding. The primary reason for the improved particle-matrix bonding has been attributed to the increased metallurgical bonding between the particle and matrix due to the intermetallic reactions.

The effect of the processing conditions on the roughness of the laser melted surface was further studied using 3D profilometry and the results have been presented in Figure 4.20. It can be clearly observed that the surface roughness of the exhibited progressive increase with increase in laser power and decrease in scanning speed. It should be noted that both increase in laser power and decrease in scanning speed increases the total thermal energy introduced to the substrate.

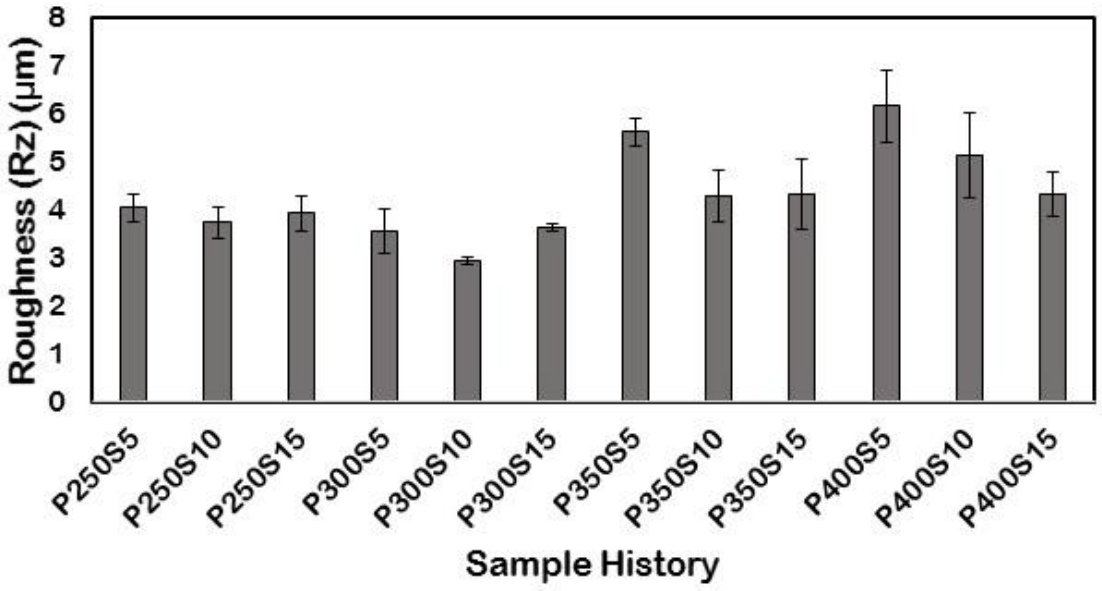

Figure 4.20 Surface roughness of laser surface melted samples processed with variation in laser power and scanning speed

Now, the surface roughness is primarily contributed by physical and chemical transformations on the surface such as deformation and chemical reactions are primarily triggered by the thermal energy from the laser irradiation. Therefore, as the total thermal energy introduced increased with increase in laser power and decrease in scanning speed, the surface deformation and chemical reactions increased thereby resulting in increased surface roughness.

4.4.3 Tribological Characterization

The wear rate of the as-received and laser surface melted substrates has been presented in Figure 4.21. It can be observed that the most of the laser melted samples exhibited relatively lower coefficient of friction compared to the as-received counterparts. For instance, the P250S5 samples exhibited wear rate of 1.592 μg/Nm compared to 2.035 μg/Nm exhibited by as received samples. The reduction in wear rate due to decrease in sub-surface damage has been illustrated in several investigations on tribological behavior of copper-silicon carbide metal matrix composites [74]. The authors reported that compared to base material, the composites exhibited significantly lower wear rate and the reduced lamellar cracks, that occurs due to plastic strain localization in the sub-surface region. Therefore, the improved wear behavior can be naturally associated with the improved particle-matrix bonding that resulted in reduced strain-localization and subsequently improved wear resistance.

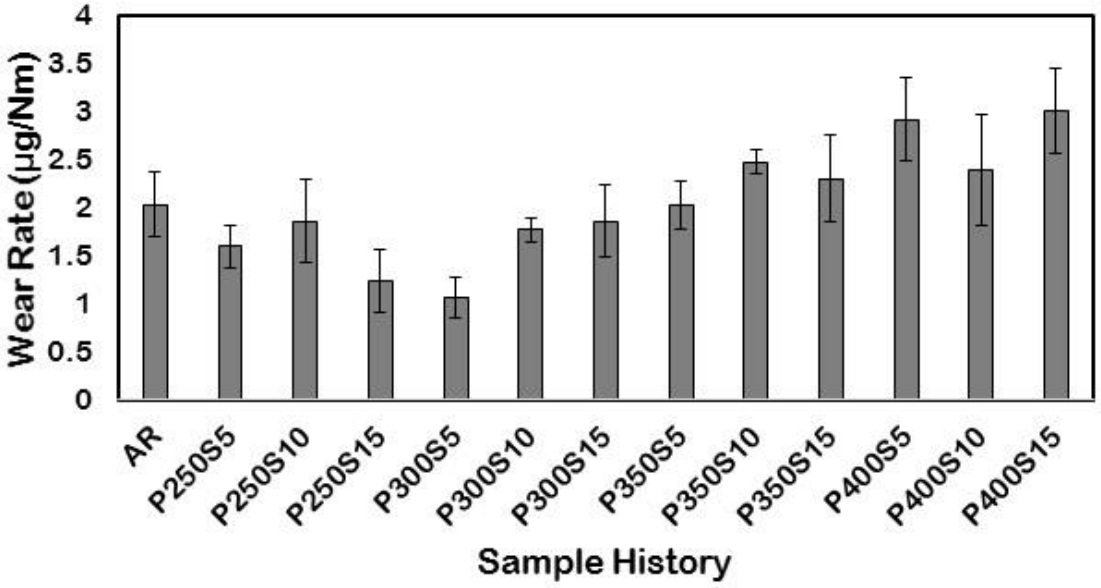

Figure 4.21 Wear rate of laser surface melted samples processed with variation in laser power and scanning speed

Indeed, the improvement in wear resistance due to superior particle-matrix bonding is remarkably similar to the findings on cavitation behavior of laser surface melted Al-SiC composites by Man *et al.*[75]. However, wear behavior has been widely accepted to be a highly complex phenomenon contributed by several factors such as surface mechanical properties, roughness and constituent phases. Hence, although the particle-matrix bonding was significantly improved with the laser surface melting, the formation of embrittling phases such as Al_4C_3, Al_4SiC_4 as well as the increased surface roughness contributed in aggravating the wear rate of the material. This observation was particularly evident in the higher power substrates such as that exhibited wear rate of compared to of. Hence, it appears that the P250S5, P250S15, and P300S5 substrates exhibit the optimum combination of improved particle-matrix bonding without extensive triggering of brittle intermetallic phases and surface deformations. The average coefficient of friction of the as-received and laser surface melted samples have been presented in Figure 4.22. It can be clearly observed that compared to the as-received (coefficient of friction about 0.547), the laser melted substrates exhibited relatively lower coefficient of friction. It should be noted that previous investigations on tribological behavior of Al-SiC composites have indicated that fracture of particles significantly influences the coefficient of friction [76]. Hence, as the particle-matrix bonding was improved with the laser surface melting treatment, the Hertzian load distribution during the wear treatment was more uniform, resulting in delayed fracture of the particles. The slight aberrations in this trend (coefficient of friction being lower than as-received) was exhibited by some samples, for example the P400S10 sample exhibiting a higher coefficient of friction of 0.56 compared to 0.547 of the as-received samples.

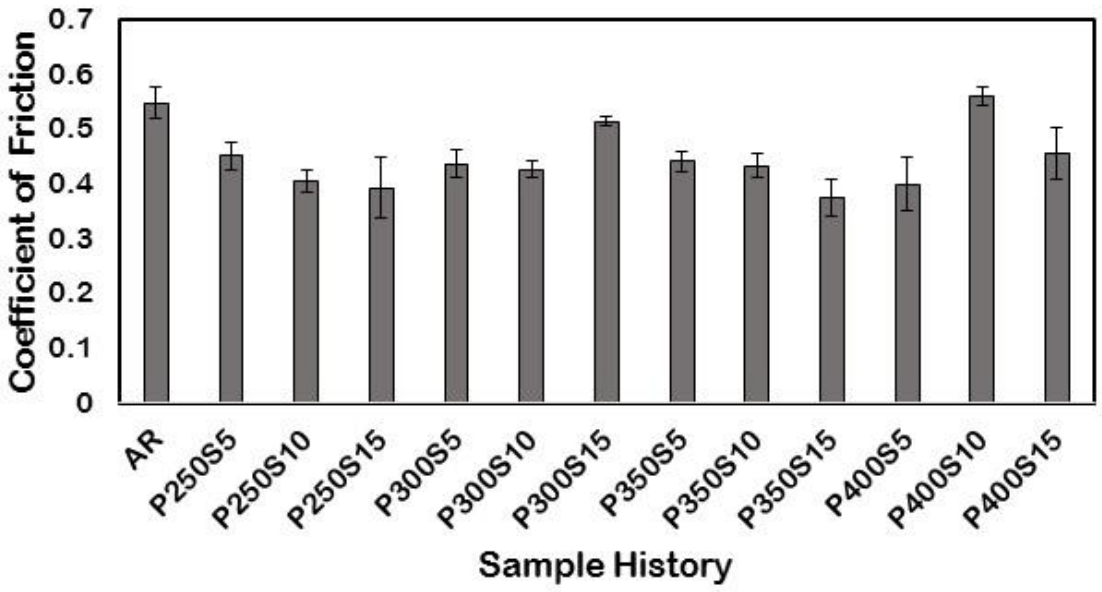

Figure 4.22 Average coefficient of friction of as-received and laser surface melted samples

4.5 Ultrasonic Vibration-Assisted Spot Laser Surface Melting of Ti-6Al-4V Alloy

This section is reproduced from the publication "Laser surface melting of Ti–6Al–4V under the influence of ultrasonic vibrations" in which the student is also the first author [77]. The investigation of laser surface melting of aluminum, with and without the simultaneous application of vertical ultrasonic vibrations on the substrate clearly demonstrated the efficiency of ultrasonic vibrations in developing a refined equiaxed microstructure with significantly reduced crystallographic texturing. However, the grain refinement strengthening (or Hall-Petch strengthening) is not particularly efficient in improving mechanical properties of aluminum the Hall-Petch constant of aluminum is considerably low (k_{Al} = 0.06 MPa $m^{1/2}$ compared to k_{Ti} = 0.4 MPa $m^{1/2}$) [78, 79]. Furthermore, the high strength wrought aluminum alloys are precipitation hardened. Therefore, elimination of precipitates associated with laser melting is almost always associated with reduction in mechanical strength that was reflected in Figure 4.8. Hence, in this investigation, Ti-6Al-4V alloy was selected as substrate material to investigate the effect of ultrasonic vibration-assisted laser processing on the mechanical properties such as hardness and wear resistance as titanium alloys are reported to exhibit significantly better Hall-Petch

strengthening compared to aluminum alloys. In this study, spot melting of grade V titanium (Ti-6Al-4V) was performed with and without the simultaneous influence of ultrasonic vibrations. Commercial Ti–6Al–4V samples (McMaster-Carr, USA, sample ID: 94081A337) were screwed on the threaded probe for the laser processing. The samples were processed with an irradiation time of 2.5 s. The LSM experiments were conducted using a continuous wave CO_2 laser (Ferranti, Manchester, UK) operated with the output power of 900 W and working distance of 35 mm (beam size: 4.89 mm). The experiments were performed with stationary irradiation at a spot (i.e. no scanning of surface). The LSM under the influence of ultrasonic vibrations was conducted with two ultrasonic power outputs of 25% and 30%.

4.5.1 Microstructural Analysis

The cross-sectional SEM images of the Ti-6Al-4V samples laser surface melted without and with the influence of the ultrasonic vibrations are presented in Figure 4.23. The sample laser melted without the ultrasonic vibrations shows a very well-defined resolidified region with a melt depth of about 434 µm and width of about 1572 µm (Figure 4.23(a)). A small depression of about 80 µm at the center of the melt pool was also observed. It has been widely reported that the formation of such depressions/ripples during LSM is primarily due to surface tension effects established by temperature gradient in the melt pool. When the LSM was performed under the influence of ultrasonic vibrations, significant melt expulsion was observed, resulting in the formation deep crater on the resolidified surface of the material (Figure 4.23(b)-(c)). While the depth of crater increased from 454 to 610 µm, the thickness of resolidified layer decreased from 272 to 231 µm with increasing ultrasonic power output from 25 to 30%. Clearly, the ultrasonic vibrations of increasing intensity appear to generate extensive agitation in the melt pool and cause more efficient melt expulsion from the surface of the laser melted Ti-6Al-4V samples.

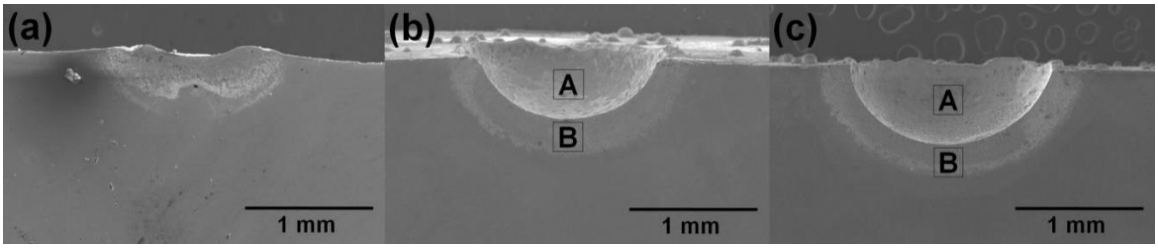

Figure 4.23 Cross-sectional micrographs of laser surface melted Ti-6Al-4V: (a) without ultrasonic vibrations, (b) with ultrasonic vibration power output of 25%, and (c) with ultrasonic vibration power output of 30%. The craters resulted from melt expulsion are marked "A" and resolidified regions are marked "B".

The high magnification images of the laser melted Ti-6Al-4V without the application of ultrasonic vibrations show three distinct regions (Figure 4.24). The microstructure consisted of large columnar/dendritic grains with average grain size of 8.44±3.04 μm near the central region of the resolidified pool (region A). These grains appear to grow towards the center of the melt pool as observed during directional solidification. The grains appear to become more regular deeper in the resolidified regions (region B). The microstructure consists of predominantly fine dendritic grains in the resolidified region near the fusion boundary (region C). The microstructures also show shallow (~60 μm thick) heat affected zone (HAZ) in the substrate below the fusion line. While most of the previous investigations have reported formation of acicular martensite (α') phase after laser melting of Ti-6Al-4V, the well-defined grain structure at the surface observed in the present investigation appears to consist of predominantly α grains. Note that the martensite HCP α' phase has similar lattice parameters to the HCP α phase. The XRD analysis also confirmed the presence of HCP phase (α or α'); no reflections of BCC β phase were observed in the XRD patterns (not shown). The microstructures of the laser surface melted Ti-6Al-4V samples under the influence of ultrasonic vibrations were distinctly different from those observed in Figure 4.24. It was observed that the ultrasonic vibrations completely eliminated the columnar/dendritic grains, and the microstructure was uniform along the depth of the resolidified region with significant grain refinement (Figure 4.25). The grain distribution was more random and didn't show any apparent

morphological texturing as commonly observed during directional solidification. The grain refinement during solidification occurs through several different mechanisms. It has been reported that solidification conditions in some cases can decrease the constitutional supercooling, favoring the grain refinement. Due to high cooling rates associated with laser surface processing, the solidification conditions are likely to be far from equilibrium and it is difficult to maintain very high chemical homogeneity in the melt. In fact, segregation of Al has been reported during selective laser melting of Ti-6Al-4V [80]. It seems that the application of ultrasonic vibrations during LSM enhances the fluid flow in melt and causes cavitation, resulting in the fragmentation of dendrites. The fragmentation of dendrites is one of the commonly observed mechanisms of grain refinement during conventional solidification under the influence of external forces. This study offers the evidence of grain refinement under rapid solidification encountered during LSM under the influence of ultrasonic vibrations. The HAZ (~45-60 μm) is also observed in the samples laser melted under the influence of ultrasonic vibrations.

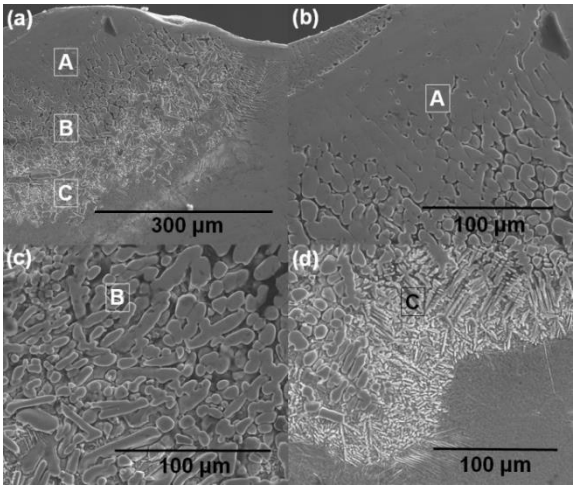

Figure 4.24 Cross-sectional SEM micrographs of without USV-LSM Ti-6Al-4V samples: (a) Low magnification microstructure exhibiting three distinct resolidified zones, (b) Large columnar dendritic grains near the surface, (c) Smaller dendritic grains at moderate melt depth, and (d) superfine equiaxed grains at the molten interface

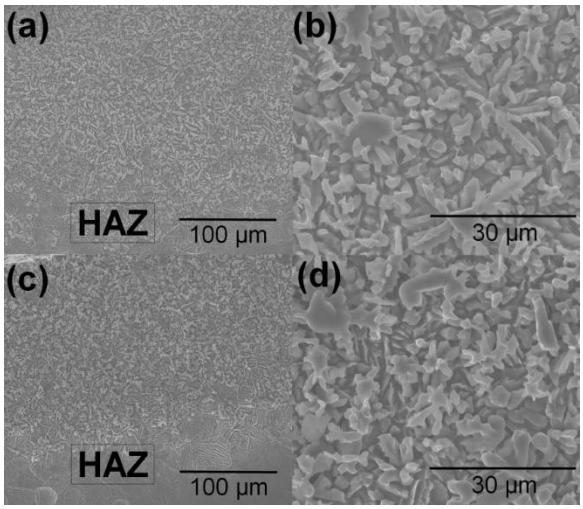

Figure 4.25 Cross-sectional SEM micrographs of USV-LSM Ti-6Al-4V samples: Low magnification microstructure exhibiting uniform equiaxed grains throughout melt zone in (a) 25%, and (b) 30% USV-LSM alloys, higher magnification microstructures exhibiting grain morphology in (c) 25%, and (d) 30% USV-LSM alloys

4.5.2 Microhardness Characterization

The variation of microhardness in the depth of laser surface melted Ti-6Al-4V samples is presented in Figure 4.26. The average microhardness of starting Ti-6Al-4V sample was about 180±5 HV. The hardness was unaffected up to the depth of about 300 µm for the sample laser melted without the application of ultrasonic vibrations. However, a marked increase (about two fold increase) in surface hardness was observed for samples laser surface melted under the influence of ultrasonic vibrations. The surface hardness of 470±14 and 486±10 was observed for the ultrasonic power outputs of 25% and 30%, respectively. The martensitic phase transformation upon solidification (L→β→α') in Ti-alloys is not associated with significant strengthening. Based on microstructural characterization, the improvement in the surface microhardness seems to be the direct result of grain refinement due to the application of ultrasonic vibrations. It should be noted that the samples laser surface melted without ultrasonic vibrations exhibited maximum hardness (350±8 HV) at a depth of 450 µm from the surface. Note that fine dendritic grains were observed for these samples only near the fusion zone (region C). The hardness values are similar to those

exhibited by samples laser surface melted under the influence of ultrasonic vibrations at the depth of 150 µm. This observation is also consistent with the explanation of improvement in surface hardness due to grain refinement.

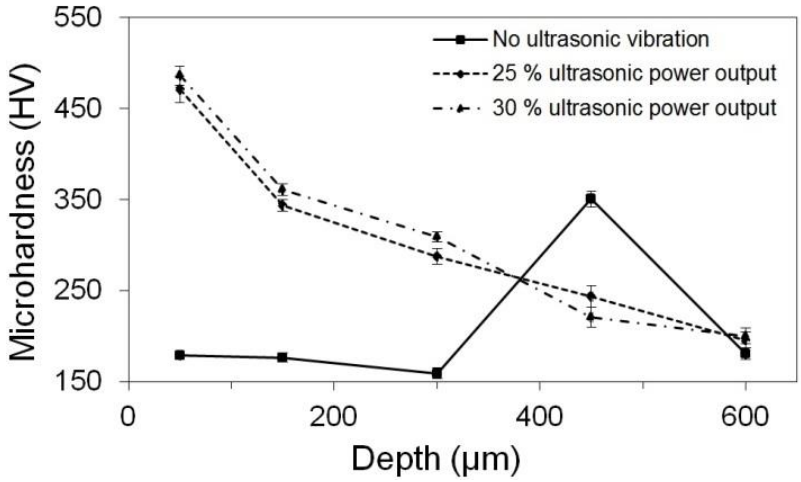

Figure 4.26 Microhardness of the laser surface melted samples with and without the application of ultrasonic vibrations.

4.6 Ultrasonic Vibration-Assisted Laser Surface Melting and Texturing of Biomedical Grade Titanium Alloy (Ti-6Al-4V ELI)

This section is reproduced from the publication "Effect of Ultrasonic Vibration-Assisted Laser Surface Melting and Texturing of Ti-6Al-4V ELI Alloy on Surface Properties" that has been accepted by the Journal of Materials Science and Technology in which the student is also the first author. The study on effect of ultrasonic vibrations on laser melting of Ti-6Al-4V alloy clearly demonstrated remarkable grain refinement, improvement in strength, and partial expulsion of the melt. Clearly, the hardening associated with ultrasonic vibration-assisted laser surface melting can be potentially extended in larger area processed substrates with similar effects. Furthermore, the turbulence associated ultrasonic vibrations (that caused the partial melt expulsion) can also be used to develop unique texture of the surface. Indeed, the texturing associated with ultrasonic vibrations have been reported to be highly successful in improving tribological properties of titanium alloys,

particularly for biomedical applications [81, 82]. It should be noted that laser texturing is almost exclusively performed using pulsed laser (with pulses ranging in the order of 10^{-9} to 10^{-15} s). This predominance is primarily due to the high instantaneous power densities associated with pulsed lasers that readily promote ablation of the substrate. However, the majority of industrial lasers are primarily continuous wave lasers that can only generate melting (but no ablation) of the melt. Hence in this study the major motivation was to use the melt turbulence associated with ultrasonic vibrations can be used to develop a controlled textured surface as well as utilize the surface hardening associated with laser melting to improve the wear resistance of biomedical grade Ti-6Al-4V ELI alloys. The tribological behavior of the textured substrates were evaluated by conducting laser surface texturing experiments in simulated body fluids (Hank's solution). The samples used were procured as extra low interstitial (ELI) Ti-6Al-4V rod (M. Vincent and Associates, Minneapolis, MN), machined to flat head screws (φ = 1.5"), and then polished with 1200 grit size polishing paper to remove surface irregularities. The details on the processing parameters used in the investigation is provided in Table 4.6.

Table 4.6 Summary of laser processing parameters for laser surface melting and texturing experiments of Ti-6Al-4V ELI alloy with and without simultaneous application of vertical ultrasonic vibrations to the substrate

Sample ID	Beam Velocity (mm/s)	Laser Power (W)	USV Amp (%)
AR	-	-	-
LM	20	950	-
ULM30	20	950	30
ULM40	20	950	40

4.6.1 Surface Profile Characterization

Figure 4.27 presents the surface SEM images and surface profiles of the as-received (AR), laser melted (LM), and ultrasonic vibration-assisted laser textured (ULM30 and ULM40) Ti-6Al-4V specimens. The surface roughness (R_z) of the AR samples was observed to be about 13.87 µm (Figure 4.27(a)). Also, the surface exhibited several peaks and valleys with the overall surface profile (mean of the peaks) being relatively horizontal. The laser melting operation without the application of ultrasonic vibrations to the substrate (LM) was observed to further reduce the surface roughness ($R_z \approx 6.64$ µm). While the laser processing resulted in decrease in surface roughness, the surface exhibited repeating undulations, presented in Figure 4.27(b). The reduction in surface roughness in the LM specimens was attributed to the use of controlled processing parameters that effectively melted the surface peaks and redistributed the melt on the surface, causing surface smoothing. Also, it can be clearly observed that laser melting with the application of ultrasonic vibrations to the substrates (ULM30 and ULM40) resulted in significant increases in surface roughness of the samples, with the roughness (R_z) measured to be about 44.00 and 47.07 µm for ULM30 and ULM40 samples, respectively (Figure 4.27(c-d)). The extensive melt agitations due to the application of ultrasonic vibrations to the substrates resulted in significant increase in vertical flow of the melt during laser scanning, forming a deep groove along the laser track. The overlapping of parallel laser tracks then creates a repeating undulating 'wavy' surface. Of course, small change in the dimensions of the grooves is a result of local melt dynamics and heat accumulation effects, especially for relatively low conductivity titanium alloys. The higher ultrasonic power output is also correlated with the higher amplitude of vertical vibrations. ULM40 specimens exhibited higher surface roughness and deeper undulations compared to ULM30 due to enhanced melt flow under the influence of ultrasonic vibrations of higher amplitude. Further optimization of processing parameters, including laser parameters (power, scanning speed, and track overlap) and ultrasonic vibration parameters (vibration frequency and amplitude), is needed to further improve the

repeatability of the dimensions of the surface features. It should be noted that the development of such undulating surfaces, accompanied by the increase in surface roughness, has been reported to be highly effective in increasing protein adhesion on implant [83]. Therefore, ultrasonic vibration-assisted laser texturing of the biomedical materials appears to be a highly promising technique to improve protein adhesion in implant surfaces.

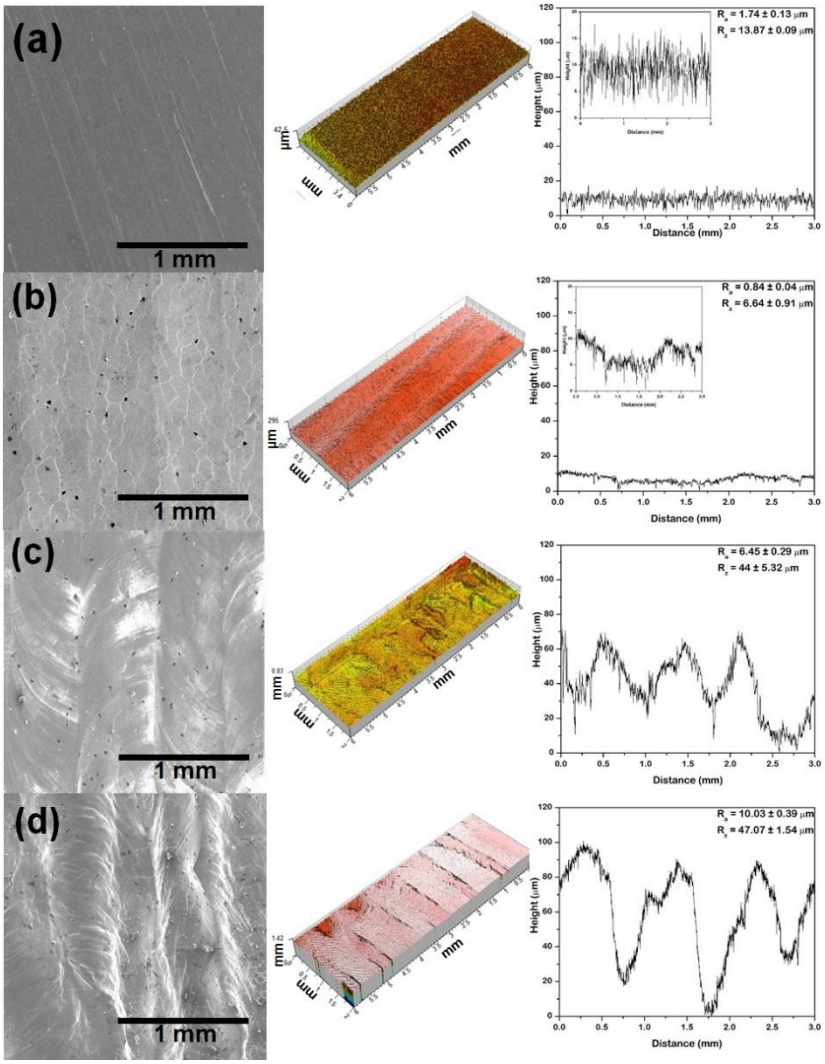

Figure 4.27 Low magnification surface micrographs and corresponding three-dimensional and 2-dimensional surface profiles for (a) AR, (b) LM, (c) ULM30, and (d) ULM40 specimens. The insets in (a) and (b) show magnified two-dimensional surface profiles.

4.6.2 XRD Analysis

The XRD patterns from AR and LM specimens indicate that the surface microstructure completely comprised of the HCP α/α' phase, with the patterns exhibiting all the major characteristic peaks of α/α' with no indication of the BCC β phase (Figure 4.28). Comparatively, the XRD patterns from ULM30 and ULM40 indicate the presence of traces of β phase. It can be clearly observed that the AR specimens exhibited a mildly textured surface, with the dominance of (100) and (101) planes. Since AR specimens were procured in rod form that is mainly manufactured by rolling or extrusion, crystallographic texturing was quite expected. Although the Ti-6Al-4V alloy is an α/β-Ti alloy, in equilibrium conditions the alloy primarily exhibits globular α at room temperature [84]. It has been established that the onset of β → α transformation in Ti-6Al-4V ELI alloys occurs at about 975 °C, and temperature for the completion of transformation decreases with increasing cooling rate [85]. Several investigations have reported that ultrasonic vibrations can significantly influence the heat transfer both in solid and liquid media. The ultrasonic vibrations induce acoustic streaming and cavitation enhancing the heat transfer in the liquid media [86, 87]. It has also been observed that the application of simultaneous ultrasonic vibrations also enhances the convective heat transfer from the surface [88]. These effects have been demonstrated for the conditions involving laser irradiation of the vibrating surfaces. It appears that these heat transfer enhancement effects associated with the application of ultrasonic vibrations results in higher cooling rates in ULM30 and ULM40 specimens. Since higher cooling rates favor β to martensitic α' as observed in the microstructural analysis, it results in rejection of the solutes from the martensitic α’ to the β phase and retaining traces of β phase in the microstructure [89].

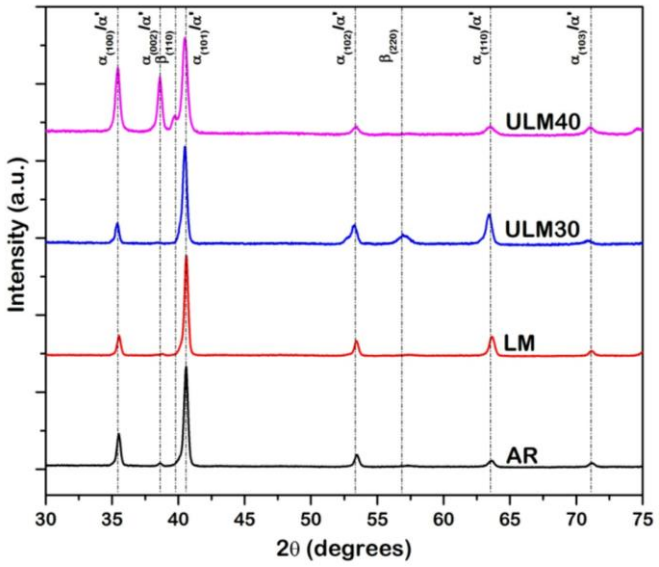

Figure 4.28 XRD patterns of AR, LM, ULM30, and ULM40 specimens

4.6.3 Microstructural Characterization

The low magnification cross-sectional micrographs of the laser processed samples (LM, ULM30 and ULM40) are presented in Figure 4.29. As can be observed, all the samples exhibited a very well defined melt zone with average melt depth of 458, 528, and 443 µm for LM, ULM30, and ULM40 samples, respectively. The physical surface morphological textures formed on ULM30 and ULM40 specimens is primarily due to flow of melt pool under the influence of ultrasonic vibrations applied to the surface. Figure 4.30 presents the higher magnification microstructures of the AR and melt zones of the laser processed samples in the cross sections. It can be observed that the microstructure of AR samples exhibited typical features of annealed Ti-6Al-4V alloy, consisting of primary globular α grains. It also indicated mild crystallographic texture as obviously expected from rods processed by hot-extrusion methods wherein grains tend to align along the working direction [85], an observation also reflected in the XRD measurements. The microstructures of the laser treated samples, as presented in Figure 4.30 (b-d) exhibited significant transformation of the primary α grains to acicular α-needles and α' martensite [90]. The acicular α phases nucleated from the prior β grain boundaries, while the grain interiors were comprised

predominantly of α' martensite in each laser processed sample. The formation of acicular α and martensitic α' was also observed in the microstructural evolution of Ti-6Al-4V samples with cooling rate studies in the higher cooling rate samples (525 $°Cs^{-1}$) by Ahmed *et al* [91]. Hence, the observation of α and α' phases is obviously a consequence of the laser processing that causes enhanced cooling rates (of the order of 10^4 $°Cs^{-1}$). Also, the acicular α needles were observed to grow parallel to the direction of conductive heat transfer, and was very similar to the observations of selective laser melted titanium substrates (that also experienced similar rapid quenching) by Thijs *et al* [92].

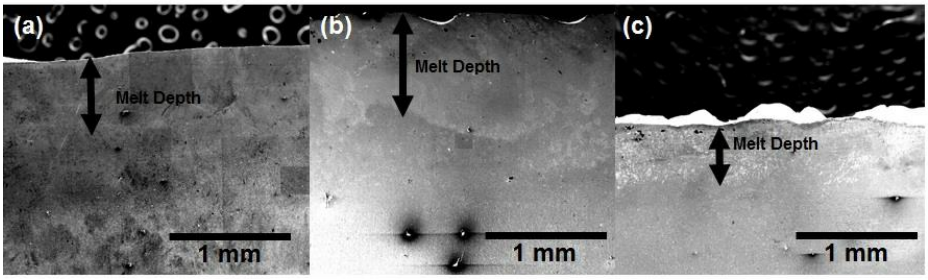

Figure 4.29 Low magnification cross-sectional micrographs of (a) LM, (b) ULM30, and (c) ULM40 samples.

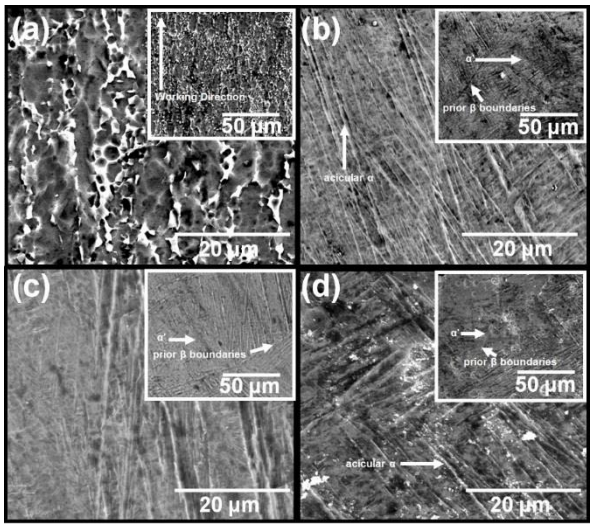

Figure 4.30 Microstructures of (a) AR, (b) LM, (c) ULM30, and (d) ULM40 samples; the lower magnification microstructures are provided in the insets

4.6.4 Surface Wettability Characterization

Contact angle measurements were performed to understand the variation in surface wettability of the laser processed samples compared to the AR samples. These results are presented in Figure 4.31. It can be clearly observed that the AR samples exhibited a more wettable (hydrophilic) surface with an average contact angle of about 67°. Comparatively, the LM sample exhibited significant decrease in wettability (becoming more hydrophobic) as evident from the increase in contact angle to 91°. As noted in the surface profile discussion, the LM sample exhibited an undulating 'wavy' surface with lower overall surface roughness ($R_z \approx 6.64$ μm) compared to the AR samples ($R_z \approx 13.87$ μm). It appears that the higher surface roughness increases the total available surface area, thereby increasing the wettability, a common observation with hydrophilic surfaces [93]. The direct relationship of surface roughness with surface wettability was further reflected in the ULM30 ($R_z \approx 44$ μm) and ULM40 ($R_z \approx 47.07$ μm) samples, which exhibited progressive increases in wettability (contact angles 75° and 86° for ULM30 and ULM40, respectively) compared to the LM samples. However, it should be noted that the AR substrates exhibited higher wettability compared to all of the laser treated samples, although the surface roughness of AR was significantly lower compared to ULM30 and ULM40 samples. Hence, it appears that the laser processing most likely influenced the surface chemical composition that subsequently affected the wettability of the surface. Indeed, the effect of surface chemical compositional changes on the wettability has been elucidated in several investigations [94, 95]. It has been reported that while extreme hydrophobicity often acts as poor cell culture substrate [83], highly hydrophilic surfaces are often prone to pitting corrosion [96]. Hence, our future efforts will be directed towards investigation of effect of processing parameters on surface textures in ultrasonic vibration-assisted laser texturing such that specific predetermined combination of surface roughness and hydrophobicity can be successfully achieved.

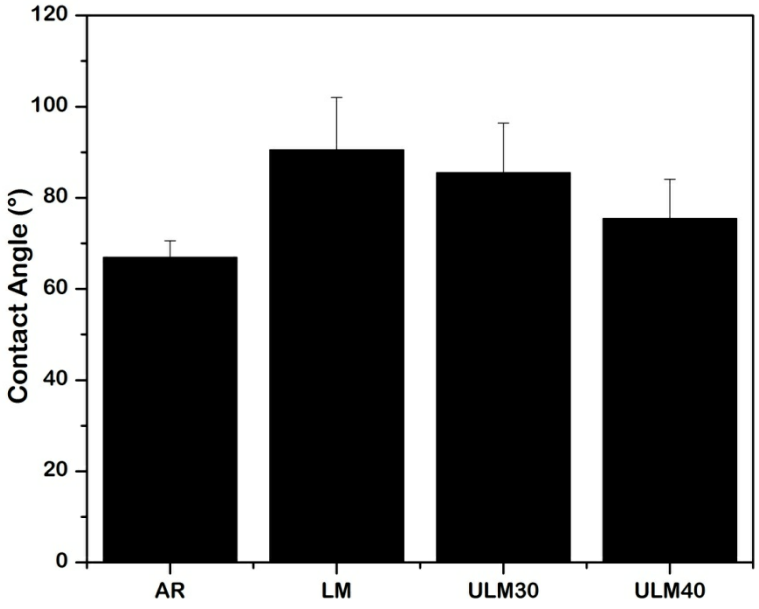

Figure 4.31 Contact angles of water droplets for AR, LM, ULM30, and ULM40

4.6.5 Microhardness Characterization

The laser processing, as discussed previously, was not only successful in developing surface texture, but also resulted in significant changes in microstructure. Hence, microhardness characterization was performed to determine the effect of the microstructural changes on the mechanical properties in the textured and remelted region. The variation of microhardness with depth from the surface of the AR and laser processed (LM, ULM30, and ULM40) samples is presented in Figure 4.32. The AR specimen exhibited an average hardness of about 327 HV, very similar to the hardness reported for globular α-rich Ti-6Al-4V alloy [97]. The LM samples exhibited a mild increase in hardness to 359 HV. Both the ULM30 and ULM40 samples exhibited higher surface hardness. The hardness of ULM30 and ULM40 samples at a depth of 50 μm was about 376 HV and 381 HV, respectively. It should be noted that the hardness values corresponds very well with the selective laser melted Ti-6Al-4V substrates (that also exhibited very similar acicular α-phase dominated microstructure) reported by Thijs *et al* [92]. Obviously, the increased grain refinement (acicular α being much refined than globular α) as well as increased presence of

traces of β phases (reflected in the XRD measurements, in ULM30 and ULM40 samples primarily contributed to the increase in hardness [98].

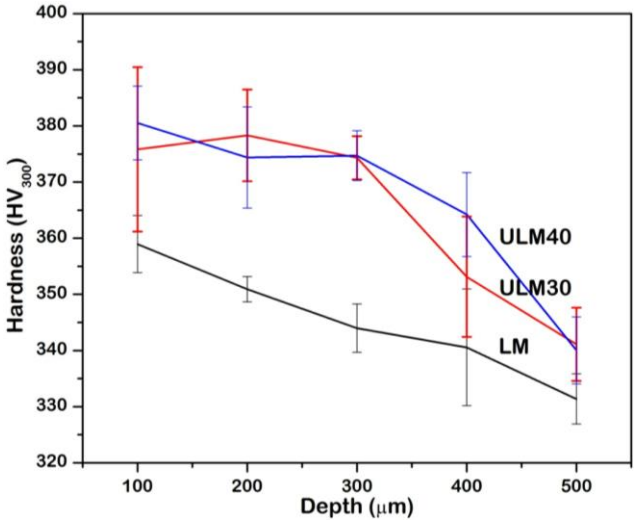

Figure 4.32 Hardness variation with depth for LM, ULM30, and ULM40 samples.

4.6.6 Wear Characterization

The pin-on-disc wear tests were performed in simulated body fluid to quantitatively analyze the effect of the surface texture as well as the improved hardness on the tribological properties. The variations of coefficient of friction (COF) during wear tests for AR and laser processed (LM, ULM30 and ULM40) samples are presented in Figure 4.33. As can be observed, the COF remains stable about mean value for each sample, indicating that the lubrication effect from the simulated body fluid was relatively same during the entire experimentation time. The mean COF was lowest for the LM sample (0.173), followed by the AR (0.359), ULM40 (0.231), and ULM30 (0.311) samples. It should be noted that the wear is a very complex process, and is dependent of several other factors such as texture, environment, surface mechanical properties, and others. In the present investigation, the processing conditions resulted in variation of primarily surface texture and surface hardness, while other factors were kept virtually unchanged. Therefore, the wear behavior should likely be influenced by the aforementioned factors. Now, a striking

feature observable in the mean COF of the samples is that although the AR sample ($R_z \approx 13.87$ μm) exhibited considerably less surface roughness compared to the ULM30 ($R_z \approx 44$ μm) and ULM40 samples ($R_z \approx 47.07$ μm), the mean COF exhibited a reverse trend. This can be attributed to the significant retainment of lubricant within the textured grooves in the ULM30 and ULM40 samples that considerably increased surface lubrication. The samples with the smallest mean COF (LM) were most likely smaller due to the smoother ($R_z \approx 6.64$ μm) but undulating textured surfaces. These surfaces possibly resulted in an optimum combination of smooth, but lubricant retaining interface. Hence, it can be surmised that the laser texturing, both with and without the influence of ultrasonic vibrations, resulted in increased lubrication of the surface. Table 4.7 presents the wear rate and mean coefficient of friction of the as received and laser processed samples. Clearly, the wears rate were smaller in each of the laser processed samples (AR exhibiting 4.4 μg $N^{-1}m^{-1}$ compared to 1.2-2.4 μg $N^{-1}m^{-1}$ in laser processed samples). Furthermore, a consistent decrease in wear rates was noted with increase in ultrasonic vibration amplitude. The increased wear resistance can be directly associated with the increased surface hardness (particularly in comparison of the AR with LM, ULM30, ULM40), reduction in surface contact due to textured (grooved) surface as well as increased lubrication in the laser processed samples compared to the AR samples.

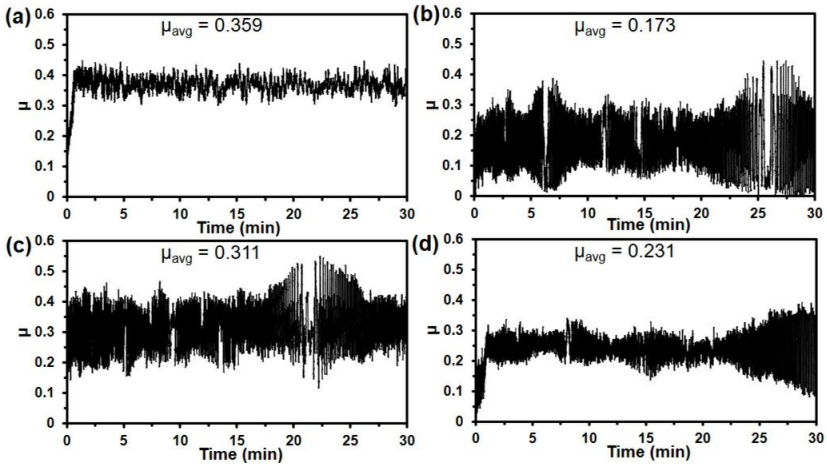

Figure 4.33 Variation of the coefficient of friction (μ), with time for (a) AR, (b) LM, (c) ULM30, and (d) ULM40 samples

Table 4.7 Wear rate and mean coefficient of friction (COF) in as received and laser processed samples

Specimens	Wear Rate (μg $N^{-1}m^{-1}$)	Mean COF
AR	4.4	0.359
LM	2.4	0.173
ULM30	2	0.311
ULM40	1.4	0.231

Since material loss due to wear is an almost exclusively abrasive wear phenomenon, the results clearly indicate that ultrasonic vibration-assisted laser processing improved wear resistance, with the wear improvement increasing with increasing ultrasonic vibration amplitude. The wear mechanism was further studied by imaging of the wear scars. The scanning electron micrographs of the wear scars are presented in Figure 4.34. The wear scars on the AR samples (Figure 4.34(a)), show primarily grooves characteristic of microcutting and ploughing mechanism in abrasive wear [99] with small regions of plastically deformed patches. The grooves were observed to be less pronounced in the laser processed samples, indicating reduction in abrasive wear that was also observed in the wear rate (4.4 μg $N^{-1}m^{-1}$ for AR compared to 1.2-2.4 μg $N^{-1}m^{-1}$) in laser processed samples. In comparison, the wear scars of the laser processed samples exhibited plastically deformed patches as well as grooves. The plastically deformed patches formed in the LM samples were much better defined (Figure 4.34(b)) compared to the AR counterparts (Figure 4.34(a)). The plastically deformed patches form due to *in-situ* cold welding and subsequent deformation of the surface of the substrate, a typical characteristic of adhesive wear [100]. Also, the wear scars in the ULM30 (Figure 4.34 (c)) and ULM40 (Figure 4.34 (d)) samples revealed unworn regions indicating that the textured surface of the laser processed samples, especially with ultrasonic vibrations.

Clearly, the laser texturing was highly effective in reducing surface contact, and hence decreasing overall available material to undergo abrasion.

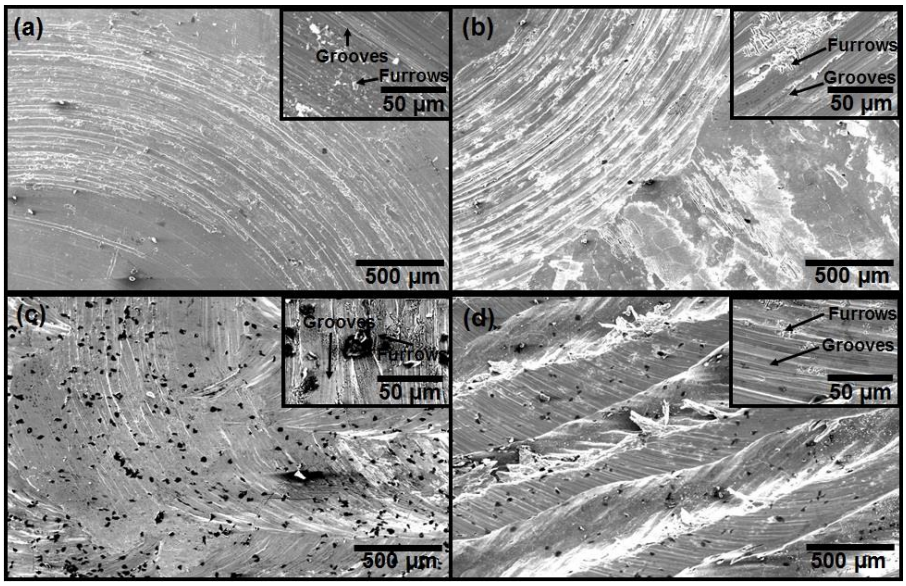

Figure 4.34 SEM micrographs of wear scars of (a) AR, (b) LM, (c) ULM30, and (d) ULM40 samples

4.7 Ultrasonic Vibration-Assisted Laser Surface Texturing of Stainless Steel

Laser surface texturing, as described previously, has been almost exclusively attempted with pulsed lasers (with pulses ranging from 10^{-9} to 10^{-15} s) due to significantly high power densities associated with pulses lasers that can generate ablation of the substrate. Furthermore, development of textured dimpled surfaces in the melting regime is further restricted due to the limited applicability of generating deeper dimpled substrates. Naturally, the melt agitations associated with ultrasonic vibrations, in optimized conditions, can be potentially highly efficient in developing deeper dimples. Now, in lubricated wear, the dimples have been reported to act as debris cache, lubricant retaining sites and thereby result in improvement of surface tribological performance. Hence in this investigation ultrasonic vibration-assisted laser surface texturing was used to develop a textured dimpled surface and the tribological performance of the textured surface upon addition

of suspension of graphene and ethanol was studied and compared to unlubricated and non-textured counterparts. Graphene has attracted significant interest in the past few decades due to its unique mechanical and electrochemical properties. In particular, graphene reduces friction and wear loss in structural materials. The material was selected to be stainless steel as steel-on-steel sliding often generates significantly high coefficient of friction that in turn generates extensive adhesive wear. Table 4.8 presents the key processing conditions employed to conduct the ultrasonic vibration-assisted laser surface texturing experiments with ARD and ARL being the sample ID of as-received without and with lubrication.

Table 4.8 Processing conditions used for laser surface texturing of stainless steel with and without simultaneous application of vertical ultrasonic vibrations to the substrate

Sample ID	Textured Area	On/Off time	Scanning Speed	Power
U0	12 mm × 12 mm	1ms/20 ms	20 mm/s	900-950W
U20	12 mm × 12 mm	1 ms/20 ms	20 mm/s	900-950W
U30	12 mm × 12 mm	1 ms/20 ms	20 mm/s	900-950W
U40	12 mm × 12 mm	1 ms/20 ms	20 mm/s	900-950W

The substrates used for laser surface texturing were procured from McMaster Carr as flat hexagonal head 316 stainless steel screws (head thickness = ¼″ and length = ½″, sample ID: 93190A707). The screws were annealed at 950°C to remove the internal strains generated during their processing and were then polished carefully with 1200 grit size paper to remove surface irregularities. The screws were then sandblasted to improve the laser absorptivity of the surface and were subsequently cleaned with deionized water and acetone to eliminate inorganic and organic impurities respectively from the surface.

4.7.1 Surface Profile Characterization

Figure 4.35 presents the transmission electron micrographs of the graphene flakes (dried on a copper grid) and the surface micrographs of the textured surfaces with and without simultaneous application of ultrasonic vibrations. The graphene flakes were observed to be about 100 nm width and were highly agglomerated, due to the evaporation of alcohol dispersion medium, as can be observed from Figure 4.35(a). The laser surface texturing, both with and without simultaneous influence of ultrasonic vibrations was observed to result in circular dimples with diameter of about 0.72 ± 1.4 mm. Also, the distance of separation between the centers was about 0.5 mm as presented in Figure 4.35(b-e). This is clearly associated with the shift (along the Y-direction) provided during the laser surface texturing. The volumetric (three-dimensional) and cross-sectional (two-dimensional) surface profiles of the laser surface textured steel specimens are presented in Figure 4.36.

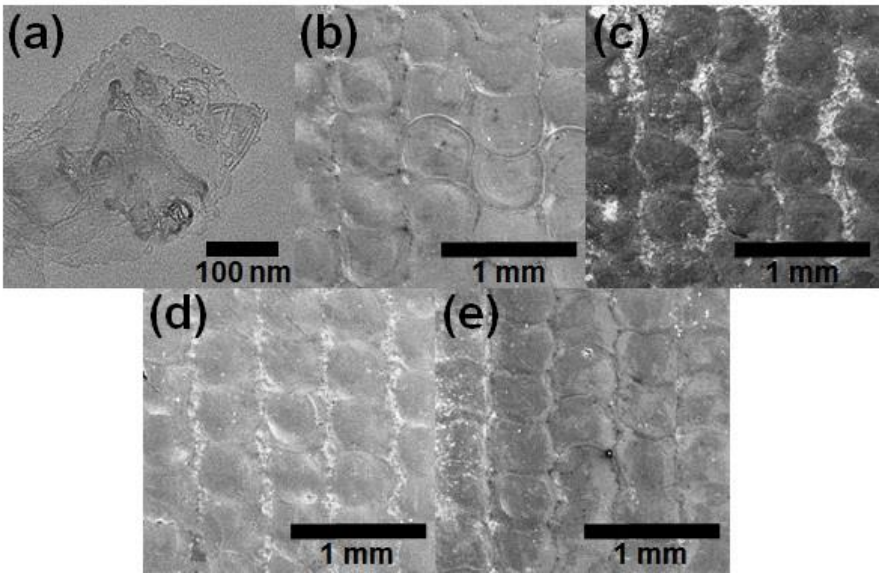

Figure 4.35 (a) TEM micrographs of graphene flakes and low magnification SEM micrographs of textured surface of (b) U0, (c) U20, (d) U30, and (e) U40 specimen respectively

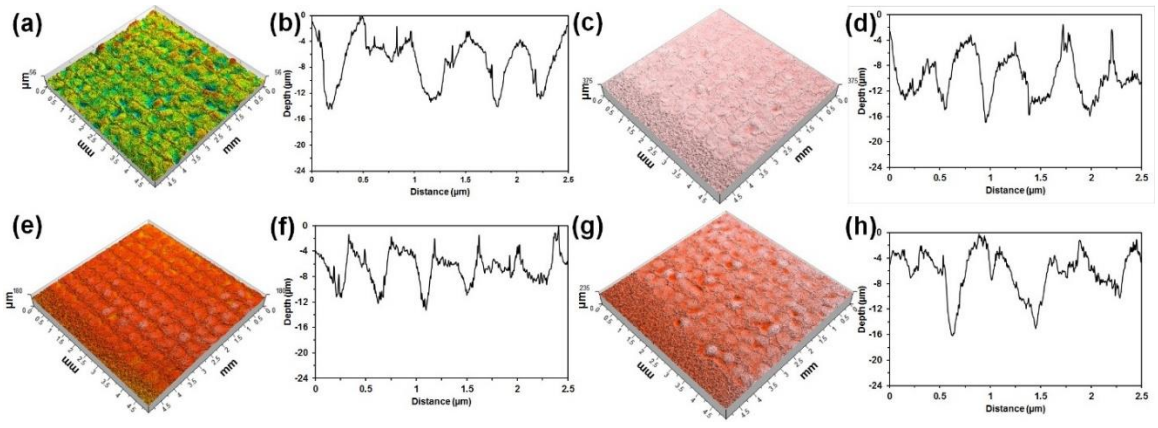

Figure 4.36 3D optical profiles and corresponding line profiles of (a-b) U0, (c-d) U20, (e-f) U30, and (g-h) U40 specimen respectively

It can be clearly observed that the laser surface texturing resulting in periodic, repeating dimples, also observed in the topographic micrographs. The dimples exhibited conical morphology, as reflected in the cross-sectional surface profiles, in the laser textured samples both with and without the influence of ultrasonic vibrations. The conical profile is due to the Gaussian energy distribution of the beam that resulted in consistent increase in melting from the edge to the center of the laser irradiated region. Also, the depths of the dimples were observed to increase with increase in ultrasonic vibrations amplitude, with the U0, U20, U30, and U40 samples exhibiting an average dimple depth of about 13.1 ± 2.7 µm, 16.4 ± 2.2 µm, 15.1 ± 1.7 µm, and 18.4 ± 1.8 µm respectively. Clearly, the extensive melt turbulence due to the ultrasonic vibrations experienced by the laser-irradiated melt film resulted in increased upward motion of the melt film, thereby increasing the dimple depth. The increased dimple depth was also reflected in the surface roughness values that also displayed monotonous increase with increase in ultrasonic vibration amplitude, with the R_z values being 2.23 ± 0.79 µm, 10.67 ± 0.13 µm, 11.1 ± 1.01 µm, 12.03 ± 0.79 µm, and 12.63 ± 1.39 µm for as-received, U0, U20, U30, and U40 samples respectively. Hence, a progressive increase in dimple depth and volume was achieved by systematic increase in ultrasonic vibration amplitude during the laser surface texturing experiments.

4.7.2 Wear Characterization

The variation of coefficient of friction with time in the as-received samples with (ARL) and without (ARD) addition of graphene, as well as the laser surface textured samples (with and without simultaneous application of ultrasonic vibrations) with addition of graphene is presented in Figure 4.37. The coefficient of friction in ARD samples was observed to be about 0.23 at the onset of the experimentation but very quickly escalated to about 0.87, as presented in Figure 4.37(a). The coefficient of friction exhibited by the ARD samples is consistent with similar literature that has investigated steel-on-steel wear [101, 102]. The wear experiments with addition of graphene resulted in nearly six-fold decrease in coefficient of friction, especially until about 1800 revolutions, as can be observed from Figure 4.37(b). However, as highlighted in the inset of Figure 4.37(b), the coefficient of friction was observed to increase after about 1800 revolutions. This clearly indicates that the lubricating effect of the graphene deteriorated with time, possibly due to mechanical and/or chemical degradation of graphene. This aggravation was observed to recur after about 3900 and 5700 revolutions, corresponding to 1900 and 1700 after addition of graphene for the second and third time respectively. Furthermore, the magnitude of the escalation was also observed to exacerbate with time, as indicated by the coefficient of friction values at 2000, 4000, and 6000 (just before addition of graphene) revolutions being about 0.17, 0.18, and 0.37 respectively. Naturally, as the roughness of the wear tracks increased with increase in revolutions, the deterioration of graphene also progressively increased. However, the laser textured samples not only exhibited marked improvement in coefficient of friction similar to the ARL samples, but also strongly implied that the decrease in coefficient of friction was sustained over time, as presented in Figure 4.37(c-f). Also, the coefficient of friction was observed to further decrease with increase in dimple depth, as indicated by the average coefficient of friction to be 0.114, 0.034, 0.048, and 0.01 for U0, U20, U30, and U40 samples respectively.

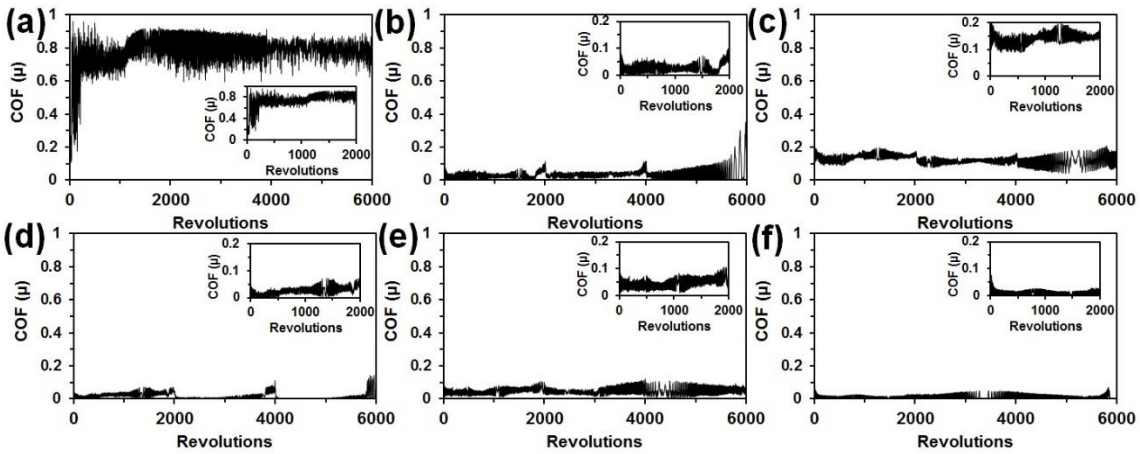

Figure 4.37 Variation of coefficient of friction with revolutions of (a) ARD, (b) ARL, (c) U0, (d) U20, (e) U30, and (f) U40 specimen respectively (the variation of coefficient of friction at the initial stages are provided in the inset)

Possibly, the higher melt depth achieved by increased melt turbulence due to the ultrasonic vibrations increased the volume of the dimples and subsequently that of the stored graphene. The efficiency of the dimples in storing graphene as well as its mechano-chemical transformations were hence studied using Raman spectroscopy. The wear scars on the ARD samples, presented in Figure 4.38(a), exhibited significant surface damage as can be observed from the extensive plastic deformation. It should be noted that contacting surfaces exhibiting relatively high coefficient of friction (greater than 0.7) are almost always accompanied by plastic deformation [103]. It has been reported that this plastic deformation is primarily due to the high friction between the contacting surface generate significant shear stresses at the surface and local cold welding that in turn plastically deform the surface, a characteristic of adhesive wear [104].

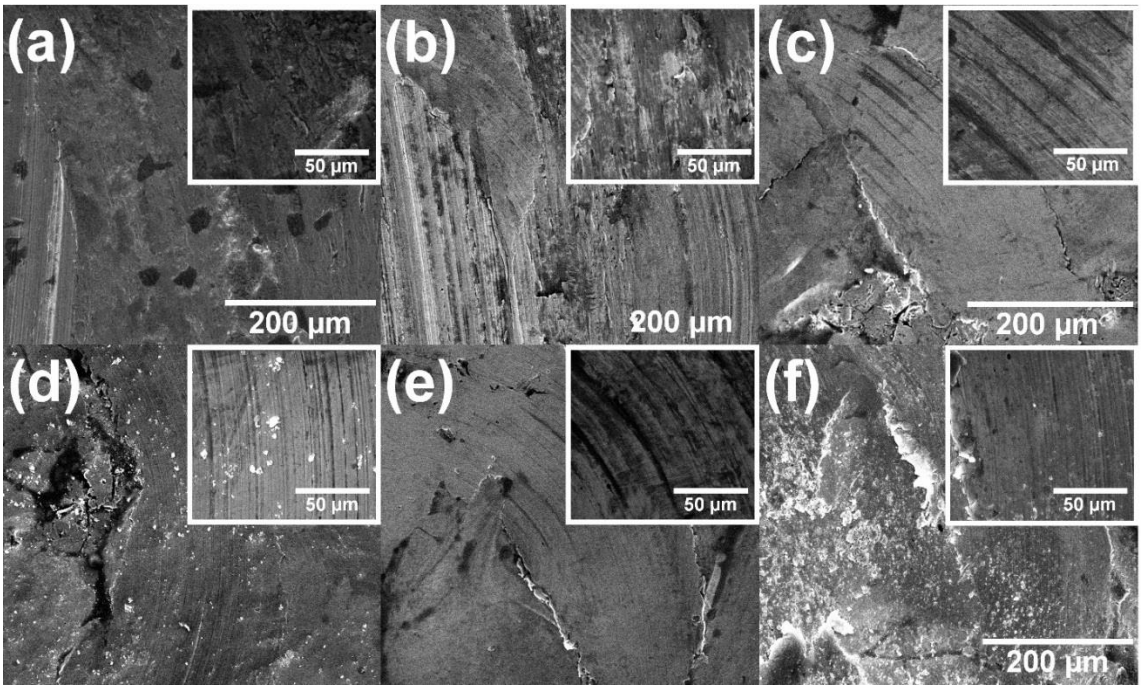

Figure 4.38 SEM micrographs of wear tracks of (a) ARD, (b) ARL, (c) U0, (d) U20, (e) U30, and (f) U40 specimen respectively (the higher magnification micrograph has been provided in the inset)

However, the wear scars on the graphene added samples revealed marked improvement in surface quality, with the plastically deformed patches being almost non-existant (Figure 4.38(b-f)). Obviously, the reduction in plastic damage can be associated with the improved lubrication provided by the graphene (presented in Figure 4.38(b-f)). Also, the wear scars exhibited presence of grooves, a characteristic of the microcutting mechanism associated with abrasive wear, and was most likely formed in the initial revolutions (prior to formation of well-developed wear track) when the Hertzian load was high.

4.7.3 Raman Characterization

Figure 4.39(a) shows the Raman spectrum of graphene after coated on a cleaned nickel coin (5 US cents) from the as-received suspension by multiple drop-and-dry steps. The peaks at 1351, 1582, and 2717 cm^{-1} are characteristic of graphite/graphene and referred as the D, G and 2D bands [105, 106]. The D+D′′ and 2D′ bands are also observed at 2447 and 3305 cm^{-1}, respectively

[107]. While the 2D band is located at 2680 cm^{-1} for single-layer graphene, the 37 cm^{-1} upshift, seen here, is attributed to the stacking of graphene layers during solvent drying, wherein the coated layer approaches a graphitic structure [105, 108]. Figure 4.39(b) shows Raman spectrum of as-received substrate surface without graphene exposure (ARD) and prior to wear. Two different iron oxides are detected on the surface. The peaks at 215, 281 and 595 cm^{-1} are assigned to α-Fe_2O_3, while the peaks at 391 and 1280 cm^{-1} are assigned to α-FeOOH [109-111]. Because Raman spectroscopy was conducted few weeks after sample preparation (i.e., polishing), detectable amount of native oxide must have formed on the sample surfaces within this duration. Additionally, Figure 4.39(c) and (d) show representative Raman spectra of ARL (as-received substrate) and U40 after wear with graphene lubrication. Herein, we only present the after-wear spectra for ARL and U40, since these two samples represent the highest and lowest degree of degradation/damage for graphene during wear.

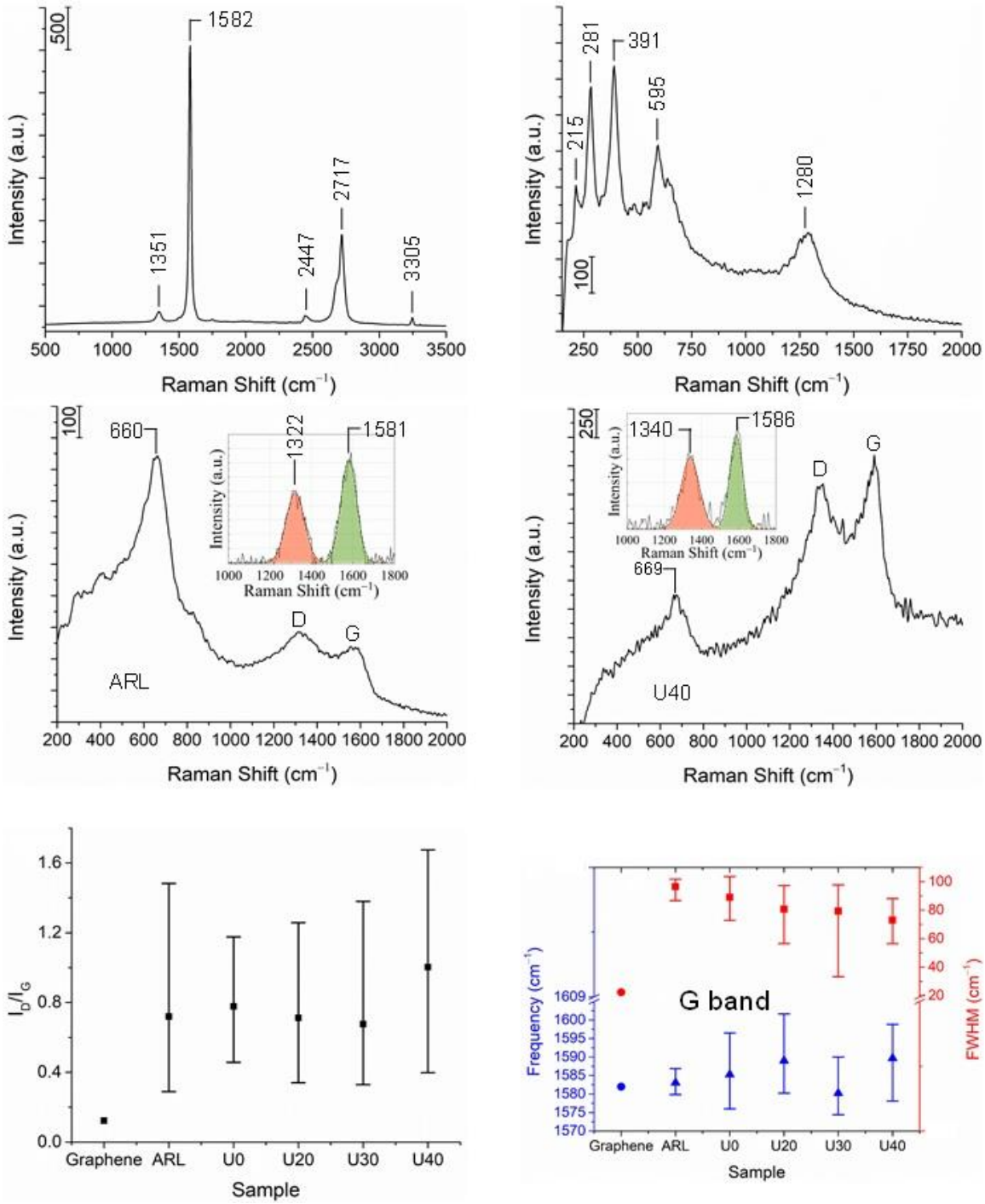

Figure 4.39 (a) Raman spectrum of as-received graphene. (b) Raman spectrum of as-received substrate surface. Representative Raman spectra of deteriorated graphene of ARL (c) and U40 (d). (e) Average I_D/I_G with error bars. (f) Average peak position (blue) and FWHM (red) of the G band with error bars

Given U40 has the highest dimple depth, it has the largest volume of lubricant reservoir, where damage per graphene flake is expected to be the minimum. In contrast, ARL has no engineered lubricant reservoirs.While the α-Fe_2O_3 and α-FeOOH peaks are not detectable after wear, likely due to polishing action of friction, two similar Raman peaks at 660 and 669 cm^{-1} are observed for ARL and U40, respectively. Those peaks are assigned to Fe_3O_4 [112], which we owe to thermal oxidation of Fe during wear (i.e., through friction-induced heat generation). Additionally, the deconvoluted D and G bands are shown in the insets after background subtraction and peak fitting. The D-to-G band intensity ratio (I_D/I_G) is commonly adopted as a measure of disorder in graphene [113]. Figures 4.39(c) and (d) indicate a remarkable increase of I_D/I_G after wear from its as-received value (Figure 4.39(e)). Hence, significant level of graphene degradation due to wear is inferred. However, variation of I_D/I_G with disorder is not monotonous if the increase of disorder is prolonged. As such, I_D/I_G is lower for ARL than U40, although these two samples are associated with the highest and lowest graphene damage, respectively. It is clearly established in the graphite/graphene Raman literature, that I_D/I_G increases with disorder first (Regime 1), up to a critical degree of disorder, beyond which it falls (Regime 2). This crossover from the rising regime to falling one, marks the onset of amorphization, during which crystalline sp^2 carbon is replaced by disordered sp^3 carbon. Therefore, the graphene of ARL must be in Regime 2 and have partially amorphized, while graphene of U40 is either in a late stage of Regime 1 or earlier stage of Regime 2. I_D/I_G of the remaining after-wear samples are also included in Figure 4.39 (e). We observe I_D/I_G is the highest for U40. Therefore, we conclude the graphene associated with U0, U20, and U30 is also in Regime 2 and partially amorphized. Accordingly, significant degradation of the graphene lubricant by the end of the wear test is inferred. This finding agrees with continuous increase of the friction coefficient, where extended amorphization of graphene (and conversion from sp^2 to sp^3 carbon) results in loss of its lubrication properties.

Based on both averages and the error band in Figure 4.39(e), we observe a trend of decreasing I_D/I_G in the direction from U40 towards ARL, indicative of increasing fraction of amorphous carbon. This trend is matched by lower wavenumber shift of the G band in Figure 4.39(f), which also suggests formation of amorphous carbon, based on the well-established amorphization trajectory by Ferrari *et al*.[113]. Also, the systematic broadening of the G band (FWHM) in Figure 4.39 (e) collaborates the increase of disorder in the direction from U40 to ARL [114]. Clearly, the error bars (based on 11 measurements) in Figure 4.39(e) and (f) indicate significant heterogeneity of graphene (i.e., in terms of degree of disorder due to deterioration) after wear. For the best representation, spectra in Figure 4.39 (c) and (d) were selected from samples, being closest to the average.

CHAPTER V

CONCLUSIONS

Ultrasonic vibration-assisted laser surface engineering of structural alloys was successfully performed in this investigation. This study was primarily focused towards understanding the efficiency of ultrasonic vibrations in reducing textured, dendritic microstructure and establishing the effect of the microstructure in improving surface tribological and electrochemical properties. Based on the key observations reported in this study, it can be successfully concluded that ultrasonic vibrations are highly efficient in improving the developing a highly refined, equiaxed laser melted microstructure with significantly reduced surface texturing. These improvements are primarily due to the extensive hydrodynamic forces associated with ultrasonic vibrations that triggers dendrite fragmentation of the nascent dendrites in the melt. While the application of ultrasonic vibrations during laser surface melting resulted in significant melt expulsion from the surface, it entirely eliminated the large columnar grains from the resolidified region. The microstructure of the laser surface melted in both the aluminum and titanium samples under the influence of ultrasonic vibrations consisted of fine dendritic grains along the entire depth of the resolidified region. The grain refinement was observed to result resulting in about three-fold increase in surface microhardness. However, the refined microstructure was not highly successful in improving the electrochemical properties, as established in the studies on large area laser melted of aluminum samples with and without simultaneous applications of ultrasonic vibrations. The laser melted specimen without ultrasonic vibrations exhibited increase in open-circuit potential (higher corrosion potential) as well as decrease in corrosion rate compared to the ultrasonic vibrated

counterparts. The laser melted specimen with ultrasonic vibrations, exhibited an initial improvement in open-circuit potential.

However, their open circuit potential underwent rapid decrease that was confirmed to be a consequence of decreased stability of the passive corrosion film. The investigation on the effect of laser melting and remelting with and without simultaneous application of ultrasonic vibrations resulted in an improvement in thickness of laser clad composite surfaces and also a reduction in needle-like α-Si phase in the composite microstructure. It appears that the observed microstructural modification is due to partial melting/dissociation of already formed phases during subsequent laser remelting. The similar microstructural modification during ultrasonic vibration-assisted laser melting is likely due to cavitation and enhanced fluid convection effects. While the laser remelting resulted in an improvement in surface finish, the specimens processed with ultrasonic vibration-assisted laser melting exhibited higher surface roughness due to melt pool instability. A remarkable improvement in wear resistance of the Al-SiC composites was observed after laser remelting, and the wear mechanisms were characterized by presence of deep grooves (abrasive wear) and severely deformed patches (adhesive wear). The specimens processed with ultrasonic vibration-assisted laser melting showed inconsistent wear rates likely due to complex effects such as microstructural modification and enhanced surface roughness.

The large area surface melted and textured titanium substrates the laser processing resulted in the development of repeating undulating 'wavy' surface textures due to vertical and sideways flow of melt under the influence of ultrasonic vibrations applied to the substrates. The depth of the undulations and surface roughness in the textured surfaces increased with increasing ultrasonic power output. he microstructural analysis confirmed that the laser melting transformed the

microstructure from globular α to acicular α and martensitic α' as well as traces of retained β due to the high cooling rates associated with laser processing. The microstructural transformation also resulted in moderate surface hardening. The laser melted and textured surface exhibited higher wettability primarily due improved surface roughness and microstructural modification. The laser melting and surface texturing performed with ultrasonic vibration-assisted laser processing also resulted in significant reduction in coefficient of friction and wear rate for sliding wear tests performed in simulated body fluid.

CHAPTER VI

FUTURE WORK

6.1 Fundamental Investigations on the Effect of Processing Parameters on Mechanical Properties of Stainless Steel Components Developed by Additive Manufacturing

Additive manufacturing or rapid prototyping is a material fabrication method wherein a component is manufactured by successive deposition of layers. Naturally, unlike traditional machining and manufacturing techniques that primarily focusses on removal of material, additive manufacturing offers remarkable flexibility in component design. Therefore, this novel technique has gained significant popularity in aerospace, automobile and biomedical sections that often demands structural components with considerable dimensional complexity. It should be also noted, that apart from the remarkable flexibility in component dimensions, the unique processing technique of additive manufacturing that involves successive melting results in extensive thermal strains, particularly in the initial layers. Indeed, the thermal strains have been successfully employed to improve the material's mechanical strength by several leading research groups. However, it should be noted that the due to the dynamic nature of this technique, the manufactured components have been reported to exhibit inferior surface finish. Furthermore, inadequate powder assimilation has been reported to result in porosity of the fabricated components. Now, the rough surface and porosity are often reported to promote surface corrosion, particularly when the components are immersed in saline solutions. Also, it should be noted that all the major applications of additive manufacturing (aerospace, automobile and biomedical) involve exposure of the components to saline and/or acidic environments.

However, information on the mechanical behavior of additive manufactured components in saline environment, technically known as stress corrosion cracking is highly limited. Hence, this investigation is directed towards addressing the stress corrosion cracking of additive manufactured components using direct energy deposition technique. The investigations will be performed by using stainless steel powders, cited to be one of the most prevalent materials used for additive manufacturing of metallic components. The direct energy deposition will be performed using a LENS (Laser Engineered Net Shaping) technique. The investigation will be primarily directed towards understanding the effect of laser scanning velocity, one of the most important processing parameter in additive manufacturing on the stress-corrosion cracking behavior of the material. It has been widely accepted that while very high scanning velocities favor incomplete powder assimilation, thereby triggering porosity in the melt, significantly decreasing scanning velocities might result in extensive thermal deformation, hence high thermal strains and surface roughness. As mentioned earlier, both surface porosity and surface roughness deteriorate material's mechanical properties in saline environments. Hence, in this investigation, the scanning velocities will be systematically varied to investigate and establish their influence in porosity and roughness of the material. The fabricated components will then be sectioned as tensile specimen, immersed in saline (3.5% NaCl) solution for 4 weeks and their mechanical properties will be measured by tensile testing. Detailed study of the effect of the immersion (in saline solution) on the mechanical properties will be performed, comparing them with the non-immersed counterparts. The phase distribution and fracture behavior will be studied using x-ray diffraction and microscopic characterization studies respectively. Hence, the fundamental corrosion mechanisms that operate during the immersion as well as the influence of the processing parameters will be commented.

REFERENCES

[1] I. Polmear, D. StJohn, J.-F. Nie, M. Qian, Light alloys: metallurgy of the light metals, Butterworth-Heinemann2017.

[2] J.D. Majumdar, R. Galun, B. Mordike, I. Manna, Effect of laser surface melting on corrosion and wear resistance of a commercial magnesium alloy, Materials Science and Engineering: A 361(1-2) (2003) 119-129.

[3] Y. Kathuria, Some aspects of laser surface cladding in the turbine industry, Surface and Coatings Technology 132(2-3) (2000) 262-269.

[4] T. Watanabe, M. Shiroki, A. Yanagisawa, T. Sasaki, Improvement of mechanical properties of ferritic stainless steel weld metal by ultrasonic vibration, Journal of Materials Processing Technology 210(12) (2010) 1646-1651.

[5] T. Yue, T. Chan, H. Man, W. Lau, Analysis of ultrasonic-aided laser drilling using finite element method, CIRP Annals-Manufacturing Technology 45(1) (1996) 169-172.

[6] H. Zheng, H. Huang, Ultrasonic vibration-assisted femtosecond laser machining of microholes, Journal of Micromechanics and Microengineering 17(8) (2007) N58.

[7] J. Zhou, J. Xu, S. Huang, Z. Hu, X. Meng, Y. Fan, Microstructure and mechanical properties of Cr12MoV by ultrasonic vibration-assisted laser surface melting, Materials Science and Technology 33(10) (2017) 1200-1207.

[8] G.E. Dieter, D.J. Bacon, Mechanical metallurgy, McGraw-hill New York1986.

[9] E. Ghali, W. Dietzel, K.-U. Kainer, General and localized corrosion of magnesium alloys: a critical review, Journal of materials engineering and performance 13(1) (2004) 7-23.

[10] F. Bridier, P. Villechaise, J. Mendez, Analysis of the different slip systems activated by tension in a α/β titanium alloy in relation with local crystallographic orientation, Acta Materialia 53(3) (2005) 555-567.

[11] D.R. Lide, CRC handbook of chemistry and physics, 12J204 (2012).

[12] G. Welsch, R. Boyer, E. Collings, Materials properties handbook: titanium alloys, ASM international1993.

[13] A. Bloyce, P.-Y. Qi, H. Dong, T. Bell, Surface modification of titanium alloys for combined improvements in corrosion and wear resistance, Surface and Coatings Technology 107(2-3) (1998) 125-132.

[14] R.S. Rajamure, H.D. Vora, N. Gupta, S. Karewar, S. Srinivasan, N.B. Dahotre, Laser surface alloying of molybdenum on aluminum for enhanced wear resistance, Surface and Coatings Technology 258 (2014) 337-342.

[15] Z. Zhang, P. Lin, L. Ren, Wear resistance of AZ91D magnesium alloy processed by improved laser surface remelting, Optics and Lasers in Engineering 55 (2014) 237-242.

[16] N.B. Dahotre, S. Harimkar, Laser fabrication and machining of materials, Springer Science & Business Media2008.

[17] J. Abboud, D. West, Laser surface alloying of titanium with aluminium, Journal of materials science letters 9(3) (1990) 308-310.

[18] Y. Cui, C. Xu, Q. Han, Microstructure improvement in weld metal using ultrasonic vibrations, Advanced Engineering Materials 9(3) (2007) 161-163.

[19] X. Jian, T. Meek, Q. Han, Refinement of eutectic silicon phase of aluminum A356 alloy using high-intensity ultrasonic vibration, Scripta Materialia 54(5) (2006) 893-896.

[20] A. Das, H. Kotadia, Effect of high-intensity ultrasonic irradiation on the modification of solidification microstructure in a Si-rich hypoeutectic Al–Si alloy, Materials Chemistry and Physics 125(3) (2011) 853-859.

[21] H. Feng, S. Yu, Y. Li, L. Gong, Effect of ultrasonic treatment on microstructures of hypereutectic Al–Si alloy, Journal of materials processing technology 208(1-3) (2008) 330-335.

[22] R. Jiang, X. Li, M. Zhang, Investigation on the mechanism of grain refinement in aluminum alloy solidified under ultrasonic vibration, Metals and Materials International 21(1) (2015) 104-108.

[23] P. Jung-Kyu, Y. Ji-Woon, K. Myung-Chang, C. Sung-Hak, Surface effects of hybrid vibration-assisted femtosecond laser system for micro-hole drilling of copper substrate, Transactions of Nonferrous Metals Society of China 22 (2012) s801-s807.

[24] J.-K. Park, J.-W. Yoon, S.-H. Cho, Vibration assisted femtosecond laser machining on metal, Optics and Lasers in Engineering 50(6) (2012) 833-837.

[25] M. Mori, H. Kumehara, The effects of ultrasonic vibration on the accuracy of laser machining, Bull. Jpn. Soc. Precis. Eng. 9(3) (1975) 87-88.

[26] W. Lau, T. Yue, M. Wang, Ultrasonic-aided laser drilling of aluminium-based metal matrix composites, CIRP Annals-Manufacturing Technology 43(1) (1994) 177-180.

[27] B. Kang, G.W. Kim, M. Yang, S.-H. Cho, J.-K. Park, A study on the effect of ultrasonic vibration in nanosecond laser machining, Optics and Lasers in Engineering 50(12) (2012) 1817-1822.

[28] S.H. Alavi, S.P. Harimkar, Ultrasonic vibration-assisted continuous wave laser surface drilling of materials, Manufacturing Letters 4 (2015) 1-5.

[29] S.H. Alavi, S.P. Harimkar, Melt expulsion during ultrasonic vibration-assisted laser surface processing of austenitic stainless steel, Ultrasonics 59 (2015) 21-30.

[30] S.H. Alavi, C. Cowell, S.P. Harimkar, Experimental and finite element analysis of ultrasonic vibration− assisted continuous-wave laser surface drilling, Materials and Manufacturing Processes 32(2) (2017) 216-225.

[31] S.H. Alavi, S.P. Harimkar, Evolution of geometric and quality features during ultrasonic vibration-assisted continuous wave laser surface drilling, Journal of Materials Processing Technology 232 (2016) 52-62.

[32] Z. Fan, K. Wang, X. Dong, W. Duan, R. Wang, X. Mei, W. Wang, J. Cui, S. Zhang, C. Xu, Evaluation of microstructural evolution and corrosion types in ultrasonic assisted laser re-melted thermal barrier coatings under exposure to molten salts, Materials Letters 188 (2017) 145-148.

[33] W.E. Frazier, Metal additive manufacturing: a review, Journal of Materials Engineering and Performance 23(6) (2014) 1917-1928.

[34] B. Baufeld, O. Van der Biest, R. Gault, Additive manufacturing of Ti–6Al–4V components by shaped metal deposition: microstructure and mechanical properties, Materials & Design 31 (2010) S106-S111.

[35] F. Ning, W. Cong, Microstructures and mechanical properties of Fe-Cr stainless steel parts fabricated by ultrasonic vibration-assisted laser engineered net shaping process, Materials Letters 179 (2016) 61-64.

[36] W. Cong, F. Ning, A fundamental investigation on ultrasonic vibration-assisted laser engineered net shaping of stainless steel, International Journal of Machine Tools and Manufacture 121 (2017) 61-69.

[37] P. Sharma, A.K. Dubey, A.K. Pandey, Numerical Study of Temperature and Stress Fields in Laser Cutting of Aluminium Alloy Sheet, Procedia Materials Science 5(Supplement C) (2014) 1887-1896.

[38] C.F. Cheng, Y.C. Tsui, T.W. Clyne, Application of a three-dimensional heat flow model to treat laser drilling of carbon fibre composites, Acta Materialia 46(12) (1998) 4273-4285.

[39] M. Legay, N. Gondrexon, S. Le Person, P. Boldo, A. Bontemps, Enhancement of heat transfer by ultrasound: review and recent advances, International Journal of Chemical Engineering 2011 (2011).

[40] X. Jian, H. Xu, T. Meek, Q. Han, Effect of power ultrasound on solidification of aluminum A356 alloy, Materials letters 59(2-3) (2005) 190-193.

[41] J. Gu, C. Beckermann, A. Giamei, Motion and remelting of dendrite fragments during directional solidification of a nickel-base superalloy, Metallurgical and Materials Transactions A 28(7) (1997) 1533-1542.

[42] M. Zimmermann, M. Carrard, W. Kurz, Rapid solidification of Al-Cu eutectic alloy by laser remelting, Acta Metallurgica 37(12) (1989) 3305-3313.

[43] T. Eto, A. Sato, T. Mori, Stress-oriented precipitation of GP Zones and θ′ in an Al□ Cu alloy, Acta Metallurgica 26(3) (1978) 499-508.

[44] V.A. Phillips, L.E. Tanner, High resolution electron microscope observations on GP zones in an aged Cu-1.97 wt.% Be crystal, Acta Metallurgica 21(4) (1973) 441-448.

[45] Y.-X. Li, W.-W. Zhao, X.-S. Leng, Q.-J. Fu, W. Lei, J.-C. Yan, Microstructure evolution and mechanical properties of ultrasonic-assisted soldering joints of 2024 aluminum alloys, Transactions of Nonferrous Metals Society of China 21(9) (2011) 1937-1943.

[46] S. Gill, W. Kurz, Rapidly solidified Al□ Cu alloys—I. experimental determination of the microstructure selection map, Acta metallurgica et materialia 41(12) (1993) 3563-3573.

[47] S. Gill, W. Kurz, Rapidly solidified Al□ Cu alloys—II. Calculation of the microstructure selection map, Acta metallurgica et materialia 43(1) (1995) 139-151.

[48] J. Hunt, S. Lu, Numerical modeling of cellular/dendritic array growth: Spacing and undercooling predictions, Minerals, Metals and Materials Society, Warrendale, PA (United States), 1995.

[49] J. Hunt, S.-Z. Lu, Numerical modeling of cellular/dendritic array growth: spacing and structure predictions, Metallurgical and Materials Transactions A 27(3) (1996) 611-623.

[50] J. McLean, P. Saffman, The effect of surface tension on the shape of fingers in a Hele Shaw cell, Dynamics of Curved Fronts, Elsevier1988, pp. 175-189.

[51] A. Munitz, Microstructure of rapidly solidified laser molten AI-4.5 Wt Pct Cu Surfaces, Metallurgical Transactions B 16(1) (1985) 149-161.

[52] V. Seetharaman, L. Fabietti, R. Trivedi, Dendritic growth in the carbon tetrabromide and hexachlorethane system, Metallurgical Transactions A 20(11) (1989) 2567-2570.

[53] R. Li, M. Ferreira, A. Almeida, R. Vilar, K. Watkins, M. McMahon, W. Steen, Localized corrosion of laser surface melted 2024-T351 aluminium alloy, Surface and coatings technology 81(2-3) (1996) 290-296.

[54] G. Zhong, S. Wu, H. Jiang, P. An, Effects of ultrasonic vibration on the iron-containing intermetallic compounds of high silicon aluminum alloy with 2% Fe, Journal of alloys and compounds 492(1-2) (2010) 482-487.

[55] A. Taha, F. Hammad, Application of the Hall-Petch Relation to Microhardness Measurements on Al, Cu, Al-MD 105, and Al-Cu Alloys, Physica status solidi (a) 119(2) (1990) 455-462.

[56] S.J. Kalita, Microstructure and corrosion properties of diode laser melted friction stir weld of aluminum alloy 2024 T351, Applied Surface Science 257(9) (2011) 3985-3997.

[57] A. Pardo, M. Merino, A.E. Coy, R. Arrabal, F. Viejo, E. Matykina, Corrosion behaviour of magnesium/aluminium alloys in 3.5 wt.% NaCl, Corrosion Science 50(3) (2008) 823-834.

[58] J.R. Davis, Corrosion of aluminum and aluminum alloys, Asm International1999.

[59] M. Mandal, A. Moon, G. Deo, C. Mendis, K. Mondal, Corrosion behavior of Mg–2.4 Zn alloy micro-alloyed with Ag and Ca, Corrosion Science 78 (2014) 172-182.

[60] S. Biswas, S.H. Alavi, S.P. Harimkar, Effect of laser remelting and simultaneous application of ultrasonic vibrations during laser melting on the microstructural and tribological properties of laser clad Al-SiC composites, Journal of Composites Science 1(2) (2017) 13.

[61] X. Liu, Y. Osawa, S. Takamori, T. Mukai, Grain refinement of AZ91 alloy by introducing ultrasonic vibration during solidification, Materials Letters 62(17-18) (2008) 2872-2875.

[62] M. Lekala, J. Van Der Merwe, S. Pityana, Laser surface alloying of 316L stainless steel with Ru and Ni mixtures, International Journal of Corrosion 2012 (2012).

[63] S.P. Harimkar, N.B. Dahotre, Crystallographic and morphological textures in laser surface modified alumina ceramic, Journal of applied physics 100(2) (2006) 024901.

[64] A. Simchi, D. Godlinski, Effect of SiC particles on the laser sintering of Al–7Si–0.3 Mg alloy, Scripta Materialia 59(2) (2008) 199-202.

[65] J. Ehrström, W. Kool, Production of rapidly solidified Al/SiC composites, Journal of materials science 23(9) (1988) 3195-3201.

[66] R. Anandkumar, A. Almeida, R. Colaço, R. Vilar, V. Ocelik, J.T.M. De Hosson, Microstructure and wear studies of laser clad Al-Si/SiC (p) composite coatings, Surface and Coatings Technology 201(24) (2007) 9497-9505.

[67] W. Wang, F. Ajersch, J. Löfvander, Si phase nucleation on SiC particulate reinforcement in hypereutectic Al□ Si alloy matrix, Materials Science and Engineering: A 187(1) (1994) 65-75.

[68] J. Jiang, R. Arnell, The effect of substrate surface roughness on the wear of DLC coatings, Wear 239(1) (2000) 1-9.

[69] D. Guha, S.R. Chowdhuri, The effect of surface roughness on the temperature at the contact between sliding bodies, Wear 197(1-2) (1996) 63-73.

[70] J.D. Majumdar, B.R. Chandra, I. Manna, Friction and wear behavior of laser composite surfaced aluminium with silicon carbide, Wear 262(5-6) (2007) 641-648.

[71] J. Gandra, P. Vigarinho, D. Pereira, R. Miranda, A. Velhinho, P. Vilaça, Wear characterization of functionally graded Al–SiC composite coatings produced by friction surfacing, Materials & Design (1980-2015) 52 (2013) 373-383.

[72] T. Liechti, Développement de revêtements portants déposés par laser sur des alliages d'aluminium, [Verlag nicht ermittelbar], [Erscheinungsort nicht ermittelbar], 1996.

[73] Z. Fang, Z. Yan, Y. Tan, X. Liu, Y. Wang, Influence of post-annealing treatment on the structure properties of ZnO films, Applied Surface Science 241(3-4) (2005) 303-308.

[74] S. Tjong, K. Lau, Tribological behaviour of SiC particle-reinforced copper matrix composites, Materials Letters 43(5-6) (2000) 274-280.

[75] H. Man, C. Kwok, T. Yue, Cavitation erosion and corrosion behaviour of laser surface alloyed MMC of SiC and Si3N4 on Al alloy AA6061, Surface and Coatings Technology 132(1) (2000) 11-20.

[76] Z. Zhang, L. Zhang, Y.-W. Mai, Particle effects on friction and wear of aluminium matrix composites, Journal of Materials Science 30(23) (1995) 5999-6004.

[77] S. Biswas, S.H. Alavi, S.P. Harimkar, Laser surface melting of Ti–6Al–4V under the influence of ultrasonic vibrations, Materials Letters 159 (2015) 470-473.

[78] S. Thangaraju, M. Heilmaier, B.S. Murty, S.S. Vadlamani, On the estimation of true Hall–Petch constants and their role on the superposition law exponent in Al alloys, Advanced Engineering Materials 14(10) (2012) 892-897.

[79] W.F. Smith, J. Hashemi, Foundations of materials science and engineering, McGraw-Hill2011.

[80] S. Yerramareddy, S. Bahadur, The effect of laser surface treatments on the tribological behavior of Ti-6Al-4V, Wear 157(2) (1992) 245-262.

[81] W. Pfleging, R. Kumari, H. Besser, T. Scharnweber, J.D. Majumdar, Laser surface textured titanium alloy (Ti–6Al–4V): Part 1–Surface characterization, Applied Surface Science 355 (2015) 104-111.

[82] R. Kumari, T. Scharnweber, W. Pfleging, H. Besser, J.D. Majumdar, Laser surface textured titanium alloy (Ti–6Al–4V)–Part II–Studies on bio-compatibility, Applied Surface Science 357 (2015) 750-758.

[83] Y. Arima, H. Iwata, Effect of wettability and surface functional groups on protein adsorption and cell adhesion using well-defined mixed self-assembled monolayers, Biomaterials 28(20) (2007) 3074-3082.

[84] R. Pederson, Microstructure and Phase transformation of Ti-6Al-4V, Luleå tekniska universitet, 2002.

[85] Y. Prasad, T. Seshacharyulu, S. Medeiros, W. Frazier, Influence of oxygen content on the forging response of equiaxed (α+ β) preform of Ti–6Al–4V: commercial vs. ELI grade, Journal of Materials Processing Technology 108(3) (2001) 320-327.

[86] S. Hyun, D.-R. Lee, B.-G. Loh, Investigation of convective heat transfer augmentation using acoustic streaming generated by ultrasonic vibrations, International Journal of Heat and Mass Transfer 48(3-4) (2005) 703-718.

[87] B.-G. Loh, S. Hyun, P.I. Ro, C. Kleinstreuer, Acoustic streaming induced by ultrasonic flexural vibrations and associated enhancement of convective heat transfer, The Journal of the Acoustical Society of America 111(2) (2002) 875-883.

[88] R.K. Gould, Heat Transfer across a Solid-Liquid Interface in the Presence of Acoustic Streaming, The Journal of the Acoustical Society of America 40(1) (1966) 219-225.

[89] M. Imam, C. Gilmore, Fatigue and microstructural properties of quenched Ti-6Al-4V, Metallurgical Transactions A 14(1) (1983) 233-240.

[90] I. Weiss, S. Semiatin, Thermomechanical processing of alpha titanium alloys—an overview, Materials Science and Engineering: A 263(2) (1999) 243-256.

[91] T. Ahmed, H. Rack, Phase transformations during cooling in α+ β titanium alloys, Materials Science and Engineering: A 243(1-2) (1998) 206-211.

[92] L. Thijs, F. Verhaeghe, T. Craeghs, J. Van Humbeeck, J.-P. Kruth, A study of the microstructural evolution during selective laser melting of Ti–6Al–4V, Acta materialia 58(9) (2010) 3303-3312.

[93] T. Uelzen, J. Müller, Wettability enhancement by rough surfaces generated by thin film technology, Thin Solid Films 434(1-2) (2003) 311-315.

[94] L. Hao, J. Lawrence, Wettability modification and the subsequent manipulation of protein adsorption on a Ti6Al4V alloy by means of CO2 laser surface treatment, Journal of Materials Science: Materials in Medicine 18(5) (2007) 807-817.

[95] L. Hao, J. Lawrence, L. Li, Manipulation of the osteoblast response to a Ti–6Al–4V titanium alloy using a high power diode laser, Applied Surface Science 247(1-4) (2005) 602-606.

[96] P.M. Barkhudarov, P.B. Shah, E.B. Watkins, D.A. Doshi, C.J. Brinker, J. Majewski, Corrosion inhibition using superhydrophobic films, Corrosion Science 50(3) (2008) 897-902.

[97] M. Jovanović, S. Tadić, S. Zec, Z. Mišković, I. Bobić, The effect of annealing temperatures and cooling rates on microstructure and mechanical properties of investment cast Ti–6Al–4V alloy, Materials & design 27(3) (2006) 192-199.

[98] N. Poondla, T.S. Srivatsan, A. Patnaik, M. Petraroli, A study of the microstructure and hardness of two titanium alloys: Commercially pure and Ti–6Al–4V, Journal of Alloys and Compounds 486(1-2) (2009) 162-167.

[99] K. Hokkirigawa, K. Kato, An experimental and theoretical investigation of ploughing, cutting and wedge formation during abrasive wear, Tribology international 21(1) (1988) 51-57.

[100] K.G. Budinski, Tribological properties of titanium alloys, Wear 151(2) (1991) 203-217.

[101] D. Berman, S.A. Deshmukh, S.K. Sankaranarayanan, A. Erdemir, A.V. Sumant, Macroscale superlubricity enabled by graphene nanoscroll formation, Science 348(6239) (2015) 1118-1122.

[102] D. Berman, A. Erdemir, A.V. Sumant, Few layer graphene to reduce wear and friction on sliding steel surfaces, Carbon 54 (2013) 454-459.

[103] W. Liang, X. Bin, Y. Zhiwei, S. Yaqin, The wear and corrosion properties of stainless steel nitrided by low-pressure plasma-arc source ion nitriding at low temperatures, Surface and Coatings Technology 130(2-3) (2000) 304-308.

[104] Y. Sun, T. Bell, Dry sliding wear resistance of low temperature plasma carburised austenitic stainless steel, Wear 253(5-6) (2002) 689-693.

[105] H.C. Lee, W.-W. Liu, S.-P. Chai, A.R. Mohamed, A. Aziz, C.-S. Khe, N.M. Hidayah, U. Hashim, Review of the synthesis, transfer, characterization and growth mechanisms of single and multilayer graphene, RSC Advances 7(26) (2017) 15644-15693.

[106] A.C. Ferrari, J. Meyer, V. Scardaci, C. Casiraghi, M. Lazzeri, F. Mauri, S. Piscanec, D. Jiang, K. Novoselov, S. Roth, Raman spectrum of graphene and graphene layers, Physical review letters 97(18) (2006) 187401.

[107] M. Couzi, J.-L. Bruneel, D. Talaga, L. Bokobza, A multi wavelength Raman scattering study of defective graphitic carbon materials: The first order Raman spectra revisited, Carbon 107 (2016) 388-394.

[108] A.C. Ferrari, Raman spectroscopy of graphene and graphite: disorder, electron–phonon coupling, doping and nonadiabatic effects, Solid state communications 143(1-2) (2007) 47-57.

[109] A.d.O. Fraga, M.A. Klunk, A.A.d. Oliveira, G.G. Furtado, G. Knörnschild, L.F.P. Dick, Soil corrosion of the AISI1020 steel buried near electrical power transmission line towers, Materials Research 17(6) (2014) 1637-1643.

[110] R.A. Antunes, I. Costa, D.L.A.d. Faria, Characterization of corrosion products formed on steels in the first months of atmospheric exposure, Materials research 6(3) (2003) 403-408.

[111] G. Singh, A. Moon, S. Sengupta, G. Deo, S. Sangal, K. Mondal, Corrosion behavior of IF steel in various media and its comparison with mild steel, Journal of Materials Engineering and Performance 24(5) (2015) 1961-1974.

[112] J.-f. Lu, C.-J. Tsai, Hydrothermal phase transformation of hematite to magnetite, Nanoscale research letters 9(1) (2014) 230.

[113] A.C. Ferrari, J. Robertson, Interpretation of Raman spectra of disordered and amorphous carbon, Physical review B 61(20) (2000) 14095.

[114] K.N. Kudin, B. Ozbas, H.C. Schniepp, R.K. Prud'Homme, I.A. Aksay, R. Car, Raman spectra of graphite oxide and functionalized graphene sheets, Nano letters 8(1) (2008) 36-41.

APPENDICES

LIST OF PUBLICATIONS

Biswas, Sourabh, S. Habib Alavi, and Sandip P. Harimkar. "Laser surface melting of Ti–6Al–4V under the influence of ultrasonic vibrations." *Materials Letters* 159 (2015): 470-473.

Biswas, Sourabh, S. Habib Alavi, and Sandip P. Harimkar. "Effect of Laser Remelting and Simultaneous Application of Ultrasonic Vibrations during Laser Melting on the Microstructural and Tribological Properties of Laser Clad Al-SiC Composites." *Journal of Composites Science* 1.2 (2017): 13.

Biswas, Sourabh, S. Habib Alavi, and Sandip P. Harimkar. "Effect of simultaneous application of ultrasonic vibrations during laser surface melting on electrochemical properties of 2024 aluminum alloy." *Advanced Materials Proceedings* 2.10 (2017): 3

Biswas, Sourabh, S. Habib Alavi, Bhishma Sedai, Frank D. Blum and Sandip P. Harimkar. "Effect of Ultrasonic Vibration-Assisted Laser Surface Melting and Texturing of Ti-6Al-4V ELI Alloy on Surface Properties." *Journal of Materials Science and Technology (Accepted)*

Biswas, Sourabh, S. Habib Alavi, and Sandip P. Harimkar. "Effect of ultrasonic vibrations in microstructural evolution, elemental distribution and mechanical properties of laser surface melted Al-5.6Cu-2.8Mg aluminum alloy." *Journal of Alloys and Compounds (Submitted)*

VITA

Sourabh Biswas

Candidate for the Degree of

Doctor of Philosophy

Dissertation: ULTRASONIC VIBRATION-ASSISTED LASER SURFACE ENGINEERING OF STRUCTURAL ALLOYS

Major Field: Mechanical and Aerospace Engineeing

Biographical:

Education:

Completed the requirements for the Doctor of Philosophy in Mechanical and Aerospace Engineering at Oklahoma State University, Stillwater, Oklahoma in December, 2018.

Completed the requirements for the Master of Science in Mechanical and Aerospace Engineering at Oklahoma State University, Stillwater, Oklahoma in 2014.

Completed the requirements for the Bachelor of Engineering in Metallurgical and Materials Engineering at Indian Institute of Engineering Science and Technology, Shibpur, India in 2011.